AVERTISSEMENT

Ce document est le fruit d'un long travail approuvé par le jury de soutenance et mis à disposition de l'ensemble de la communauté universitaire élargie.

Il est soumis à la propriété intellectuelle de l'auteur. Ceci implique une obligation de citation et de référencement lors de l'utilisation de ce document.

D'autre part, toute contrefaçon, plagiat, reproduction illicite encourt une poursuite pénale.

Contact : ddoc-theses-contact@univ-lorraine.fr

LIENS

Code de la Propriété Intellectuelle. articles L 122. 4
Code de la Propriété Intellectuelle. articles L 335.2- L 335.10
http://www.cfcopies.com/V2/leg/leg_droi.php
http://www.culture.gouv.fr/culture/infos-pratiques/droits/protection.htm

UNIVERSITÉ DE LORRAINE

École doctorale RP2E

Laboratoire GeoRessources

THÈSE

Présentée en vue d'obtenir le grade de

DOCTEUR DE l'UNIVERSITÉ DE LORRAINE

Spécialité : **Mécanique - Génie Civil**

par

Ahmad HAJJAR

Analytical, numerical, and experimental investigations of particle transport in fractures with flat and corrugated walls

soutenance prévue le 6 décembre 2017 devant le jury composé de :

Jean-Régis Angilella	PR,	Université de Caen-Normandie	Rapporteur
Valeri Mourzenko	DR,	Institut Pprime	Rapporteur
Anne Tanière	PR,	Université de Lorraine	Examinatrice
Armelle Jarno-Druaux	MCF,	Université du Havre	Examinatrice
Constantin Oltéan	MCF,	Université de Lorraine	Examinateur
Michel Buès	PR,	Université de Lorraine	Directeur de thèse

Membres invités :

Luc Scholtès	MCF, Université de Lorraine	Co-directeur de thèse
Mohammed Souhar	PR, Université de Lorraine	

All praise and thanks are due to the Almighty God for giving me the strength to complete this thesis. Without His blessings, this achievement would not have been possible.

I dedicate this dissertation to the memory of my mother and my father

... Until we meet again

Acknowledgments

I would like to thank my thesis supervisor, Prof. Michel Buès, for the confidence and the freedom he granted me to prepare this thesis, for his support, and for giving me the opportunity to express my taste for teaching.

I am grateful to my thesis co-supervisor, Dr. Luc Scholtès, for his guidance, his availability, and his constructive and thoughtful suggestions throughout my time as a PhD student. I am also very thankful to him for his careful editing and proofreading work, which contributed enormously to the productivity of this thesis.

I would like to thank Dr. Constantin Oltéan for the constructive discussions we had together and for providing me continuously with new ideas to improve my work. I thank him also for accepting to participate in the jury.

I would like to express my gratitude to Jean-Rgis Angilella, Professor at Université de Caen, and to Valeri Mourzenko, Director of Research at Institut Pprime, for the honor they gave me by agreeing to review my thesis dissertation, as well as for their interesting comments and constructive criticism. I am equally grateful to Prof. Anne Tanire, to Dr. Armelle Jarno-Druaux, and to Prof. Mohammed Souhar for agreeing to participate in the jury and for making my defense an enjoyable moment.

I would also like to thank Mr. Éric Lefèvre for his technical assistance and his good humor, and for all the GeoRessources employees for their kindness and for creating a nice working environment.

In my thanks, I can not forget my kind colleagues, PhD students and Postdocs, with whom I shared the most pleasant moments.

I do not forget to thank all my former teachers at Lycée Pascal, the school in which I spent fifteen years of my life. I thank them for molding me into the person I am today.

My deep gratitude is due to my brothers Mohammad and Mahmoud, to my parents-in-law, and to my brothers-in-law for their support despite the distance.

Last but not least, I address my special and affectionate thanks and my deep indebtedness to my wife Aseel, for her unconditional support and patience. I could not have completed this work without her. I would like also to express my love to my precious daughter, Asmahan, whose presence in my life made the hardship of this task bearable.

Abstract

Analytical, numerical, and experimental investigations of particle transport in fractures with flat and corrugated walls

The aim of the present thesis is to study the transport and deposition of small solid particles in fracture flows. First, single-phase fracture flow is investigated in order to assess the validity of the local cubic law for modeling flow in corrugated fractures. Channels with sinusoidal walls having different geometrical properties are considered to represent different fracture geometries. It is analytically shown that the hydraulic aperture of the fracture clearly deviates from its mean aperture when the walls roughness is relatively high. The finite element method is then used to solve the continuity and the Navier-Stokes equations and to simulate fracture flow in order to compare with the theoretical predictions of the local cubic law for Reynolds numbers Re in the range $6.7 \times 10^{-2} - 6.7 \times 10^{1}$. The results show that for low Re, typically less than 15, the local cubic law can properly describe the fracture flow, especially when the fracture walls have small corrugation amplitudes. For Re higher than 15, the local cubic law can still be valid under the conditions that the fracture presents a low aspect ratio, small corrugation amplitude, and moderate phase lag between its walls. Second, particle-laden flows are studied. An analytical approach has been developed to show how particles sparsely distributed in steady and laminar fracture flows can be transported for long distances or conversely deposited inside the channel. More precisely, a rather simple particle trajectory equation is established. Based on this equation, it is demonstrated that when particles' inertia is negligible, their behavior is characterized by the fracture geometry and by a dimensionless number W that relates the ratio of the particles sedimentation terminal velocity to the flow mean velocity. The proposed particle trajectory equation is verified by comparing its predictions to particle tracking numerical simulations taking into account particle inertia and resolving the full Navier-Stokes equations. The equation is shown to be valid under the conditions that flow inertial effects are limited. Based on this trajectory equation, regime diagrams that can predict the behavior of particles entering closed channel flows are built. These diagrams enable to forecast if the particles entering the channel will be either deposited or transported till the channel outlet. Finally, an experimental apparatus that was designed to have a practical assessment of the analytical model is presented. Preliminary experimental results tend to verify the analytical model. Overall, the work presented in this thesis give new insights on the behavior of small particles in fracture flows, which may improve our prediction and control of underground contamination, and may have applications in the development of new water filtration and mineral separation techniques.

Keywords: Particle-laden flow, Particle trajectory, Corrugated walls, Rough Fracture, Local Cubic Law

Résumé

Études analytique, numérique, et expérimentale du transport de particules dans des fractures parois plates et ondulées

Le but de cette thèse est d'étudier le transport et le dépôt de particules solides dans les écoulements à travers les fractures. Dans un premier temps, l'écoulement monophasique à travers les fractures est étudié afin d'évaluer la validité de la loi cubique locale comme modèle de l'écoulement. Des canaux à parois sinsoïdales à géométrie variable sont utilisés pour représenter différents types de fractures. Un premier développement analytique montre que l'ouverture hydraulique de la fracture diffère de son ouverture moyenne lorsque la rugosité des parois est élevée. La méthode des éléments finis est ensuite utilisée pour résoudre les équations de continuité et de Navier-Stokes et comparer les solutions numériques aux prédictions théoriques de la loi cubique locale sur une gamme relativement étendue de nombres de Reynolds Re. Pour de faibles Re, typiquement inférieurs à 15, la loi cubique locale décrit raisonnablement l'écoulement, surtout lorsque la rugosité et le déphasage entre les parois sont relativement faibles. Dans un deuxième temps, les écoulements chargés de particules sont étudiés. Une approche analytique est d'abord développée pour montrer comment des particules distribuées dans un écoulement stationnaire et laminaire à travers une fracture peuvent être transportées sur de longues distances ou au contraire se déposer à l'intérieur. Plus précisément, une équation simple décrivant la trajectoire d'une particule est établie. Sur la base de cette équation, il est démontré que, quand l'inertie des particules est négligeable, leur comportement dépend directement de la géométrie de la fracture et d'un nombre adimensionnel W qui relie la vitesse de sédimentation des particules à la vitesse moyenne de l'écoulement. L'équation proposée est vérifiée en comparant ses prédictions à des simulations numériques de suivi de particules prenant en compte l'inertie des particules et résolvent complètement les équations de Navier-Stokes. Il est montré que l'équation est valide lorsque l'inertie du fluide est faible. Des diagrammes de régimes, permettant de prévoir le comportement des particules à travers la fracture sont proposés. Enfin, un appareil expérimental conçu dans le but d'effectuer une évaluation pratique du modèle analytique est présenté et les résultats préliminaires sont discutés. Les rèsultats expérimentaux préliminaires tendent valider le modèle analytique. De façon plus générale, les résultats obtenus à travers ce travail de thèse font progresser nos connaissances du comportement des petites particules transportées dans les écoulements de fractures. Potentiellement, ce travail devrait permettre d'améliorer notre prévision de la pollution souterraine, et peut avoir des applications dans le développement de nouvelles techniques de filtration de l'eau et de séparation des minéraux.

Mots-clefs: Transport de particules, Fracture rugueuse, Parois ondulées, Loi cubique locale

Résumé étendu

La modélisation des fluides chargés en particules à travers des canaux d'écoulement interne est fondamentale afin de mieux appréhender divers applications environnementales, telles que le transport de sédiments et la pollution souterraine ou industrielles, comme la filtration de l'eau et la séparation des minéraux, ou encore, l'exploitation des ressources pétrolières. Le transport de contaminants à travers les fractures rugueuses est aussi un sujet de recherche important de par sa relation directe avec la contamination des formations aquifères.

Dans ce contexte, la présente thèse est consacrée à l'étude du transport et de la déposition de particules solides dans des écoulements à travers des canaux fermés, avec une application aux fractures rugueuses. En particulier, on considère des fractures à parois planes et ondulées (Figure 1). L'objectif principal de ce travail est de déterminer les conditions pour lesquelles les particules se déposeront à l'intérieur de la fracture ou, au contraire, seront transportées sur de grandes distances. Plusieurs paramètres doivent être pris en compte pour étudier le comportement des particules immergées dans un fluide en mouvement. Tout d'abord, les propriétés des particules, telles que leur taille et leur densité, doivent être connues pour déterminer les forces pouvant agir sur leur déplacement. Par exemple, lorsque la taille des particules est inférieure au micron, leur comportement est dominé par la diffusion brownienne. En revanche, dans le cas de particules plus grosses, leur mouvement est insensible à la diffusion brownienne et leur transport dépend uniquement des forces macroscopiques extérieures, comme les forces gravitationnelles et hydrodynamiques. Normalement, l'augmentation de la taille et/ou de la densité des particules tend à favoriser leur déposition en raison de la prédominance des effets gravitationnels sur leur comportement. Deuxièmement, les caractéristiques de l'écoulement, telles que la vitesse, la viscosité et la

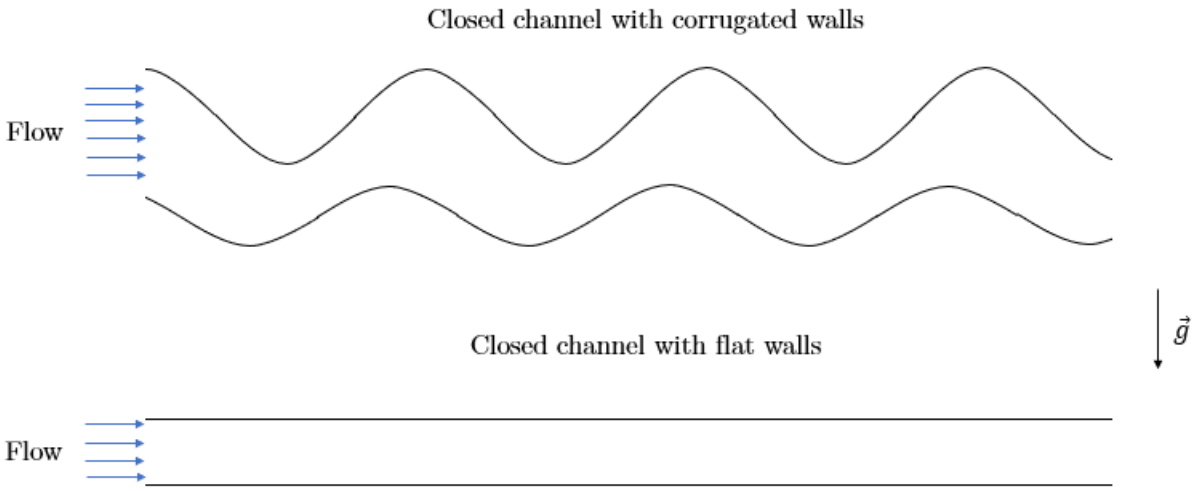

Figure 1: Fractures à parois planes et ondulées considérées dans cette thèse

masse volumique du fluide, sont également des facteurs importants qui doivent être pris en compte pour modéliser correctement le comportement des particules. L'augmentation de la viscosité du fluide, par exemple, tend à favoriser le transport des particules sur de plus longues distances en raison de forces de frottement plus importantes entre le fluide et les particules.

Dans tout écoulement chargé de particules, il est important d'avoir une description précise de l'écoulement du fluide avant de modéliser le transport de particules. Dans le cas des fractures rugueuses, un modèle bien connu et souvent utilisé pour décrire l'écoulement est la loi cubique locale (LCL), qui est une solution analytique approximative des équations de Navier-Stokes (NS) pour les écoulements laminaires visqueux à travers les fractures. Cependant, l'applicabilité de la LCL reste discutable. En fait, un certain désaccord est évoqué dans les critères proposés par différents auteurs pour valider cette loi. Ceci est dû est lié aux études précédentes réalisées avec des fractures ayant des géométries spécifiques. Afin de pallier à ce problème, une étude numérique approfondie a étv menée. Ainsi, la première partie de notre travail est dédiée à l'effet induit par la géométrie de la fracture sur la validité de la LCL, sous différentes conditions liées à la géométrie et à l'écoulement. Cette étude est plus que nécessaire puisque la LCL constitue la base du modèle de transport de particules dans les fractures.

Pour l'étude du transport des particules, trois approches ont été adoptées:

- Approche analytique : En supposant que l'inertie des particules soit négligeable, une forme simplifiée de l'équation du mouvement des particules est couplée à la LCL, et, par conséquent, une équation décrivant les trajectoires des particules est développée. Les particules peuvent alors être suivies analytiquement et la distance à laquelle elles se déposeront peut être calculée. Cette équation relie un nombre sans dimension W à la géométrie de la fracture. W dépend des propriétés des particules et des caractéristiques de l'écoulement. Basé sur W et sur les propriétés géométriques de la fracture, des régimes de transport et de sédimentation sont définis, et des diagrammes de régime sont établis.

- Approche numérique : En prenant en compte l'inertie des particules et en résolvant les équations complètes de NS, des simulations numériques sont menées pour confirmer la capacité du modèle analytique à prédire le comportement des particules dans les fractures. Les distances auxquelles les particules sédimentent à l'intérieur de la fracture sont calculées numériquement et comparées aux solutions de l'équation des trajectoires déterminée analytiquement. Des expériences numériques sont ensuite menées afin d'évaluer la pertinence des diagrammes de régime.

- Approche expérimentale : Un dispositif expérimental a été conçu et construit dans le but principal de vérifier le modèle analytique. Des tests préliminaires utilisant des graines de pavot comme particules ont été conduits, et les résultats expérimentaux ont été comparés aux prédictions du modèle analytique.

Cette thèse est divisée en quatre chapitres:

Dans le chapitre 1, on présente les concepts de base des écoulements chargés en particules sont présentés, ainsi qu'un état de l'art sur l'écoulement et le transport des particules dans des fractures.

Le chapitre 2 est consacré à l'étude des écoulements monophasiques dans des fractures à parois sinusoïdales. Les simulations numériques visant à évaluer la validité de la LCL sont présentées et les résultats sont discutés et comparés aux travaux précédents.

Dans le chapitre 3, l'intérê est proté sur le modèle analytique décrivant le transport des particules faiblement inertielles dans les canaux fermés. Les expériences numériques visant

à vérifier le modèle analytique sont également présentées et discutées.

Dans le chapitre 4, le dispositif expérimental conçu pour une évaluation pratique du modèle analytique est décrit. Des résultats expérimentaux préliminaires utilisant des graines de pavot sont présentés.

Enfin, les principaux résultats obtenus tout au long de la thèse sont résumés et les perspectives du travail sont discutées.

Chapitre 2

Différents modèles ont été utilisés en hydrogéologie pour étudier l'écoulement à travers des fractures à parois rugueuses. L'idéalisation de la fracture en tant que canal à deux parois plates simplifie grandement le problème et permet de trouver une solution analytique pour le champ des vitesses, appelée la loi cubique (CL). En tenant compte de la rugosité des parois et en considérant une faible variation de l'ouverture dans la direction de l'écoulement, on peut utiliser l'équation de Reynolds qui conduit à la loi cubique locale (LCL), où les composantes du vecteur vitesse sont exprimées en fonction de la géométrie de la fracture. Cependant, la validité de la CL et de la LCL reste discutable. En effet, il existe des critères, strictement liés à la géométrie de la fracture, permettant l'applicabilité de ces deux lois. Dans ce chapitre, une étude numérique visant à évaluer la validité de la CL et de la LCL, en considérant des fractures avec différentes géométries, est menée. Les fractures sont représentées par des canaux à parois sinusoïdales ayant des propriétés géométriques différentes définissant l'ouverture du canal, l'amplitude et la longueur d'onde des ondulations des parois, l'asymétrie entre les ondulations des deux parois, et le déphasage entre les deux parois. La validité de la LCL est évaluée pour des nombres de Reynolds dans la gamme $[6.7 \times 10^{-2}, 6.7 \times 10^{1}]$, en comparant ses prédictions à la solution numérique des équations de Navier-Stokes (NS). Cette dernière est obtenue en utilisant la méthode des éléments finis, implémentée dans le logiciel COMSOL Multiphysics.

Les résultats obtenus confirment que la CL, basée sur l'ouverture moyenne de la fracture, peut remplacer la LCL, basée sur l'ouverture hydraulique, tant que les ondulations des parois sont relativement petites ou lorsque les parois sont identiques et parallèles. Par contre, elle

surestime nettement le débit dès que l'amplitude des ondulations devient élevée, surtout dans les fractures ayant des parois décalées et/ou des parois avec différentes amplitudes d'ondulation.

La LCL est valide pour modéliser l'écoulement des fluides dans les fractures pour à faible Re, et en particulier dans les fractures avec de faibles ratios d'aspect et de faibles amplitudes d'ondulation. Cependant, l'écart entre les solutions de la LCL et des équations NS augmente même à faible Re, lorsque les parois sont en phase et lorsque les deux parois présentent une amplitude d'ondulation élevée. Cet écart est dû à la courbure des lignes de courant qui augmente la tortuosité de l'écoulement et la dissipation d'énergie à l'intérieur de la fracture. Lorsque Re augmente, les effets inertiels deviennent significatifs pour $Re > 15$. Cela signifie que les résultats obtenus pour faibles Re sont valides pour des valeurs de Re inférieures à 15. Au-dessus de cette limite, la LCL peut encore être pertinente pour modéliser l'écoulement sous la condition que la fracture présente un petit rapport d'aspect, de faibles amplitudes d'ondulation, et de faibles variations dans l'ouverture locale le long de la direction d'écoulement. Lorsque ces conditions ne sont pas respectées, l'accélération et la décélération répétées du fluide, dues à la variation de l'ouverture locale, tendent à favoriser les effets inertiels et donc à augmenter l'écart entre les solutions de la LCL et celles des équations de NS.

En conclusion, une estimation quantitative de l'erreur relative en utilisant la LCL, voire la CL, pour modéliser l'écoulement du fluide dans les fractures rugueuses a été effectuée. Il ressort que, tant que les écoulements dans les fractures dépendent fortement de la géométrie de la fracture, les critères existants dans la littérature ne permettent pas de généraliser l'applicabilité de la LCL ou la CL pour tout type de fracture, i.e., à géométrie arbitraire. Cependant, la LCL est valide pour modéliser l'écoulement pour de faibles ratios d'aspect et de faibles amplitudes d'ondulation.

Chapitre 3

Ce chapitre est consacré à l'étude du transport des particules dans les fractures, en supposant que l'écoulement peut être décrit par la LCL comme discuté au chapitre 2. Les partic-

ules sont non-browniennes, passives et de dimensions largement plus faibles que l'ouverture de la fracture. Comme au chapitre 2, des canaux à parois planes et sinusoïdales sont considérés.

L'inertie des particules est considérée comme faible de telle sorte qu'elle peut être négligée dans l'équation du mouvement. On montre que, sous cette condition, le comportement des particules peut être caractérisé par la géométrie du canal et par un nombre sans dimension W qui représente le rapport entre la vitesse de sédimentation des particules et la vitesse moyenne de l'écoulement. Une équation différentielle définissant la trajectoire des particules dans les canaux à parois ondulées et une équation exacte de cette trajectoire dans les canaux à parois planes ont été dérivées sous l'hypothèse que la vitesse de l'écoulement peut être explicitement calculée en utilisant la LCL. Ces équations ont été vérifiées à travers les solutions numériques basées sur une technique de suivi des particules impliquant les équations du mouvement des particules et le champ d'écoulement obtenu par la résolution des équations de NS. Les simulations numériques ont été réalisées en tenant compte à la fois de l'inertie des particules et de celle du fluide. Les résultats numériques ont confirmé les hypothèses sous lesquelles l'approche analytique a été développée. De plus, ils ont confirmé que la trajectoire des particules peut être prédite directement en fonction de la valeur de W et de la géométrie du canal, sans avoir besoin de calculs ou de simulations numériques supplémentaires.

En se basant sur ces développements, un diagramme de régime qui prédit le transport ou la sédimentation des particules en fonction de W et d'un paramètre géométrique h^*, représentant le rapport entre l'ouverture moyenne du canal et sa longueur totale, a été proposé (Figure 2).

Pour les canaux à parois ondulées, le diagramme de régimes est similaire à celui obtenu pour les canaux à parois planes, mais les zones de transport et de sédimentation ont tendance à augmenter ou diminuer en fonction de la période et l'amplitude des ondulations, et le déphasage entre les parois. Quand les deux parois sont en phase, le diagramme de régimes est identique à celui obtenu pour un canal à parois planes. Lorsque les deux parois sont décalées, l'augmentation de l'ondulation de la paroi entraîne une augmentation des zones de transport et de sédimentation dans le diagramme. En considérant l'asymétrie entre les ondulations des deux parois, l'augmentation de l'ondulation de la paroi supérieure par rapport à celle de la

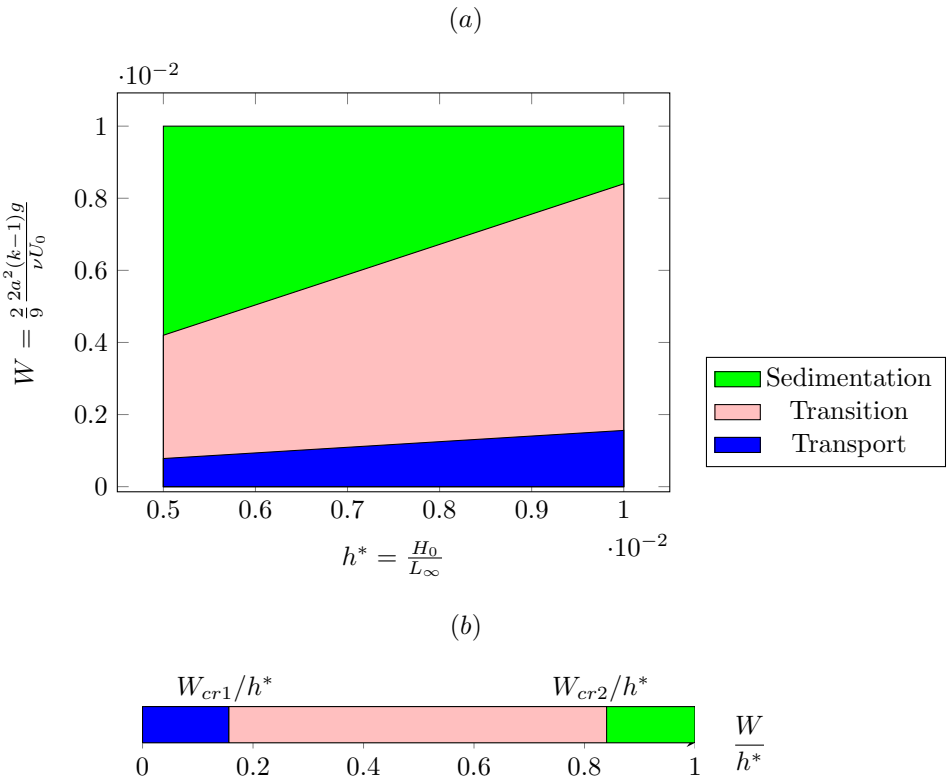

Figure 2: Diagramme de régimes de transport de particules dans un canal á parois planes. (a) représentation 2D des différentes zones selon la variation de W en fonction de h^*(b) représentation 1D de ces zones selon $\dfrac{W}{h^*}$.

paroi inférieure tend à diminuer la zone de transport et à augmenter la zone de sédimentation. Le diagramme de régimes et les effets des paramètres géométriques sur la variation de ses zones sont vérifiés par des expériences numériques menées en injectant 100 particules dans le canal et en calculant les pourcentages de particules qui se déposent à l'intérieur du canal.

Les principaux résultats de ce chapitre ont été publiés dans le "European Journal of Mechanics B/Fluids" (Hajjar et al. [1]).

Chapitre 4

Le modèle analytique proposé au chapitre 3, sous l'hypothèse que l'inertie des particules est négligée et que l'écoulement suit la loi cubique locale (LCL), a été vérifié numériquement via la résolution numérique des équations de NS et en prenant en compte l'inertie des particules. Pour aller plus loin, une validation expérimentale est nécessaire, afin de considérer

des situations réelles et d'évaluer la validité du modèle analytique sur une base pratique. Par conséquent, ce chapitre est dédié au modèle expérimental. La première partie du chapitre est consacrée à la présentation de la conception et à la mise en place du modèle physique. Ensuite, la procédure expérimentale et la méthodologie utilisée pour traiter les données expérimentales sont décrites. Enfin, plusieurs résultats préliminaires sont présentés et discutés vis-à-vis des objectifs initiaux de l'étude. Le dispositif est utilisé pour effectuer une étude préliminaire du transport des particules dans les fractures avec des parois planes et/ou sinusoïdales, ayant des dimensions conformes aux hypothèses théoriques formulées dans les chapitres précédents.

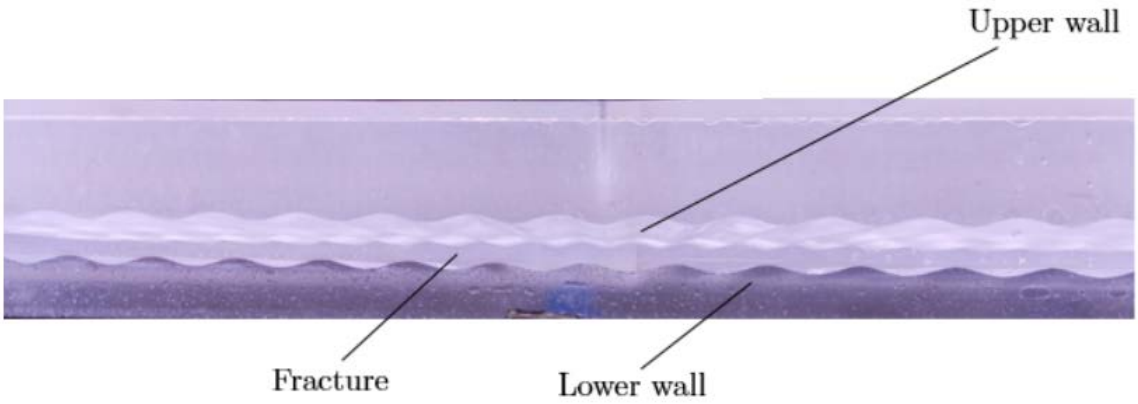

Figure 3: Modèle d'une fracture à parois sinusoïdales utilisées dans les expériences

Les résultats obtenus montrent que le banc expérimental est capable de reproduire les différents comportements des particules dans les fractures, tels que le transport et la sédimentation, ainsi que la focalisation inertielle. De nombreux tests ont été effectués en utilisant comme fluides l'eau et un mélange eau-glycérine, et des graines de pavot comme particules polydispersées. En choisissant une différence optimale de charge hydraulique, les effets inertiels de l'écoulement sont réduits et les résultats expérimentaux sont en accord avec la solution analytique. La distance parcourue par les particules jusqu'à leur sédimentation est dans la plage prédite par le modèle analytique développé. Ceci suggère que la solution analytique peut être utilisée afin d'évaluer la distance de sédimentation des particules polydispersées dans les fractures à parois planes et/ou sinusoïdales. Lorsque la charge hydraulique augmente, i.e., pour Re plus élevé, on observe que, dans les fractures à parois planes et sinusoïdales, les particules se focalisent sur une seule trajectoire, vérifiant ainsi la

présence d'une focalisation inertielle des particules. Ce résultat vérifie l'hypothèse que le modèle analytique n'est valide que pour un faible Re.

En conclusion, les résultats expérimentaux préliminaires confirment le modèle analytique développé dans cette thèse. En plus, ces résultats démontrent la capacité du dispositif expérimental à étudier le transport des particules dans les écoulements en canaux fermés. Il peut être judicieusement utilisé pour de futures études expérimentales sur le transport de particules, ce qui peut améliorer notre compréhension du comportement des particules et valider les modèles déjà développés.

Conclusion

Dans l'ensemble, les résultats obtenus dans cette thèse améliorent notre compréhension du comportement de petites particules immergées dans les écoulements à travers des canaux fermés, avec une application directe au transport des contaminants dans les fractures. Par exemple, on peut identifier, en fonction de leur taille et de leur densité, les contaminants susceptibles de se déposer à l'intérieur de la fracture ou être en suspension et transportés sur de longues distances. Ces résultats ont d'autres applications dans la filtration de l'eau et dans la séparation des minéraux. En effet, sur la base de nos diagrammes de régime, un système de séparation basé sur la sédimentation de particules dans des canaux à parois sinusoïdales pourrait être envisagé. Cela permettrait de séparer les particules en fonction de leur taille et/ou de leur densité en fonction de la distance à laquelle elles se déposent dans le canal. Comme l'écoulement dans le canal peut simplement être créé par une différence de charge hydraulique, l'avantage d'un tel système par rapport aux techniques de séparation actuelles est qu'il est passif et ne nécessite pas une importante alimentation en énergie. Une autre application concerne la focalisation inertielle qui peut trouver des échos en microfluidique. Tout d'abord, les résultats obtenus peuvent conduire à une quantification des conditions (Re et taille des particules) dans lesquelles la focalisation devient efficace. Deuxièmement, on a pu observer la focalisation inertielle dans les canaux à parois sinusoïdales. Des analyses supplémentaires pourraient révéler de nouvelles caractéristiques à l'origine du phénomène de focalisation, comme par exemple l'effet de la courbure des parois des canaux sur les forces

de portance inertielles agissant sur les particules.

Contents

GENERAL INTRODUCTION **27**

1 STATE OF THE ART **31**

1.1 Particle-laden flows: Basic concepts 31

1.1.1 Definition of particle inertia 34

1.1.2 Particle transport in closed channel flows 36

1.1.3 Focusing phenomena in closed channels 38

1.1.3.a. Lift-induced inertial migration 38

1.1.3.b. Preferential accumulation of particles in periodic channels . . 38

1.2 Flow in channels with flat and corrugated walls 39

1.2.1 Modeling flow in rough fractures 41

1.2.2 Inertial effects in fracture flows 44

1.2.3 Idealized model of fracture geometry 46

2 SINGLE PHASE FLOW THROUGH FRACTURES **49**

2.1 Geometrical description of fractures with corrugated walls 53

2.2 Governing equations 56

2.2.1 Flow between parallel flat walls: the cubic law 57

2.2.2 Flow between corrugated walls: the local cubic law 58

2.2.3 Flow velocity components in corrugated channels 60

2.3 Influence of the fracture geometry on its hydraulic aperture 61

2.3.1 Δx effect 62

2.3.2 γ effect 63

2.4 Influence of the fracture geometry on the validity of the LCL for different Reynolds numbers . . . 64
2.4.1 Numerical Method . . . 65
2.4.2 Low Re (< 1) . . . 66
2.4.2.a. Relative error between the LCL and NS solutions for three reference geometries . . . 66
2.4.2.b. Influence of ϵ, δ_0, γ and Δx on the relative error between the LCL and NS solutions . . . 67
2.4.3 High Re (> 1) . . . 71
2.4.3.a. Relative error between the LCL and NS solutions for the reference geometries . . . 72
2.4.3.b. Influence of ϵ, δ_0, γ and Δx on the relative error between the LCL and NS solutions . . . 73
2.5 Discussions . . . 77
2.5.1 Relation between the hydraulic and the mean apertures . . . 77
2.5.2 Validity of the local cubic law for different Reynolds numbers . . . 78
2.6 Conclusion . . . 83

3 TRANSPORT AND DEPOSITION OF WEAKLY-INERTIAL PARTICLES IN FRACTURE FLOWS 85

3.1 Governing equations . . . 87
3.1.1 Forces acting on each particle . . . 87
3.1.2 Particle motion equation and particle trajectory equation . . . 92
3.1.2.a. Focusing of weakly inertial particles in channels with periodic walls . . . 94
3.1.2.b. Trajectory equation of inertia-free particles . . . 95
3.1.2.c. Channel with flat walls . . . 97
3.1.2.d. Channel with sinusoidal walls . . . 98
3.2 Numerical verification . . . 99
3.2.1 Simulation procedure . . . 100

3.2.2 Results . . . 101
3.2.2.a. Particle focusing . . . 101
3.2.2.b. Particle trajectories . . . 102
3.3 Particle transport regime diagrams . . . 107
3.3.1 Channel with flat walls . . . 108
3.3.2 Corrugated channel with sinusoidal walls . . . 110
3.3.2.a. Channel with in phase walls . . . 111
3.3.2.b. Channel with out of phase identical walls . . . 112
3.3.2.c. Channel with maximum phase lag between the walls . . . 116
3.3.3 Summary . . . 119
3.4 Conclusion . . . 120

4 EXPERIMENTAL INVESTIGATION OF PARTICLE TRANSPORT IN FRACTURE FLOWS 123

4.1 Experimental setup and procedure . . . 127
4.1.1 Open channel with closed circuit flow . . . 127
4.1.2 Fractures with flat and sinusoidal walls . . . 129
4.1.3 Liquid properties . . . 134
4.1.4 Visualization and image treatment . . . 136
4.2.4.a. Lighting . . . 136
4.2.4.b. Camera and bench . . . 136
4.1.5 Experimental procedure and image treatment . . . 137
4.2 Preliminary results with poppy seeds . . . 140
4.2.1 Particle properties . . . 141
4.2.2 Transport with water as the operating liquid . . . 142
4.3.2.a. Trajectory of a single particles . . . 143
4.3.2.b. Inertial focusing of two particles . . . 144
4.2.3 Transport with water-glycerin mixture as the operating liquid . . . 145
4.3.3.a. Fracture with two flat walls . . . 146
4.3.3.b. Fracture with a flat wall and a sinusoidal wall . . . 148

4.3.3.c. Fracture with two sinusoidal walls 150
4.3 Conclusion 153

CONCLUSION AND PERSPECTIVES **155**

List of symbols

Length, velocity, and time

H_0	fracture aperture
L_∞	fracture length
L_0	wavelength of corrugations
$A_{1,2}$	Walls corrugation amplitudes
A_0	mean corrugation amplitude
V_0	flow mean velocity
T_0	time scale

Particle and fluid properties

a	particle radius
ρ_p	particle density
ρ_f	fluid density
ν	fluid kinematic viscosity
μ	fluid dynamic viscosity
$\vec{g}$	gravity acceleration

Particle and fluid velocities

$\vec{x_p}$	particle position
$\vec{v_p}$	particle velocity
$\vec{v_f}$	fluid velocity field
ψ	fluid stream function

fracture geometry

$\phi_{1,2}$	fracture walls shape
$h(x)$	fracture half-aperture
$\phi(x)$	fracture middle line
$\eta(x,z)$	cross-channel coordinate
ϵ	fracture aspect ratio
δ_0	dimensionless corrugation amplitude
γ	asymmetry of walls corrugations
Δx	phase shift
α	dimensionless phase lag

Dimensionless numbers

Re	Reynolds number
St	Stokes number
k	density ratio
$R = \frac{2}{2k+1}$	density ratio
$W = \frac{2}{9}\frac{a^2(k-1)g}{\nu V_0}$	velocity ratio

GENERAL INTRODUCTION

Understanding the transport and deposition of small particles in closed channel flows is of fundamental importance in many environmental issues, such as underground pollution and sediment transport, and in several industrial applications, like water filtration and mineral separation. Other applications concern energy extraction processes like the injection of proppants in petroleum reservoirs, and medical and biological research like the deposition of inhaled particles in human airways and cell sorting and separation in microfluidics. In earth sciences, the transport of contaminants in rough fractures is a crucial research topic due to its tight relation with water contamination in aquifers.

In such a context, the present thesis is devoted to the investigation of the transport and deposition of small solid particles in closed channel flows, with application to fracture flows. In particular, fractures with flat and corrugated periodic walls are considered. The main objective is to determine the conditions under which the particles will settle inside the fracture or, on the contrary, be transported over long distances. Several parameters must be considered in order to study the behavior of particles immersed in a moving fluid. First, the physical properties of the particles such as their size and density must be known to determine the forces acting on them. For instance, for sub-micron particles, Brownian diffusion dominates particle behavior and can be considered for studying particle transport. On the other hand, the transport of larger particles, which are insensitive to Brownian diffusion, depends directly on the forces acting on the particles due to gravitational and hydrodynamical effects. Normally, increasing the particle size and/or density tends to favor particle deposition due to the predominance of gravitational effects on their behavior. Second, the characteristics of the flow such as its velocity and the fluid viscosity and density are also important factors that must be taken into account for modeling correctly particle behavior. Increasing the

fluid viscosity, for example, tends to enhance the transport of particles for longer distances due to greater friction forces between the fluid and the particles. Finally, the effects of the channel geometrical properties related to its aperture and to the wall corrugations on particle behavior must be comprehended.

Before addressing particle-laden flows, it is important to have a precise description of the fluid flow itself. In the case of rough fractures, a well-known model commonly used to describe the flow is the local cubic law (LCL), which is an approximate analytical solution of the Navier-Stokes (NS) equations for viscous laminar flows through thin channels. However, the LCL applicability remains arguable. In fact, a certain discrepancy emerged in the criteria proposed by different authors for its validity. This is due to the fact that the previous studies have been performed with specific fracture geometries. This discrepancy motivated the first part of our work. In particular, a thorough numerical study is conducted in order to to investigate the effect of the fracture geometry on the validity of the LCL under different geometrical and kinematic conditions. This investigation is necessary since the LCL constitutes the basis of our study aiming to model particle transport and depositions in fracture flows.

To sum up, this thesis is an attempt to answer the following questions:

- Is the LCL a suitable model of fracture flow and what are the effects of the fracture geometry on its validity?
- What are the effects of the particle properties and of the flow characteristics on the behavior of particles when immersed in fracture flows?
- How do the the geometrical properties of the fracture affect the particle behavior?

For the study of particle transport and deposition, we adopt three approaches:

- Analytical approach: Assuming that particle inertia is negligible, a simplified form of the particle motion equation is coupled to the LCL and an equation describing particle trajectories is developed. Particles can be tracked analytically and the distance at which the particle may deposit can be calculated. This equation relates a dimensionless number W to the fracture geometry. W depends on the particle properties and on the

flow characteristics. Based on W and on the geometrical properties of the fracture, arbitrary regimes of transport and deposition are defined, and regime diagrams are established.

- Numerical approach: Taking into account particle inertia, and solving the full NS equations, numerical simulations are conducted to confirm the ability of the analytical model to predict the behavior of particles immersed in fracture flows. The distances at which particles deposit inside the fracture are computed numerically and compared to the trajectory equation determined analytically. Numerical experiments are then conducted to assess the relevance of the regime diagrams.

- Experimental approach: An experimental apparatus has been designed and constructed, with the main aim of verifying the analytical model. Preliminary tests using poppy seeds as moving particles are conducted and experimental results are compared to the analytical predictions.

Outline of the thesis

This thesis consists of four chapters:

In chapter 1, we present the basic concepts of particle-laden flows and a bibliographic review is made regarding flow and particle transport in fractures.

Chapter 2 is devoted to the study of single-phase flows in fractures with sinusoidal walls. The numerical simulations aiming to assess the validity of the local cubic law are presented, and the results are discussed and compared to previous works.

In chapter 3, we introduce the analytical model describing the transport of weakly-inertial particles in closed channel flows. Numerical experiments aiming to verify the analytical model are also presented and discussed.

In chapter 4, the experimental apparatus that was designed for further validation and practical assessment of the analytical model is described. Preliminary experimental results using poppy seeds are presented.

Finally, the main results obtained throughout the thesis are summarized and the perspectives of the work are discussed.

Chapter 1

STATE OF THE ART

1.1 Particle-laden flows: Basic concepts

The term particle-laden flows refers to two phase flows in which a carrier fluid contains suspensions of particles. Such flows consist of a fluid phase, called continuous phase, and the collection of all the particles in the flow, called dispersed phase. They represent a complex medium where multiple interactions are developed between phases which may have different physical properties.

Examples of particle-laden flows include solid particles in a liquid or a gas, gas bubbles in a liquid, or liquid particles in a gas. They are ubiquitous in many situations, whether at the natural and environmental level like rain droplets in clouds, transport of sediments, and dust inhalation, or at the industrial level like solid-particle separation, bubble column reactors, and sprays.

The complete set of equations describing particle-laden flows are in general very complicated to be solved analytically or require high computation costs to be solved numerically. Therefore, some approximations are usually made to simplify the problem such as point-force particles or mixed multiphase flow. It is also typical to assume that the dispersed particles size is very small compared to the flow domain so that the suspension is diluted. This assumption can greatly simplify the problem by neglecting particle-particle interactions (like collisions) with respect to particle-fluid interactions.

The concentration of particles certainly affects the particle dynamics in the flow. Nonethe-

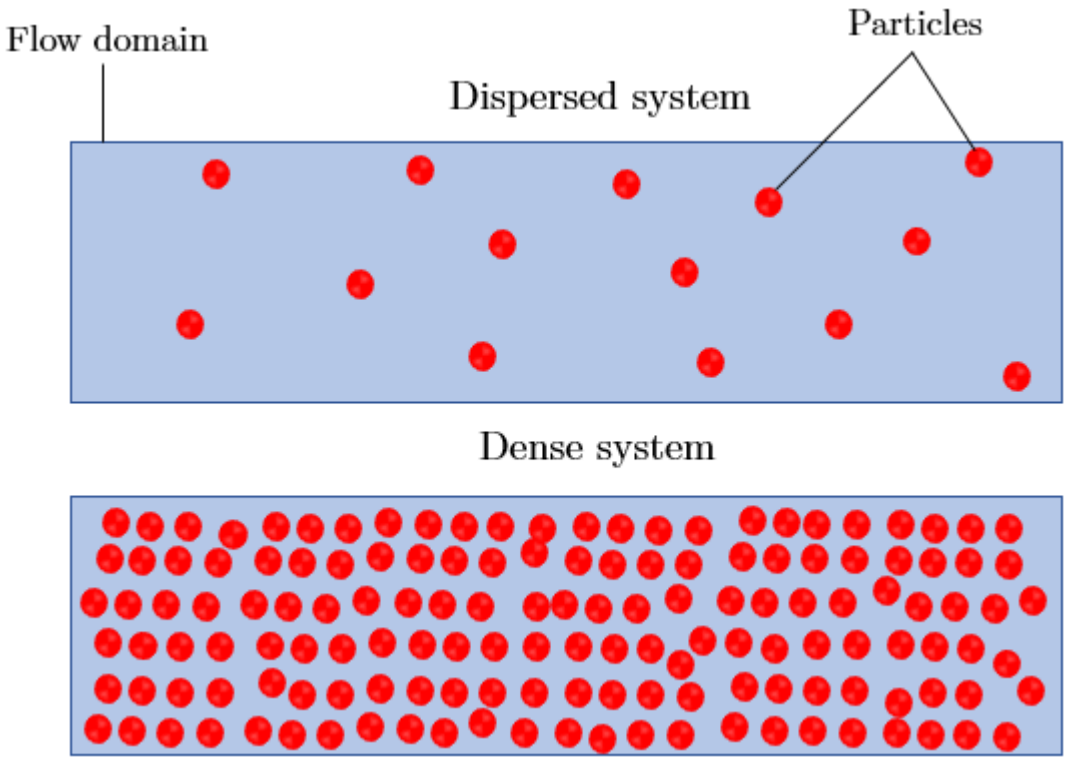

Figure 1.1: Schematic representation of the difference between dispersed and dense systems according to particle concentration

less, a distinction has to be made between dispersed systems and dense systems (Figure 1.1). In the latter case, as the concentration of the particles is high, particle motion is dominated by particle-particle interactions. On the other hand, in a dispersed system, particle dynamics is governed by the fluid hydrodynamical forces that prevail over particle-particle interactions. In this case, the concentration also defines the level of coupling between the dispersed and continuous phases. Generally, one-way coupling is considered when the particle concentration is very low so that their effect on the carrier fluid is neglected. The flow equations can then be solved independently from particle motion equations, which can be then solved using the corresponding flow fields at the particle position. For higher particle concentrations, particles can affect the flow by changing the local density and/or viscosity or the velocity field. In this case, the flow and particle motion equations are mutually coupled. In any case, to correctly predict the behavior of particle-laden flows, it is important to have an accurate description of the particle properties and flow characteristics. In addition, depending on the particle size, a distinction has to be made between colloidal and non-colloidal particles

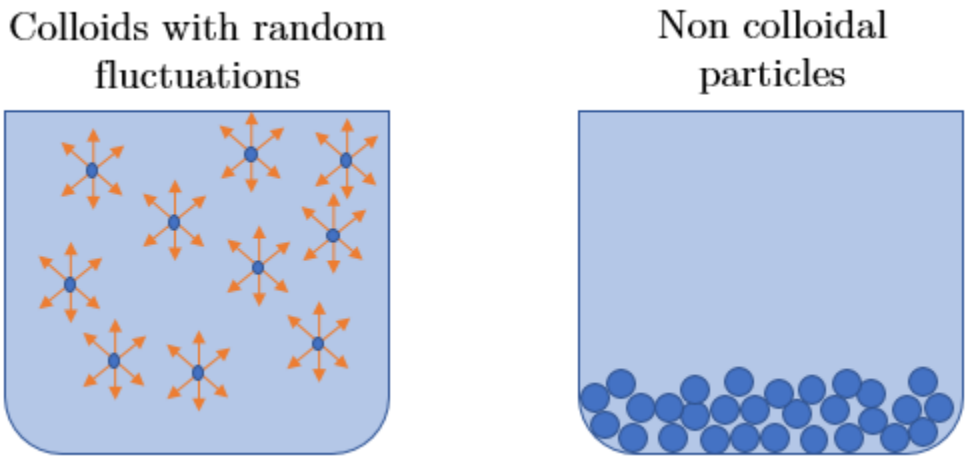

Figure 1.2: Suspended colloids with random fluctuations (Brownian motion) and non colloidal particles sedimenting due to their density.

(Figure 1.2). Colloids are very small particles, generally submicron-particles having a size ranging between $1\,nm$ and $1000\,nm$ (McCarty and Zachara [2], Kretzschmar et al. [3]), even though some studies suggest extending their size up to $10\mu m$ (Khilar and Fogler [4], Sen and Khilar [5]). Colloids are sensible to Brownian diffusion, i.e. the mechanism by which particles move (diffuse) from zones of higher concentration to zones of lower concentration (Jones [6]). Because Brownian diffusion dominates the other mechanisms in colloidal transport, colloids may be suspended in the fluid for long time periods. On the other hand, when the particle size increases, typically above $1\mu m$, Brownian effects become negligible and particle behavior is driven by external forces due to the interaction with the fluid and to potential external fields such as, for instance, gravity in the case of dense particles and electricity in the case of charged particles. An example of the distinction between particles based on their size can be found in the processes of water filtration. In figure 1.3, the different types of water contaminants which can be encountered in water filtration are illustrated, highlighting the difference between colloidal and non-colloidal particles.

Throughout this thesis, Brownian effects are neglected so that only non-colloidal particles are considered.

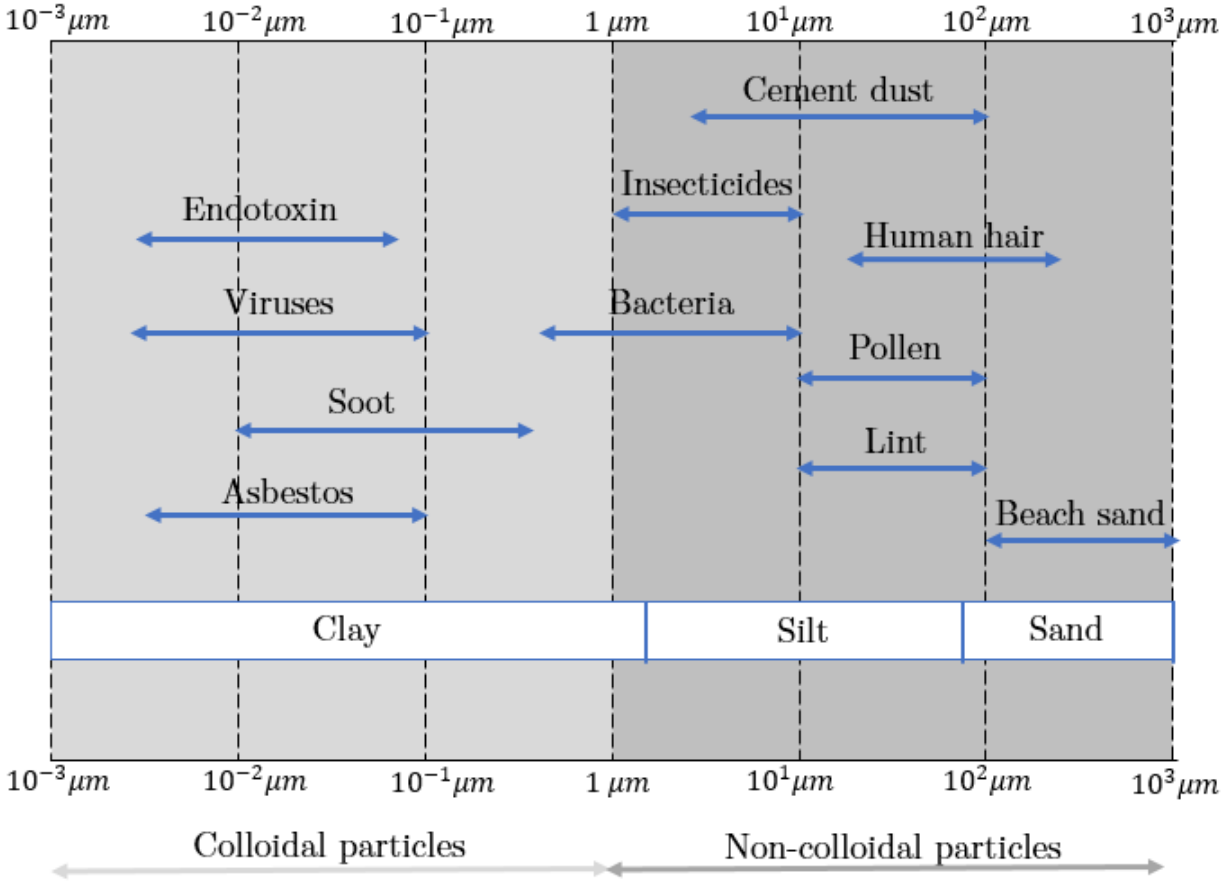

Figure 1.3: Different types of water contaminants encountered in water filtration and their sizes, including underground sediments (white rectangles). Adaptation of Water Quality Association source material.

1.1.1 Definition of particle inertia

To understand particle inertia, one can consider a case in which inertia is negligible. A good example for the latter situation is flow tracers, which are commonly utilized to measure flow velocity when combined with imaging techniques such as PIV and PTV. In fact, a tracer particle follows exactly the flow streamlines due to its small size and to having a density matching that of the carrier fluid.

The motion of a non-colloidal tracer can be simply described by:

$$\vec{v_p} = \vec{v_f} \tag{1.1}$$

where $\vec{v_p}$ and $\vec{v_f}$ are respectively the particle and fluid dimensionless velocities rescaled based

on the typical velocity scale of the flow.

When their size and/or density increase, particles have a proper dynamic and their trajectories deviate from the flow streamlines. These particles are called inertial particles. The motion of inertial particles can be very complex even when particles are passive and have non Brownian dynamics (Babiano et al. [7], Haller and Sapsis [8], Cartwright et al. [9], Balkovsky et al. [10]). This characteristic behavior of inertial particles has a great importance in many practical situations in earth sciences like oceanology (Lunau et al. [11]) and atmospheric sciences (Shaw [12]).

Another interesting feature of inertial particles is that, under the effect of their inertia, they tend to cluster or accumulate in well defined regions of the flow. This phenomena has been widely studied for different types of fluid flows (e.g. Eaton and Fessler [13] and Squires and Eaton [14] in turbulent flows, Bec [15] in random flows, Nizkaya et al. [16] in laminar spatially periodic flows, Angilella [17] and Angilella et al. [18] in vortex flows). This clustering ability of inertial particles can explain, for example, how rain in turbulent clouds can be enhanced by the accumulation of water droplets (e.g. Falkovich et al. [19]).

Moreover, particle inertia has a great effect on particle trajectories in fluid flows. For instance, Stommel [20] studied particle motion in cellular flow fields without taking into account particle inertia. He found that the particles' trajectories can be calculated according to the ratio between the particles settling velocity and the flows vortex velocity. Maxey [21] extended this concept by including the effect of particle inertia and found that two dimensionless numbers must be considered: Stokes number St, which characterizes particle inertia, and the particle to fluid density ratio.

By definition, St is the ratio between particle relaxation time t_p and the flow characteristic time t_0. t_p can be seen as the characteristic time of particle reaction to a change in the fluid velocity. If $St << 1$, then the particle will quickly adapt itself to the fluid velocity and acts as a tracer. On the other hand, for higher St, the particle will take longer time to respond to any change in the fluid velocity and will continue along its initial trajectory.

Unlike tracers, inertial particle motion is governed by a second order equation that can

be written in the following general form:

$$\frac{d\vec{v_p}}{dt} = -\frac{1}{St}(\vec{v_p} - \vec{v_f}) + \vec{f} \tag{1.2}$$

the term $-\frac{1}{St}(\vec{v_p} - \vec{v_f})$ being related to the drag force while $\vec{f}$ includes forces resulting from externally applied fields, such as gravity or other forces (electrical, magnetic...). If $St \to 0$ and if $\vec{f}$ is negligible (e.g. a neutrally buoyant particle in a gravity field), then equation (1.2) reduces to equation (1.1) and the particle is simply a tracer. When St increases and/or when f is not negligible, deviation from equation 1.1 appears and solving the particle motion equation is more complex. However, for small inertia, equation 1.2 can be solved based on an asymptotic expansion, St being the perturbation parameter.

1.1.2 Particle transport in closed channel flows

Closed channel flows define configurations where a fluid is moving inside closed conduits such as tubes, pipes or confined channels like fractures (Figure 1.4).

In this thesis, We consider 2D flows occurring in closed channels with flat and corrugated walls (Figure 1.5). In addition, we consider that the fluid fills the channel cross-section and there is no free surface of the fluid. In a hydrogeological context, such channels are commonly used to model rough fractures for example. Flows through these fractures can carry tiny particles such as rock sediments or organic debris. Depending on the particle physical properties, on the flow characteristics, and on the fracture geometry, these particles can have different behaviors. Most of previous works emphasizing on fracture flows focused either on solute transport (Therrien and Sudicky [22], Bouqain et al. [23], Oltéan et al. [24]) or on the transport of colloidal particles (Boutt et al. [25]).

Generally, for particle-laden flows through fractures, the macroscopic behavior of the particulate phase can be described by breakthrough curves, i.e. the plot of the variation of particle relative concentration as a function of time, where the relative concentration is defined as the ratio of the actual concentration to the one at the source. Breakthrough curves in previous experimental works have shown that particles are not simply advected like tracers and that particles velocity deviates from that of the fluid (Novawski et al. [26]).

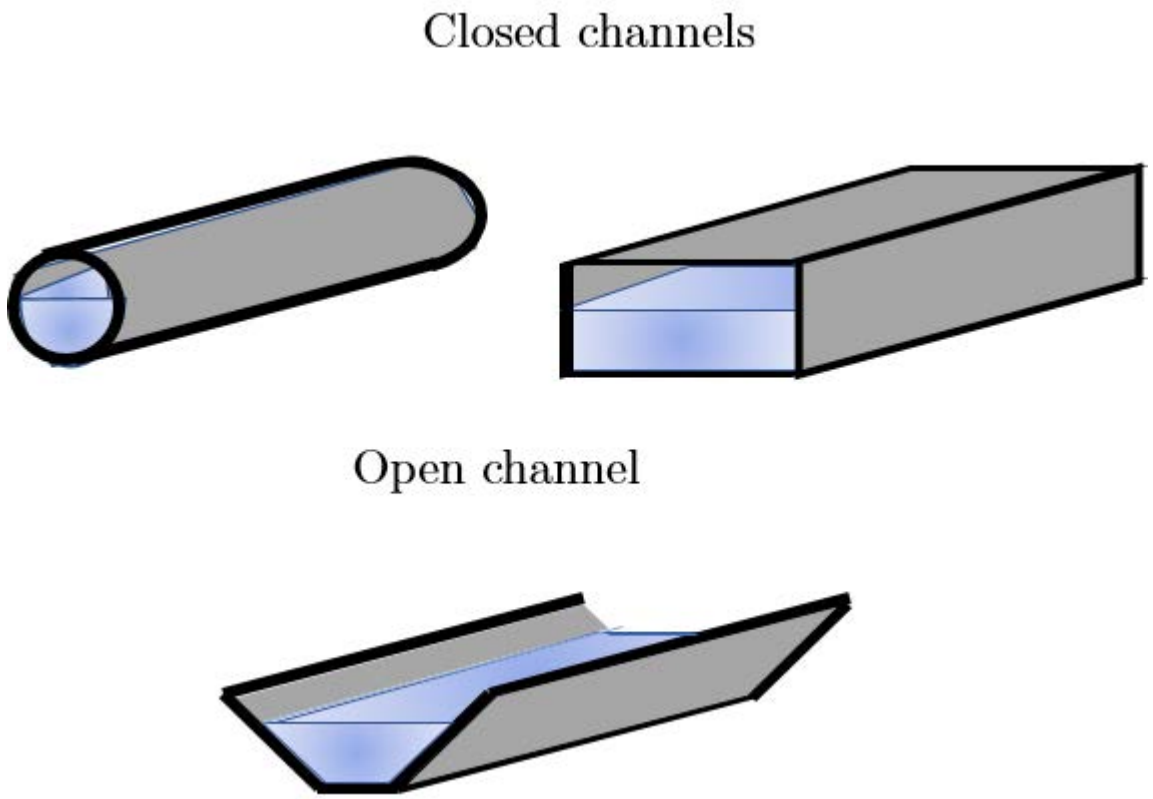

Figure 1.4: Examples of closed and open channels

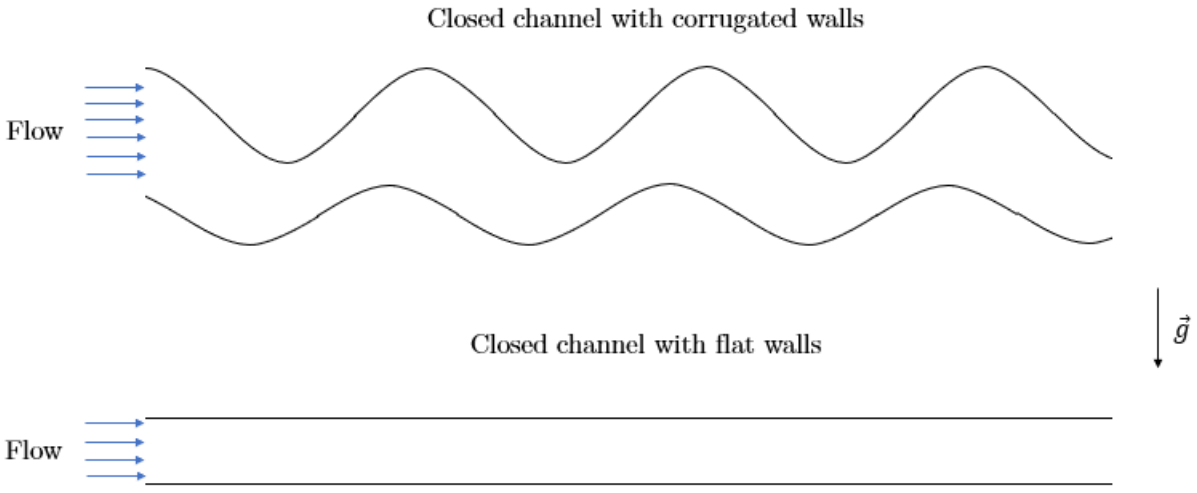

Figure 1.5: Closed channels with corrugated and flat walls considered in this thesis

This phenomenon was shown to be due to the effect of Brownian diffusion which leads to the redistribution of particles along the channel cross-section. However, this is not valid for larger particles that are not affected by diffusion. For example, the transport of such particles has been investigated by Nizkaya [27] and Nizkaya et al. [16] who showed how they can be accumulated in preferential regions and focus towards specific streamlines inside the flow. Another focusing phenomenon that is expected to occur in closed channels is particle focusing due to the lift forces that emerge when flow inertial effects are important. These two distinct phenomena of particle focusing are briefly described in the following section.

1.1.3 Focusing phenomena in closed channels

1.1.3.a. Lift-induced inertial migration

Both neutrally and non-neutrally buoyant particles can migrate across the flow streamlines to reach specific equilibrium positions within the channel (Figure 1.6). In fact, Segré and Silberberg [28] were the first to witness that particles in a laminar pipe Poiseuille flow congregate on an annulus located at a certain distance from the pipe centerline equal to 0.6 times the pipe radius. This phenomenon is known as the tubular pinch effect. Since then, this phenomenon has been studied extensively using theoretical (Schonberg and Hinch [29], Asmolov [30]), experimental (Karnis et al. [31], Matas et al. [32]) and numerical approaches (Feng et al. [33], Yang et al. [34]). These investigations concluded that inertial migration occurs due to forces that act on particles in inertial flows, known as the inertial lift forces. Recently, lift-induced particle focusing attracted much attention with the development of microfluidics where it has many applications, e.g. in cell separation and isolation in biological fluids (Di Carlo et al. [35], Martel and Toner [36]). The effect of inertial lift forces must be is explained in detail in the following chapters.

1.1.3.b. Preferential accumulation of particles in periodic channels

Unlike lift-induced particle focusing, accumulation or clustering of particles due to their inertia in liquid flows through channels with corrugated walls, remains a theoretical prediction yet to be verified experimentally (Nizkaya et al. [16]). Moreover, particle clustering is

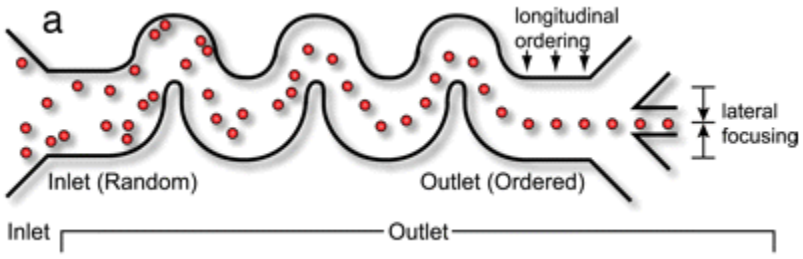

Figure 1.6: Lift-induced inertial migration in a serpentine channel (Di Carlo et al. [35]).

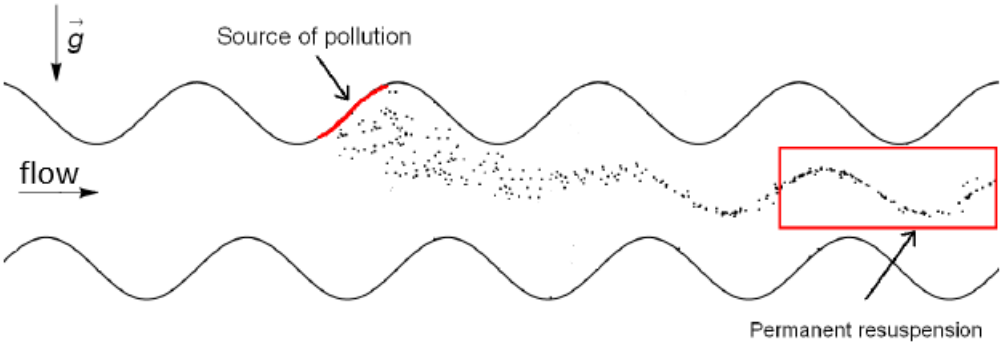

Figure 1.7: Accumulation of particles in a channel with corrugated walls as predicted by Nizkaya [27].

only limited to the case of periodic walls corrugations (Figure 1.7) as, in contrast with lift-induced migration, clustering can not occur in channels with flat walls. This phenomenon in which particles, with low but finite inertia, are expected to be attracted by a streamline, may occur for specific channel geometries and flow characteristics.

This phenomenon will be discussed later on with more details. Before that, the flow must be investigated.

1.2 Flow in channels with flat and corrugated walls

Channels with flat and corrugated walls have been studied extensively in earth sciences as a model of single rough fractures.

In fact, many studies have shown the importance of the fracture characteristics when considering flow in fractured geological systems, such as its orientation, its extent, and its interconnection with other fractures (Rasmussen [37]). Zhang et al. [38] showed that the hydraulic behavior of a fractured medium is largely influenced by the characteristic lengths

of the single fractures and their number (i.e. fracture density), and fracture orientations. Indeed, the properties of the flow occurring through a network of fractures are strongly controlled by those of the flow occurring through single or discrete fractures. For a network of fractures, the percolation theory is an appropriate technique for solving the permeability problems (Mourzenko et al. [39], Mourzenko et al. [40]). However, modeling flow in single fractures remains a key issue that needs to be properly understood before extrapolating to more complex configurations.

The parameters likely to intervene in the prediction of flow through single fractures have been gathered experimentally by Hakami and Larsson [41]. They noted that, apart from the effect of the fluid properties and pressure conditions on the fracture boundaries, fracture flow depends also on different geometrical parameters such as the aperture and spatial correlations related to the walls roughness. The roughness characterizes the morphology of the fracture walls, their general shape and their surface state. The term roughness encompasses very different morphological characteristics such as: amplitude (elevation of points on the surface), angularity (slopes and angles), waviness (periodicity), and curvature (Gentier [42], Belem [43]). The geometric description of the roughness and morphological characteristics of fractures is based on empirical, geometrical and statistical analyzes, which can be either geostatistical or fractal (Gentier [42], Belem [43], Mourzenko et al. [39], Plouraboué [44], Oron & Berkowitz [45], Lefèvre [46], Legrain [47]).

The roughness in its general sense has a multiplicity of characteristic length scales. However, in the literature, two main scales of roughness are usually highlighted (Figure 1.8). They are characterized and defined by their effects on the mechanical and hydraulic behavior of a fracture. It is important at this point to distinguish two types of roughness (Louis [48]). At the micro-scale level, roughness is related to irregularities in the surface of the walls. It may slightly increase the linear head loss inside the fracture. The macro-scale roughness characterizes the overall shape of the walls. It causes changes in flow direction and the shape of the streamlines. The concept of tortuosity is then often used in the literature. Tortuosity represents the ratio of the length of the trajectory of the flow between two points and the straight distance between these two same points, and, thus, it can has an important effect the behavior of the flow through rough fractures. The micro-scale roughness is neglected in

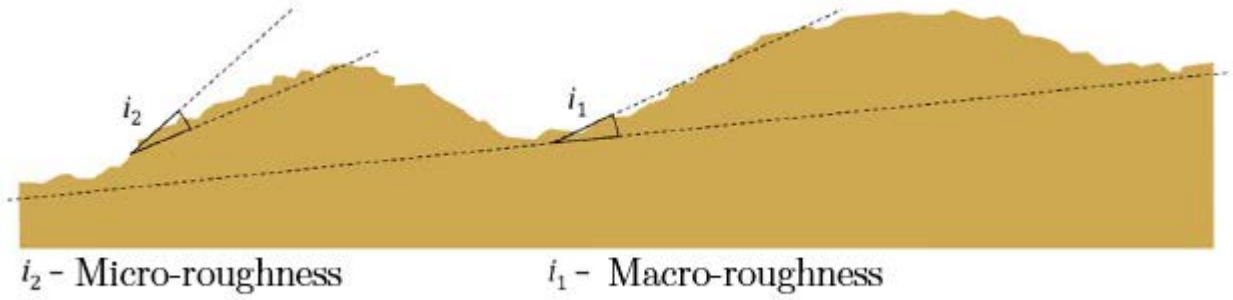

Figure 1.8: Different scales of roughness according to Dippenaar and Van Rooy [49]. i_1 represents first order waviness corresponding to the macro-roughness. i_2 represents second order asperities corresponding to the micro-roughness.

this thesis and only the effects of the macro-scale roughness on the behavior of fracture flow are considered.

1.2.1 Modeling flow in rough fractures

To model fluid flow in a single fracture, the standard laws of fluid mechanics can be used. These are the Navier-Stokes (NS) and continuity equations. Eventually, these equations can be simplified according to the channel geometry and/or assumptions regarding the flow, so that analytical solutions can be obtained to determine the pressure and velocity fields.

On the other hand, on a larger scale, the flow can be described by Darcy's law. Darcy's law relates the hydraulic gradient to the flow rate using an intrinsic parameter defined as the permeability. It can be obtained from the NS equation using an upscaling method such as volume averaging an homogenization (Whitaker [50]).

One of the most important characteristics of a rough fracture is its aperture. The aperture is defined as the distance between the fracture walls and implicitly depends on the way the roughness is defined. The aperture can be defined locally or globally according to geometrical criteria, mechanical criteria, or as a result of hydraulic experiments assuming a law for the flow. Consequently, the geometric mean, the mechanical and the hydraulic apertures can be distinguished (Lin [51], Davias [52], Crosnier [53]).

Early attempts to model flow in single fracture assumed that the flow occurs between two flat parallel plates representing the fracture walls (Bear [54]). This is known as the

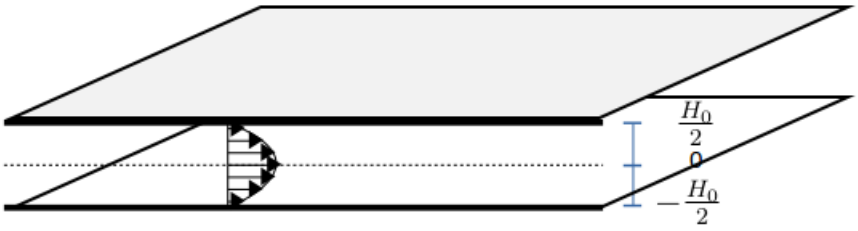

Figure 1.9: The parallel-plate model

parallel-plate model (Figure 1.9). This model is based on the observations stating that most natural fractures are approximately plane at the fracture length scale. Analytical solutions to the problem of laminar flow between parallel plates can then be easily obtained. In particular, for a 2D channel with flat walls of length L_∞ and aperture H_0, through which a fluid of density ρ and dynamic viscosity μ is flowing due to a pressure difference $\Delta P = \rho g \Delta Z$ between the inlet and the outlet of the channel, with ΔZ is the hydraulic head and g the gravity acceleration, the volumetric flow rate per unit width is given by:

$$Q = -\frac{\rho g {H_0}^3}{12\mu}\frac{\Delta Z}{L_\infty} \tag{1.3}$$

The volumetric flow rate per width is $Q = V_0 H_0$, V_0 being the mean velocity of the flow in the channel. In this case, the velocity has a parabolic profile (Figure 1.9)

At the same time, Darcy's law (Darcy [55]) gives a linear relation between the volumetric flow rate Q_v and the pressure drop ΔP:

$$Q_v = -\frac{KA}{\mu}\frac{\Delta P}{L} \tag{1.4}$$

where K is the hydrodynamic permeability and A is the cross-section on which Q_v is computed. In order to consider the flow rate per unit width Q, A can be replaced by H_0 and equation (1.4) thus becomes:

$$Q = -\frac{KH_0}{\mu}\frac{\Delta P}{L} \tag{1.5}$$

Replacing equation (1.3) in equation (1.5), the permeability of the channel is equal to

$K = \frac{H_0^2}{12}$, and, therefore, the channel transmissivity can be computed as $T = KH_0 = \frac{H_0^3}{12}$. Since T is proportional to the cube of the aperture, equation (1.3) is known as the cubic law (CL) (D.M. Brown [56], S.R. Brown [57], Silliman [58], Chen et al. [59], Konzuk and Kueper [60], Dippenaar and Van Rooy [49]). If the CL is valid for large fracture apertures, i.e. when walls macro-roughness can be neglected, it tends to overestimate the flow rate if the roughness and the aperture have the same order of magnitude. In this case, the two walls can not be modeled as flat plates and the local aperture varies along the flow direction, an effect that is not taken into account in equation (1.3). However, the CL can accurately predict the flow rate in a rough fracture when the apparent aperture H_0 is replaced by a fitting parameter calculated from experimental data and obeying equation (1.3) (Whitherspoon et al. [61]). This parameter is called the hydraulic aperture H_h. Attempts to match the measured flow rates to the hydraulic head as predicted by the CL have been made using different aperture definitions such as the arithmetic mean (Brown [57]), the geometric mean (Tsang and Tsang [62], Renshaw [63]), the harmonic mean (Unger and Mase [64]) and the volume-averaged mean (Hakami and Barton [65]) of local apertures or by applying correction factors to include other information about the fracture (Whitherspoon et al. [61], Gutfraind and Hansen [66], Neuman [67], De Vallejo and Ferrer [68]). A comparative evaluation of the different definitions of the aperture can be found in the work presented by Konzuk and Kueper [60].

Instead of matching the measured flow rates to the predictions of the CL, a different approach consists in considering the spatial variation of the aperture along the flow direction, implying that the CL is valid locally along the fracture length and leading to the known local cubic law LCL. In fact, fluid flow through rough fractures can be fully described by the NS equations (Zimmerman and Bodvarsson [69]). However, the non-linearity of the inertial term in these equations makes them difficult to be solved analytically without the use of perturbation expansions (Hasegama and Izuchi [70], Basha and El Asmar [71]). When the flow inertial effects are negligible, the NS equations reduce to the Stokes equation. Furthermore, when the channel aperture varies slowly along the flow direction, Stokes equation can be further reduced to Reynolds equation also known as the LCL (Zimmerman et al. [72]). The development of the LCL based on the NS equation is detailed and discussed in the

next chapter.

1.2.2 Inertial effects in fracture flows

At the macroscopic level, fracture flow is characterized by the relation between the volumetric flow rate Q_v and the pressure drop ΔP applied between the fracture inlet and outlet. At low flow rates, this relation is linear and is described by Darcy's law (equation (1.4)). For low Q_v, the permeability K depends only on the fracture geometry. When Q_v increases, experimental investigations showed that the variation of Δh as a function of Q_v deviates from the linear defined in Darcy's law (e.g. Firdaouss et al. [73]). This deviation is due to the inertial effects developing in the flow and to the walls corrugation (Bear [54], Dybbs and Edwards [74]). The intensity of flow inertial effects allows the separation between Darcian and non-Darcian regimes and is characterized by the Reynolds number $Re = \frac{V_0 H_0}{\nu}$, $V_0 = \frac{Q}{A}$ being the flow mean velocity, H_0 is the characteristic length, and ν is the fluid kinematic viscosity.

For low and moderate Re, when the inertial and viscous forces in the liquid are of the same order of magnitude, the deviation of Darcy's law is cubic in Q_v (proportional to Q_v^3). This cubic deviation was later confirmed by many theoretical investigations (Firdaouss et al. [73], Skjetne and Auriault [75], Jacono et al. [76]). For higher Re, inertial effects can lead to the appearance of recirculation zones in the flow (Figure 1.10). They are due to the viscous shear stresses resulting from the fluid momentum mismatch in the channel center and near-wall regions. The central fluid moves faster than the quasi-stagnant fluid close to the channel walls, causing thus fluid recirculations within the channel furrows. Such zones can theoretically appear even in Stokes flows, but only when the aperture variations are important (Kitanidis and Dikaar [77], Malevich et al.[78]). Due to the presence of recirculation zones at high Re, the deviation from Darcy's law is quadratic in Q (Forchheimer regime [79]). In this case, the deviation is due to energy dissipation that may be explained by the loss of kinetic energy occurring when single jets tend to penetrate into the separating line between the main flow and the recirculation zone (Lucas et al. [80]). Therefore, it is convenient to define the flow regimes as follows:

- Viscous regime: inertial forces are negligible with respect to viscous forces. This is a

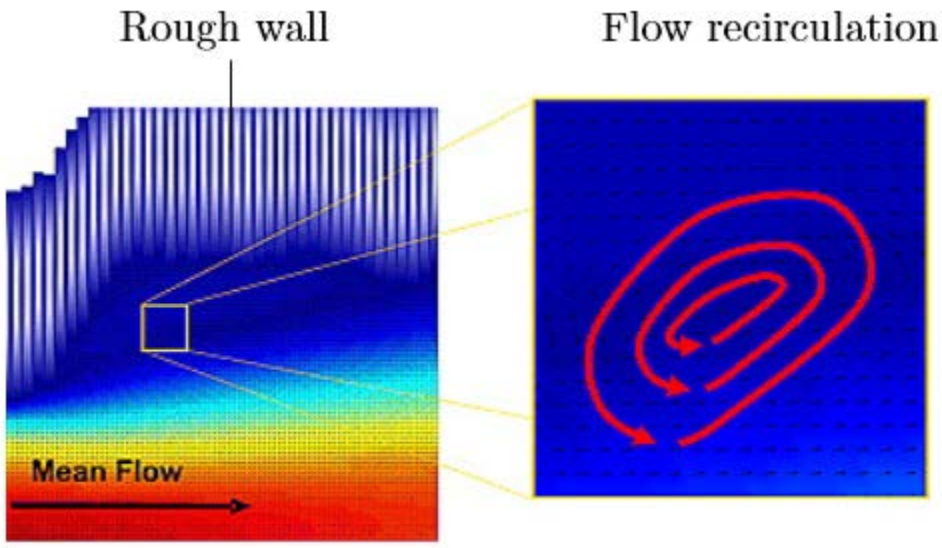

Figure 1.10: Recirculation zones appearing in a fracture with rough walls as identified by Boutt el al. [25].

Darcian regime in which the variation of ΔP as a function of Q_v is linear.

- Transition regime: viscous and inertial forces are of the same order of magnitude. The deviation from Darcy law is cubic in Q_v. This regime is also known as weakly inertial regime.

- Inertial regime: viscous forces are negligible with respect to inertial forces. The deviation from Darcy law is quadratic in Q_v.

In this thesis, fracture flow is investigated for low and moderate Re. Investigating the onset of creation of recirculation zones as well as the effect of the channel geometry on their appearance in the inertial regime is not part of the study and will thus not be addressed.

The CL and LCL provide simple relationships relating the hydraulic aperture of a fracture to its permeability, given that the flow is Darcian. For high Re, when the flow becomes non-Darcian, the validity of the CL and of the LCL becomes questionable. The applicability of these models must then be assessed before considering them to model fracture flow.

1.2.3 Idealized model of fracture geometry

Although real fractures have 3D geometries, 2D geometries can be considered for simplification sake. Indeed, the fracture aperture is practically many orders of magnitude smaller than its width. If the fracture is presented in a reference frame (X, Y, Z), where X is in the main flow direction (along the length), Y is in the orthogonal direction (along the width) and Z is in the vertical direction (along the aperture), it is reasonable to assume an invariance of the velocity field in the Y direction and to study the system in the 2D referential (X,Z). In this context, Zimmerman et al. [81] showed that a 2D model in which the aperture varies only in the flow direction gives qualitatively the same results as a full 3-D model.

In order to study analytically flow and transport in fractures, a geometrical model that best represents the fracture characteristics must be used. Power and Tullis [82] showed that natural rock fractures, despite having self-affine properties, can be described by the sum of multiple sine waves with equal amplitude to wavelength ratios. This means that the walls roughness, even if irregular, has an oscillatory nature and can be represented by a regular corrugation, which leads to the sinusoidal fracture model.

The configuration in which the profiles of the walls vary sinusoidally along the length can be used as a model of real fractures because, it captures their oscillatory nature, as well as the effects of the walls roughness and of the aperture variation on the flow. Actually, Le Borgne et al. [83] showed that velocity distribution in sinusoidal channels are very similar to that obtained in more complex medium.

The difference between using the parallel plate model and the sinusoidal model is shown in Figure 1.11. On the one hand, it is obvious that the parallel plate model does not take into account surface roughness. It presents a constant aperture and a geometry that would not affect the flow streamlines inside the channel. On the other hand, the sinusoidal model, despite not following exactly the real roughness profile, can still take into account the aperture variation and the effect of the channel walls on the flow geometry. These are the reasons why channels with sinusoidal walls have been then widely used to represent rough fractures (Zimmerman et al. [81], Brown et al. [84], Zimmerman and Bodvarsson [69], Waite et al. [85], Sisavath et al. [86],Basha and El Asmar [71], Yeo and Ge [87], Nizkaya [27], Liu and Fan [88], Renu and Kumar [89])

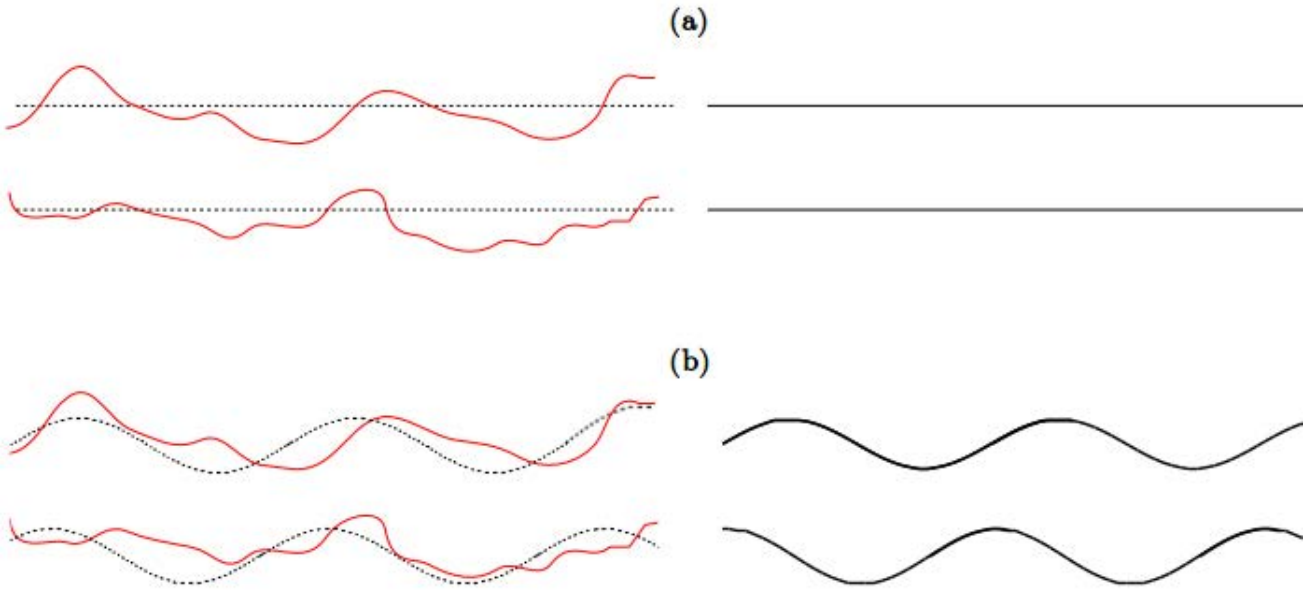

Figure 1.11: Fracture with irregular roughness modeled as a channel with parallel flat walls (a) and a channel with sinusoidal walls (b).

It is convenient also to notice that sinusoidal channels have been used to model homogeneous porous media. For instance, porous media can be modeled as a set of uniform spherical grains regularly stacked. In this case, a 2D simplification of a representative elementary volume can lead to a sinusoidal channel that accounts for the aperture variation inside the medium. This simplification has been widely applied to study flow and solute dispersion in porous media (Kitanidis and Dikaar [77], Edwards et al. [90], Bolster et al. [91], Bouquain et al. [23]).

Throughout the thesis, sinusoidal variation will be considered to represent walls corrugation. Other than representing fracture roughness, such geometry is convenient for setting up numerical simulations and experimental devices aiming at studying fracture flow.

Chapter 2

SINGLE PHASE FLOW THROUGH FRACTURES

In order to study particle transport, it is crucial to consider a model that can describe accurately the fluid flow. Different models were used in hydrogeology for investigating flow through single rough-walled fractures. Idealizing the fracture as a channel with two flat walls simplifies greatly the problem and enables to find an analytical solution for the velocity field, known as the cubic law (CL). Taking into account walls corrugation and considering slowly varying apertures, Reynolds equation can be used and leads to the local cubic law (LCL), which gives expressions of the velocity components depending the fracture geometry. However, the validity of the CL and the LCL remains questionable. Indeed, there exist some criteria, strictly related to the fracture geometry, for the applicability of these two laws. In this chapter, we propose a numerical study aiming to assess the validity of the CL and of the LCL by considering different fracture geometries. The fractures are represented by channels with sinusoidal walls having different geometrical properties defined the channel aperture, the amplitude and the wavelength of the walls corrugation, the corrugations asymmetry and the phase shift between the two walls. The validity of the CL and of the LCL is evaluated for Reynolds number in the range $[6.7 \times 10^{-2}, 6.7 \times 10^{1}]$.

Introduction

Flow in rough-walled fractures is governed by the Navier-Stokes (NS) equations (Zimmerman and Bodvarsson [69]. However, the non-linearity of the inertial term in these equations makes their solution very difficult to be obtained without the use of perturbation expansions that may give approximate solutions (Hasegaw and Izuchi [70], Basha and El Asmar [71]). As pointed out in chapter 1, a fracture can be approximated as a channel with two flat parallel walls. This approximation simplifies the problem and leads to an analytical solution of the NS equations known as the CL. Another approximation consists in considering that the fracture aperture varies slowly and the Reynolds equation, i.e. the LCL, can then be used.

However, several authors have shown that Reynolds equation tends overestimate the flow rate in rough-walled and corrugated fractures depending on their geometry and the flow characteristics (Mourzenko et al. [92], Brown et al. [84], Nicholl et al. [93], Lee et al. [94]). Indeed, there are some restrictions related to the flow and to the fracture geometry for the Reynolds equation, and thus for the LCL, to be valid. First, different geometrical criteria have been proposed for the validity of the LCL. For instance, Zimmerman et al. [81], by applying the perturbation approach of Hasegawa and Izuchi [70] to fractures with mirror-symmetric sinusoidal walls, found that Stokes equation can be replaced by Reynolds equation only if the ratio between the wavelength of the wall and the standard deviation of the local apertures is higher than five. Using a similar approach with a fracture consisting of a flat wall and a sinusoidal wall, Zimmerman et al. [72] suggested that the wavelength of the walls must be higher than three times the arithmetic mean of local apertures for Reynolds equation to be valid. Later on, Yeo and Ge [87] performed numerical simulations of flow in fractures with sinusoidal parallel walls with different corrugation amplitudes, and identified a criterion relating flow tortuosity and walls roughness for Reynolds equation to be applicable. On the other hand, the influence of the flow characteristics on the validity of the LCL has been investigated. The LCL is generally considered valid for viscous flows when $Re < 1$ ([95], [96], [60]). When Re increases, flow inertial effects become significant and thus the deviation of the LCL from the NS equations increases. The first inertial corrections to

the solution given by the lubrication theory were found by [97]. Second order corrections were then calculated for specific geometries, like for instance, the case of a fracture having a flat wall and a corrugated wall ([70]), the case of a fracture with parallel walls ([98]) or for mirror-symmetric fractures ([53], [99] in the case of a radial fracture). [71] and [27] generalized these results by calculating the inertial corrections for corrugated fractures with arbitrary walls.

Besides, numerous studies have focused on the determination of the hydraulic aperture, i.e. the aperture of a fracture with flat walls that would have the same permeability as the actual rough fracture. For example, in order to relate precisely the hydraulic aperture to the walls roughness and to the fracture mean aperture (known also as the mechanical aperture), Sisavath et al. [86], following the method of Van Dyke [97], used a perturbation approach to study fluid flow in a sinusoidal fracture undergoing dilatation or closure, and developed an expression for the hydraulic aperture taking into account a resistance term that can not be simply deduced from Reynolds equation. This result is valid for fractures with mirror-symmetric walls and is similar to the one obtained by Hasegawa and Izuchi [70] for flow through fractures consisting of a corrugated wall and a flat wall. Later on, Liu et al. [88] improved this expression of the hydraulic aperture by taking into account the roughness, the mean aperture, and the phase shift between the two walls. All these results clearly demonstrated that the hydraulic aperture deviates from the mean aperture in rough fractures.

Several attempts were made to modify the LCL in order to take into account the surface roughness, the tortuosity, the friction loss and the flow inertial effects, with different definitions of the mean aperture, like the geometric mean, the arithmetic mean and the true aperture (Ge [100], Konzuk and Kueper [60], Mallikamas and Rajaram [101], Qian et al. [102], Wang et al. [103], Chen et al. [104]). These modifications were able to reduce the over-prediction of the flow rate by the LCL.

Nevertheless, it would be convenient, when studying fracture flow in rough fracture with applications ranging from particle and solute transport to heat and mass transfer, to use the LCL, or the CL. Indeed, they give a direct and relatively simple relationship between the flow rate and the pressure difference and lead to an explicit expression of the velocity

components inside the fracture. However, many issues must be resolved before using the LCL for modeling the fracture flow. First, the criteria proposed in the literature regarding the applicability of the LCL present certain discrepancy among authors. Most likely, the discrepancy arise from the specific fracture geometry considered by each one of these authors. In addition, to our knowledge, none of the available studies provides a quantification of the relative error between the LCL and the NS equations for arbitrary geometries, i.e. when the two walls are shifted or when they present different corrugation amplitudes. Such assessment is nonetheless crucial before considering further complexity in the modeling of fracture flow processes (particle transport, heat and mass transfer, etc...). Finally, a fine analysis of the mechanisms involved at the local scale is required to better understand the influence of the fracture geometry on the flow field and how inertial effects may affect the validity of the LCL.

To estimate the validity of the LCL and the CL for modeling flow in rough fractures, we present here a thorough numerical investigation aiming at characterizing flow in rough fractures by studying the effect of their geometry on their hydraulic aperture. For convenience, fractures are modeled as channels with sinusoidal walls.

In this chapter, we do not study a specific fracture geometry. Instead, we consider all the possible configurations involving sinusoidal walls to investigate the influence of the fracture mean aperture, walls corrugation wavelength and amplitude, asymmetry between walls corrugations, and horizontal phase shift between the walls on the flow characteristics. Instead of developing analytical solutions for the flow, we verify the validity of the LCL to model flow by comparing its predictions to numerical solutions of the NS equations for different values of Re.

Chapter outline: In section 1, we present the fracture configuration as well as the different parameters that define its geometry. In section 2, the equations governing the flow in corrugated fractures are recalled and the LCL model is developed in the dimensionless form. In section 3, these equations are expoited to evaluate the effect of the fracture geometry on the difference between the hydraulic aperture predicted by the LCL and the mean or mechanical aperture used in the CL . In section 4, the numerical method used to solve the NS equations is described. The validity of the LCL is then assessed for Re ranging from

6.7×10^{-2} to 6.7×10^{1}. In particular, these predictions given by the LCL are compared to the numerical results, and the relative error between the two solutions systematically quantified for different geometrical configurations. In section 5, a discussion is provided based on the results of the study.

2.1 Geometrical description of fractures with corrugated walls

The domain is represented in a reference frame (X, Z) where X corresponds to the horizontal direction (the main flow direction) and Z to the vertical one. Gravity is taken into account and applies perpendicularly to the main flow direction (along Z).

Following the approach proposed by Nizkaya [27], we consider a two dimensional fracture having two rough walls with idealized periodic roughness described respectively by the functions $\Phi_1(X)$ for the lower wall and $\Phi_2(X)$ for the upper one (Figure (2.1)). The fracture total length is L_∞ and is thus defined by the domain limited by $X\epsilon[0, L_\infty]$ and $Z\epsilon[\Phi_1(X), \Phi_2(X)]$. The fracture walls corrugations are smooth so that $\frac{\partial \Phi_{1,2}(X)}{\partial X} << 1$. The fracture can be

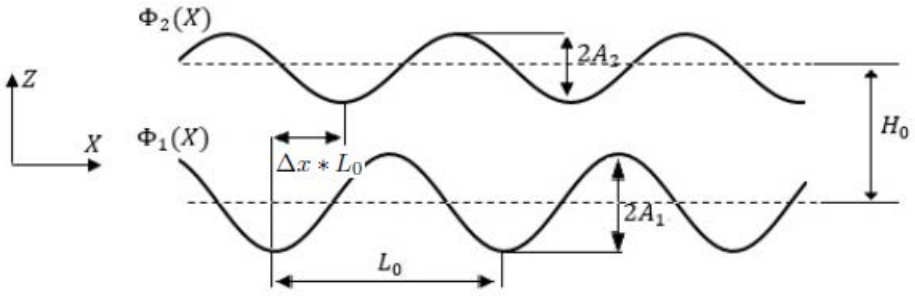

Figure 2.1: Schematic diagram of a 2D fracture having sinusoidal walls.

equally defined by the local half aperture $H(X) = \frac{1}{2}(\Phi_2(X) - \Phi_1(X))$ and the fracture middle line $\Phi(X) = \frac{1}{2}(\Phi_1(X) + \Phi_2(X))$. The fracture walls are periodic and have the same corrugation wavelength L_0, which is the characteristic length of the flow in the X direction.

The phase shift between the two walls is ΔX and the corrugation amplitude of each wall is:

$$A_{1,2} = \frac{1}{2}(max[\Phi_{1,2}(X)] - min[\Phi_{1,2}(X)])$$

The characteristic length in the Z direction can be defined as the mean aperture of the fracture given by:

$$H_0 = \frac{1}{L_\infty}\int_0^{L_\infty}(\Phi_2(X) - \Phi_1(X))dX$$

Finally, the fracture aspect-ratio can be defined as:

$$\epsilon = \frac{H_0}{L_0}$$

At this point, it is important to note that there are two types of channels that can be found in literature depending on the order of magnitude of ϵ. Channels with $\epsilon \sim 1$ are commonly used to model flow and heat transfer in heat exchangers tubes (e.g. Yin et al. [105], Mohammed et al. [106]) and channels with $\epsilon << 1$ are commonly considered to represent rough fractures.

It is more convenient to study the fracture flow using dimensionless parameters. The length scales L_0 and H_0 are thus used to define the dimensionless variables:

$$z = \frac{Z}{H_0},\ \phi_{1,2}(x) = \frac{\Phi_{1,2}(X)}{H_0},\ \phi(x) = \frac{\Phi(X)}{H_0},\ v_x = \frac{V_X}{V_0},\ v_z = \frac{1}{\epsilon}\frac{V_Z}{V_0},\ \psi = \frac{\Psi}{Q}$$

In addition, the following dimensionless parameters are introduced:

- $\delta_0 = \dfrac{A_1 + A_2}{2H_0}$ is the dimensionless average corrugation defined by the ratio of the mean corrugation amplitude of the walls to the fracture mean aperture. This parameter is an indicator of the roughness of the walls.
- $\gamma = \dfrac{A_2 - A_1}{A_2 + A_1}$ represents the asymmetry between the walls corrugations defining the difference of corrugation level between the two walls. $\gamma > 0$ means that the upper wall is more corrugated than the lower one and vice versa. $\gamma = 0$ corresponds to upper and bottom walls with the same corrugation amplitude and $\gamma = 1$ to a fracture with flat

bottom wall.

- $\Delta x = \dfrac{\Delta X}{L_0}$ is the dimensionless phase shift

The fracture geometry is thus defined by four parameters ϵ, δ_0, γ and Δx.

In this thesis, the periodic corrugations of the walls are represented by a sinusoidal variation (cf. chapter 1). For a fracture with sinusoidal walls, the walls can be defined by the following equations:

$$\phi_1(x) = -\frac{1}{2} + \delta_0(1-\gamma)sin[2\pi(x - \frac{\Delta x}{2})] \text{ and } \phi_2(x) = \frac{1}{2} + \delta_0(1+\gamma)sin[2\pi(x + \frac{\Delta x}{2})] \quad (2.1)$$

The equation of the dimensionless local half-aperture of the fracture is given by:

$$h(x) = \frac{1}{2} + \delta_0(cos(2\pi x)sin(\pi\Delta x) + \gamma(sin(2\pi x)cos(\pi\Delta x))) \quad (2.2)$$

and the equation of the fracture middle-line is:

$$\phi(x) = \delta_0(sin(2\pi x)cos(\pi\Delta x) + \gamma(cos(2\pi x)sin(\pi\Delta x))) \quad (2.3)$$

In such a case, the effect of δ_0, γ and Δx on the fracture geometry is illustrated in Table 2.1.

Table 2.1: Geometry of the fracture walls corresponding to different values of δ_0 (a), Δx (b) and γ (c).

		$\delta_0 = 0.2$	$\delta_0 = 0.3$
(a)	$\Delta x = 0\ , \gamma = 0$		
		$\Delta x = 0.25$	$\Delta x = 0.5$
(b)	$\delta_0 = 0.2\ , \gamma = 0$		
		$\gamma = 0.2$	$\gamma = 0.8$
(c)	$\delta_0 = 0.2\ , \Delta x = 0.5$		

2.2 Governing equations

Steady flows in closed channels are governed by the NS equations:

$$\rho(V.\nabla)V = -\nabla P + \rho g + \mu\nabla^2 V \tag{2.4}$$

where V is the velocity of the fluid, ρ is the fluid density, μ is the fluid dynamic viscosity, and P is the hydrodynamic pressure. This equation is an application of the fundamental principle of dynamics to a fluid particle. The rate change of the linear momentum of the fluid particle (left-hand side of equation (2.4)) is equal to the sum of the external forces:

- $\rho(V.\nabla)V$: describes the inertial acceleration. As steady flow is independent of time, acceleration is only due to spatial variations of the velocity field by convection. This term is a source of non-linearity in the flow as it presents the square of the velocity vector.
- $-\nabla P$: represents the pressure gradient.
- ρg: represents the external body forces. In our case, these forces are solely due to gravity.
- $\mu\nabla^2 V$: accounts for the energy dissipation due to viscous friction occurring inside the fluid causing momentum diffusion. Its contribution is more important in zones of high shear, near walls for example.

Equation (2.4), when written in the scalar form, consists in a system of three equations with four variables, the three velocity vector components and the pressure. The system of equations is closed using the continuity equation (mass conservation) which, in the case of an incompressible fluid flow, is written as:

$$\nabla.V = 0 \tag{2.5}$$

The relative importance between viscous and inertial forces is the ratio between the orders of magnitude of the inertial acceleration ($\rho(V.\nabla)V$) and of the viscous friction ($\mu\nabla^2 V$), which

is the Reynolds number $Re = \frac{\rho V_0 H_0}{\mu}$. When $Re >> 1$, viscous friction becomes negligible (perfect fluid case). On the other hand, when $Re << 1$, viscosity dominates the flow, and equation (2.4) can be simplified into the Stokes equation:

$$\mu \nabla^2 V - \nabla P + \rho g = 0 \tag{2.6}$$

2.2.1 Flow between parallel flat walls: the cubic law

In an incompressible laminar flow generated by a pressure gradient along a channel consisting of two parallel planes (the parallel-plate model), the inertial terms are identically null and the steady flow can be expressed via equation (2.6). This problem has been thoroughly addressed in the literature. For instance, Zimmerman and Bodvarsson [69] recalled in detail all the equations and conditions Of the problem. We therefore recall here only the major conclusions.

If the wall length is much greater than the distance separating them, one can assume that only the X-component of the velocity vector is non-zero. In such case, the X-component of equation (2.6) is written as:

$$(\nabla P)_X = \frac{\partial P}{\partial X} = \mu \frac{\partial^2 V_X}{\partial X^2} \tag{2.7}$$

with ∇P the applied pressure gradient. If the distance between the two walls is H_0, integrating equation (2.7) with the no-slip boundary conditions ($V_x(0) = V_x(H_0) = 0$) leads to the following parabolic velocity profile, similar to the one found in the so called Poiseuille flow:

$$V_x = -\frac{H_0^2}{8\mu} (\nabla P)_X \, (1 - \frac{4Z^2}{H_0^2}) \tag{2.8}$$

For a difference Δh in the hydraulic head h between the ends of the two plates, $(\nabla P)_X = \frac{\rho g \Delta h}{L_0}$. The volumetric flow rate per unit width can thus be expressed as ([54]):

$$Q = \int_{-H_0/2}^{H0/2} V_X dZ = -\frac{\rho g {H_0}^3}{12\mu} \Delta h / L_0 \tag{2.9}$$

2.2.2 Flow between corrugated walls: the local cubic law

We consider here the fractures defined in section 1. The viscous flow in the fracture is calculated under the assumption that the simplification of equation (2.4) into equation (2.6) is valid. The no-slip boundary conditions on the fracture walls yield:

$$\vec{V}(X, \Phi_1(X)) = \vec{0} \quad \vec{V}(X, \Phi_2(X)) = \vec{0} \tag{2.10}$$

and the volumetric flow rate per unit width is given by:

$$Q = \int_{\Phi_1(X)}^{\Phi_2(X)} V_X(X, Z) dZ \tag{2.11}$$

Writing equation (2.6) in scalar form and estimating $\frac{\partial^2 V_X}{\partial X^2}$ proportional to $\frac{V_0}{L_0^2}$ and $\frac{\partial^2 V_X}{\partial Z^2}$ proportional to $\frac{V_0}{H_0^2}$, one can see that when $\epsilon << 1$, the derivative of the velocity with respect to X can be neglected compared to that with respect to Z. Thus, the projection of equation (2.6) on X can be reduced to:

$$\mu \frac{\partial^2 V_X}{\partial Z^2} = \frac{\partial P}{\partial X} \tag{2.12}$$

Integrating equation (2.12) with respect to Z, and taking into account the boundary conditions (equation (2.10)), leads to:

$$V_X(X, Z) = \frac{1}{2\mu} \frac{\partial P}{\partial X} (Z - \Phi_1(X))(Z - \Phi_2(X)) \tag{2.13}$$

Defining $H(X) = \frac{1}{2}(\Phi_2(X) - \Phi_1(X))$ as the local half aperture, the average velocity can then be calculated as:

$$\overline{V_X} = \frac{1}{2H(X)} \int_{\Phi_1(X)}^{\Phi_2(X)} V_X(X, Z) dZ = \frac{-H^2(X)}{3\mu} \frac{\partial P}{\partial X} \tag{2.14}$$

Recalling the no-slip boundary conditions $V_X(X, \Phi_1(X)) = V_X(X, \Phi_2(X)) = 0$, equation (2.5), which is applied to local velocities V_X, can be also applied to the flux $2H(X)\overline{V_X}$

(Zimmerman and Bodvarsson [69]), thus leading to:

$$\nabla.[H^3(X)\nabla P] = \frac{d}{dX}[H^3(X)\frac{dP}{dX}] = 0 \tag{2.15}$$

which corresponds to the Reynolds equation for a steady incompressible flow ([57]). Reynolds equation gives an approximate description of the flow between two slightly non parallel and non-planar surfaces. Equation (2.15) implies that the CL, which is valid for flows occurring between two parallel planar walls, can be applied locally (at a point of coordinate X) to a channel with non parallel walls, leading to the LCL model. To proceed from the local level to the fracture level, equation (2.15) can be integrated between two points X_1 and X_2 along the channel ([58]):

$$\overline{\Delta P} = -12\mu Q \int_{X_1}^{X_2} \frac{1}{H^3(X)} dX \tag{2.16}$$

with $\overline{\Delta P}$ the pressure drop between these points. When the walls of the fracture are periodic with a wavelength L_0, equation (2.16) gives ([57], [81]):

$$\frac{\overline{\Delta P}}{L_0} = -\frac{12\mu Q}{{H_h}^3} \tag{2.17}$$

where H_h represents the hydraulic aperture of the fracture.

To write the LCL in dimensionless form, $x = \frac{X}{L_0}$ and $h(x) = \frac{H(X)}{H_0}$ are defined. The hydraulic aperture of the fracture is thus:

$$H_h = 2H_0 < h^{-3} >^{-\frac{1}{3}} \tag{2.18}$$

with:

$$< h^{-3} > = \int_0^1 \frac{1}{h^3(x)} dx \tag{2.19}$$

the dimensionless hydraulic aperture.

Taking the viscous lubrication pressure $P^* = \frac{\mu V_0}{\epsilon H_0}$ as a pressure scale, equation (2.17)

leads to:

$$p = -\frac{3}{2} < h^{-3} > \tag{2.20}$$

with $p = \Delta P / P^*$ the dimensionless pressure drop.

2.2.3 Flow velocity components in corrugated channels

To calculate the flow velocity components, equation (2.6) is rewritten as a function of the stream function $\Psi(X, Z)$ ([70], [71], [27]), which satisfies $V_X = \frac{\partial \Psi}{\partial Z}$ and $V_Z = -\frac{\partial \Psi}{\partial X}$:

$$\nabla^4 \Psi = \frac{\partial^4 \Psi}{\partial X^4} + 2\frac{\partial^4 \Psi}{\partial X^2 \partial Z^2} + \frac{\partial^4 \Psi}{\partial Z^4} = 0 \tag{2.21}$$

Choosing the walls corrugation wavelength L_0 and the channel mean aperture H_0 as length scales and the mean flow velocity V_0 as a velocity scale in the X direction, the following dimensionless parameters can be defined:

$$z = \frac{Z}{H_0},\ \phi_{1,2}(x) = \frac{\Phi_{1,2}(X)}{H_0},\ \phi(x) = \frac{\Phi(X)}{H_0},\ v_x = \frac{V_X}{V_0},\ v_z = \frac{1}{\epsilon}\frac{V_Z}{V_0},\ \psi = \frac{\Psi}{Q} \tag{2.22}$$

with $v_x = \frac{\partial \psi}{\partial z}$ and $v_z = -\frac{\partial \psi}{\partial x}$ the velocity components in the dimensionless form. Equation (2.21) can then be rewritten as:

$$\epsilon^4 \frac{\partial^4 \psi}{\partial x^4} + 2\epsilon^2 \frac{\partial^4 \psi}{\partial x^2 \partial z^2} + \frac{\partial^4 \psi}{\partial z^4} = 0 \tag{2.23}$$

When $\epsilon << 1$, the terms proportional to ϵ^2 and ϵ^4 can be neglected (zeroth-order when the stream function is developed in the form of an asymptotic expansion), and equation (2.23) reduces to:

$$\frac{\partial^4 \psi}{\partial z^4} = 0 \tag{2.24}$$

In order to simplify the problem, a cross-channel coordinate is introduced as ([69], [16]):

$$\eta = \frac{z - \phi(x)}{h(x)}$$

η enables to map the channel interior into a rectangle ($z \in [\phi_1(x), \phi_2(x)] \rightarrow \eta \in [-1, 1]$). Equation (2.24) becomes:

$$\frac{1}{h^4(x)} \frac{\partial^4 \psi}{\partial z^4} = 0 \tag{2.25}$$

with the boundary conditions (equation 2.10) expressed as:

$$\psi(x, -1) = -\frac{1}{2}, \quad \psi(x, 1) = \frac{1}{2}, \quad \frac{\partial \psi}{\partial \eta}(x, -1) = \frac{\partial \psi}{\partial \eta}(x, 1) = 0 \tag{2.26}$$

The solution of equation (2.25) is thus:

$$\psi(x, \eta) = \frac{1}{4}\eta(3 - \eta^2) \tag{2.27}$$

and the flow velocity components are respectively equal to ([69], [16]):

$$v_x = \frac{3}{4h(x)}(1 - \eta^2) \text{ and } v_z = \frac{3(\phi'(x) + \eta h'(x))}{4h(x)}(1 - \eta^2) \tag{2.28}$$

The validity of these expressions to describe the flow velocity components in corrugated channels will be assessed later on. Note that replacing the dimensional form of equation (2.28) in Equation 2.12 also leads to the LCL in the form given by equation (2.16).

2.3 Influence of the fracture geometry on its hydraulic aperture

The CL, established with respect to the mean aperture, tends to overestimate the flow rate in channels with corrugated walls ([60], [49]) and thus needs to be replaced by the LCL for a better description of the flow. To evaluate this overestimation, we examine the effect

of the fracture geometry on the difference between the hydraulic aperture H_h (on which the LCL is based) and the mean aperture H_0 (on which the CL is based).

In a channel with corrugated walls, the ratio $\frac{H_h}{H_0}$ calculated from the dimensionless hydraulic aperture $< h^{-3} >$ (equation (2.18)) depends only on the corrugation amplitude representing walls roughness defined by δ_0, the corrugations asymmetry defined by γ, and the dimensionless phase shift between the two walls Δx (equations (2.19) and (2.2)). As $\frac{H_h}{H_0}$ does not depend on the channel aspect ratio ϵ, if the channel mean aperture H_0 is fixed, then two channels having walls with different wavelengths should have the same hydraulic aperture H_h.

2.3.1 Δx effect

The variation of $\frac{H_h}{H_0}$ as a function of Δx is evaluated for $\Delta x \in [0, 1]$ (Figure (2.2)). This range covers all the possible phase shifts between the top and bottom walls. $\Delta x = 0$ and $\Delta x = 1$ correspond to in phase walls whereas $\Delta x = 0.5$ corresponds to the case where the phase shift is maximum between the two walls. Different values of δ_0 (0.1, 0.2 and 0.4) and γ (0, 0.5 and 1) are considered to investigate multiple geometrical configurations. $\gamma = 0$ corresponds to a channel having two walls with the same corrugation amplitude and $\gamma = 1$ to a channel with one flat wall.

$\frac{H_h}{H_0}$ is very close to 1 for $\delta_0 = 0.1$ in all the considered configurations. This means that H_h does not deviate strongly from H_0 in the case of low corrugation amplitudes. On the other hand, for $\delta_0 = 0.2$ and $\delta_0 = 0.4$, $\frac{H_h}{H_0}$ decreases with the increase of the phase shift between the two walls and reaches its minimum when this shift is maximum ($\Delta x = 0.5$). Note that when $\gamma = 0$ and $\Delta x = 0$, corresponding to parallel identical walls, H_h is equal to H_0 for all the values of δ_0. Therefore, the deviation of H_h from H_0 increases for higher wall corrugations amplitudes and when the walls are shifted. For $\gamma = 1$, $\frac{H_h}{H_0}$ does not vary as a function of Δx as there is, by definition, no phase shift for this specific configuration. However, when $\gamma = 1$, $\frac{H_h}{H_0}$ decreases significantly when δ_0 increases.

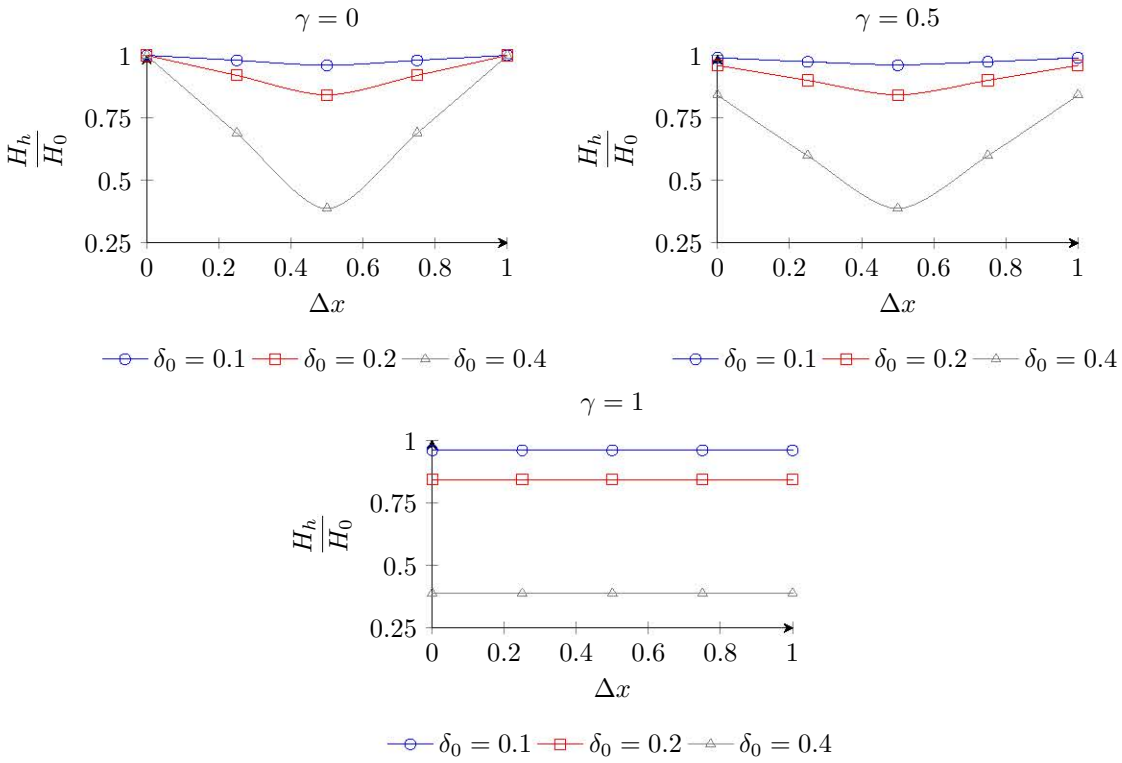

Figure 2.2: Variation of $\frac{H_h}{H_0}$ as a function of the phase shift Δx for different values of the dimensionless corrugation amplitude δ_0, and for corrugations asymmetry γ equal to 0, 0.5 and 1 respectively

2.3.2 γ effect

The variation of $\frac{H_h}{H_0}$ as a function of γ is plotted in Figure (2.3). γ varies in the range of $[-1, 1]$ to cover different corrugation asymmetries, going from a channel with a flat bottom wall ($\gamma = -1$) to a channel with a flat top one ($\gamma = 1$). Different values of δ_0 (0.1, 0.2 and 0.4) and Δx (0, 0.2 and 0.5) are considered to cover different ranges of the corrugation amplitudes and phase shifts between the walls. For a channel with parallel identical walls ($\gamma = 0$ and $\Delta x = 0$), the hydraulic aperture is always equal to the mean aperture.

$\frac{H_h}{H_0}$ is minimal when one of the channel walls is flat ($\gamma = \pm 1$). For the same mean corrugation amplitude, $\frac{H_h}{H_0}$ increases when the asymmetry between the two walls corrugations decreases. When the phase shift between the two walls is maximal, the hydraulic aperture remains constant with the variation of the asymmetry between the two walls. This means that for the same average corrugation amplitude, a channel having a maximum phase shift

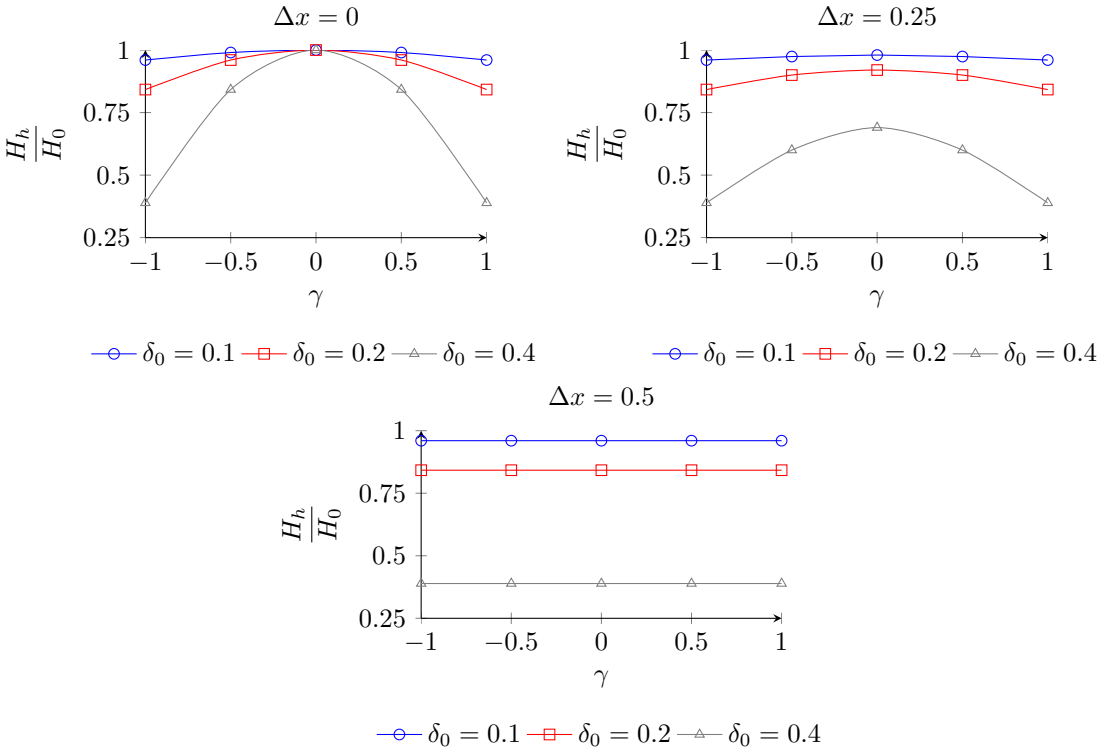

Figure 2.3: Variation of $\frac{H_h}{H_0}$ as a function of the corrugations asymmetry γ for different values of the dimensionless corrugation amplitude δ_0, and for phase shifts Δx equal to 0, 0.25 and 0.5 respectively.

between its walls has the same hydraulic aperture as a channel having a flat wall and a corrugated wall.

2.4 Influence of the fracture geometry on the validity of the LCL for different Reynolds numbers

In this section, numerical simulations using the finite element method (FEM) are conducted to study the effect of different geometrical properties of fractures with sinusoidal walls on the validity of the LCL, for Re values ranging from 6.7×10^{-2} to 6.7×10^{1}. To do so, we systemically compare the theoretical predictions of the LCL to the numerical solution obtained by solving the full NS equations.

2.4.1 Numerical Method

The FEM is used to compute numerical solutions of the NS equations. The numerical solutions are obtained using COMSOL Multiphysics software. Like most of the numerical methods, the FEM is based on the discretization of the geometrical domain into small and simple cells such as triangles or quadrilaterals in 2D. Each one of these cells is called an element. Each element contains nodes, which are points in the domain on which approximated solutions are computed. These approximated solutions are represented by basis functions that are usually selected as polynomials of order 1 to 3. For each element, the solver searches values at the nodes and the polynomials constants that can match the differential equation in the most accurate way.

Numerical simulation procedure

The aim of the simulations is to verify the validity of the LCL represented in the dimensionless form by equation (2.20). To do so, the pressure difference between two sections perpendicular to the main flow and distant of a wavelength, computed numerically via the resolution of the NS equation, is compared to the pressure difference estimated by the LCL. The procedure of the numerical simulations is as follows:

- The geometry of the fracture is first defined. The fracture is built by setting the amplitude and the wavelength of its walls, and the horizontal phase shift between them according to the expressions of $\Phi_1(X)$ and $\Phi_2(X)$. A flat part is constructed upstream to ensure a parabolic velocity profile at the fracture inlet.

- The computational domain is discretized using a mesh consisting of triangular elements. The mesh is refined in the near wall regions and gradually coarsened when moving towards the fracture center (Figure (2.4)). A mesh objectivity test was performed and the spatial discretization considered sufficiently fine when the same problem, treated with a finer mesh (1.5 times more nodes) led to the same solution for each considered field (velocity and pressure).

- A parabolic velocity profile with a mean flow velocity V_0 is defined at the inlet. V_0 is defined according to the value of the corresponding Re. A zero pressure is imposed at

the outlet $P_{outlet} = 0$, and the no-slip boundary conditions are imposed on the fracture walls ($\vec{V_f} = \vec{0}$).

- The continuity and NS equations governing the steady incompressible flow in the fracture are solved, and the pressure and velocity fields are computed.

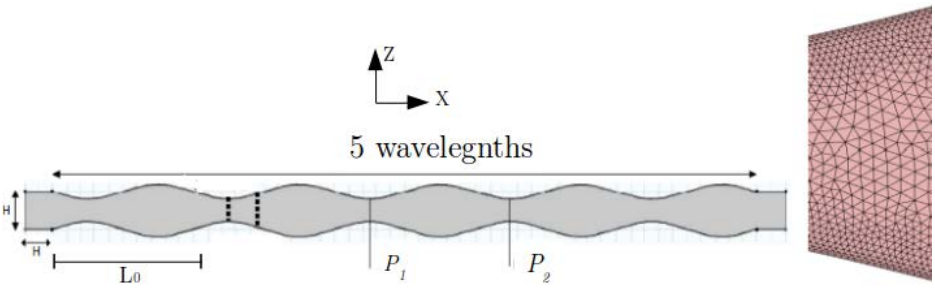

Figure 2.4: Example of a fracture with sinusoidal walls used in the simulations where the pressure difference $P_1 - P_2$ is calculated along the third wavelength (left), where the flow is developed and far from the inlet and outlet boundaries. The mesh (adaptive) used for the numerical simulations (right). The two dashed lines represent the two cut lines on which the velocity profile is plotted

The pressure difference $\Delta P = P_1 - P_2$ is calculated along the third wavelength (Figure (2.4)) where the flow is developed, far away from the inlet and outlet boundaries. This difference is divided by the corresponding lubrication pressure P_0 to determine the dimensionless pressure drop p which is then compared to the solution determined by the LCL (equation (2.20)).

2.4.2 Low Re (< 1)

The LCL is generally considered valid for $Re < 1$. In this section we set $Re = 0.1$ for all the simulations.

2.4.2.a. Relative error between the LCL and NS solutions for three reference geometries

To study the effect of each one of the geometrical parameters on the validity of the LCL, we consider three reference geometries (Table (2.2)).

Table 2.2: Geometrical properties of the three fractures used as references in the numerical simulations.

Configuration	*Geometry*	ϵ	δ_0	Δx	γ
Parallel walls		0.1	0.2	0	0
Mirror symmetric walls		0.1	0.2	0.5	0
Arbitrary walls		0.1	0.2	0.25	0.2

For each geometry, we set different values of the parameter whose effect is being studied, and the dimensionless pressure p is computed according to the LCL (p_{LCL}) and to the NS numerical solution (p_{NS}) respectively. The relative error between the two values is then calculated as $error = \dfrac{p_{NS} - p_{LCL}}{p_{LCL}} * 100$. Finally, the variation of this error is plotted as a function of the established parameter.

2.4.2.b. Influence of ϵ, δ_0, γ and Δx on the relative error between the LCL and NS solutions

The LCL was established for $\epsilon << 1$. To verify to which extent the value of ϵ should be small for the LCL to be valid, ϵ was varied from 0.05 to 0.4 for each geometry. The variation of the relative error between the LCL and NS solutions as a function of ϵ is plotted in Figure (2.5).

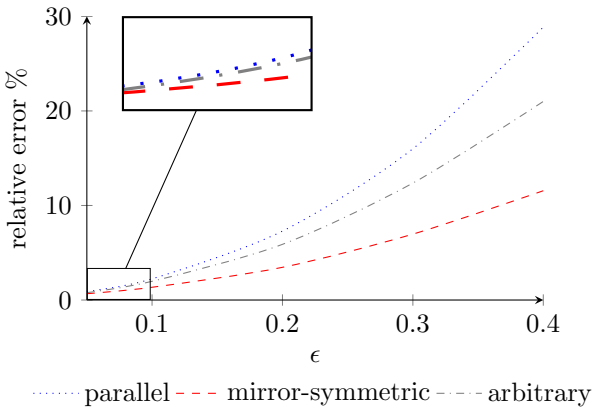

Figure 2.5: Variation of the relative error between the LCL and NS solutions as a function of the aspect ratio ϵ for channels with parallel walls, with mirror symmetric walls and with arbitrary walls (Table (2.2)).

One can notice that the relative error increases with the increase of ϵ for all the geometrical configurations. This error is less than 2 % for $\epsilon < 0.1$ in all the geometrical configurations. When ϵ increases, the error is maximum in the channel with parallel walls. Moreover, this error and consequently the deviation of the LCL from NS are maximal in a channel with parallel walls and minimal in a channel with mirror-symmetrical configuration.

To compare the two solutions on a local level, the dimensionless velocity profiles are plotted on two cut lines inside the channel located at $x = 1.25$ and $x = 1.5$ (Figure 2.4) for $\epsilon = 0.1$ and $\epsilon = 0.4$, in the cases of channels with parallel and mirror symmetric walls (Figures (2.6) and (2.7)). For $\epsilon = 0.1$, the velocity profiles seem to be identical in the case of parallel

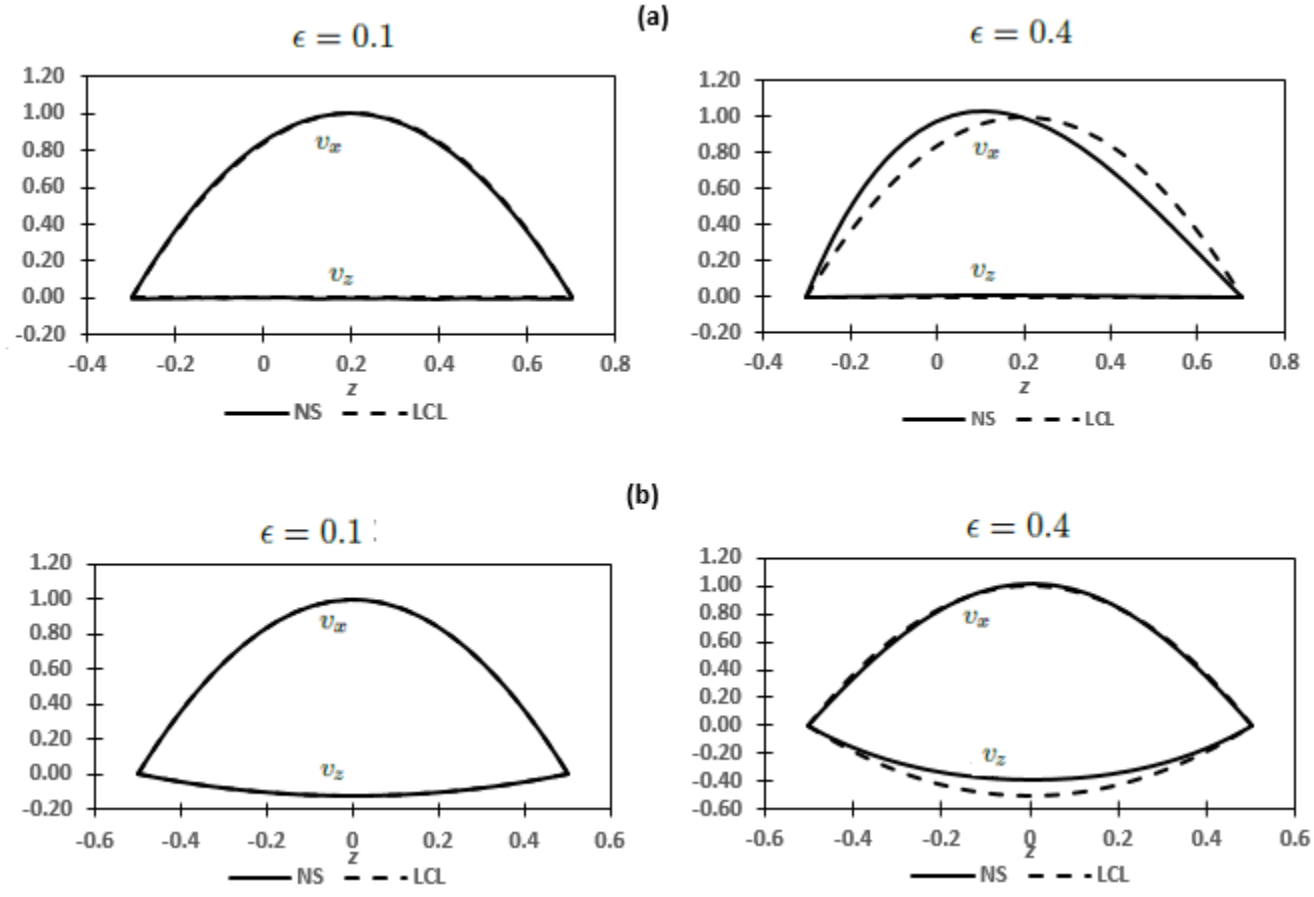

Figure 2.6: Dimensionless velocity profiles given by the LCL (dashed lines) and NS (solid lines) solutions for aspect ratios $\epsilon = 0.1$ and $\epsilon = 0.4$ in the case of a channel with parallel walls. (a) velocity profiles on cut line 1. (b) velocity profiles on cut line 2

walls and mirror symmetric walls. On the other hand, the two profiles deviate for $\epsilon = 0.4$ and the deviation is more important in the channel with parallel walls. This confirms the

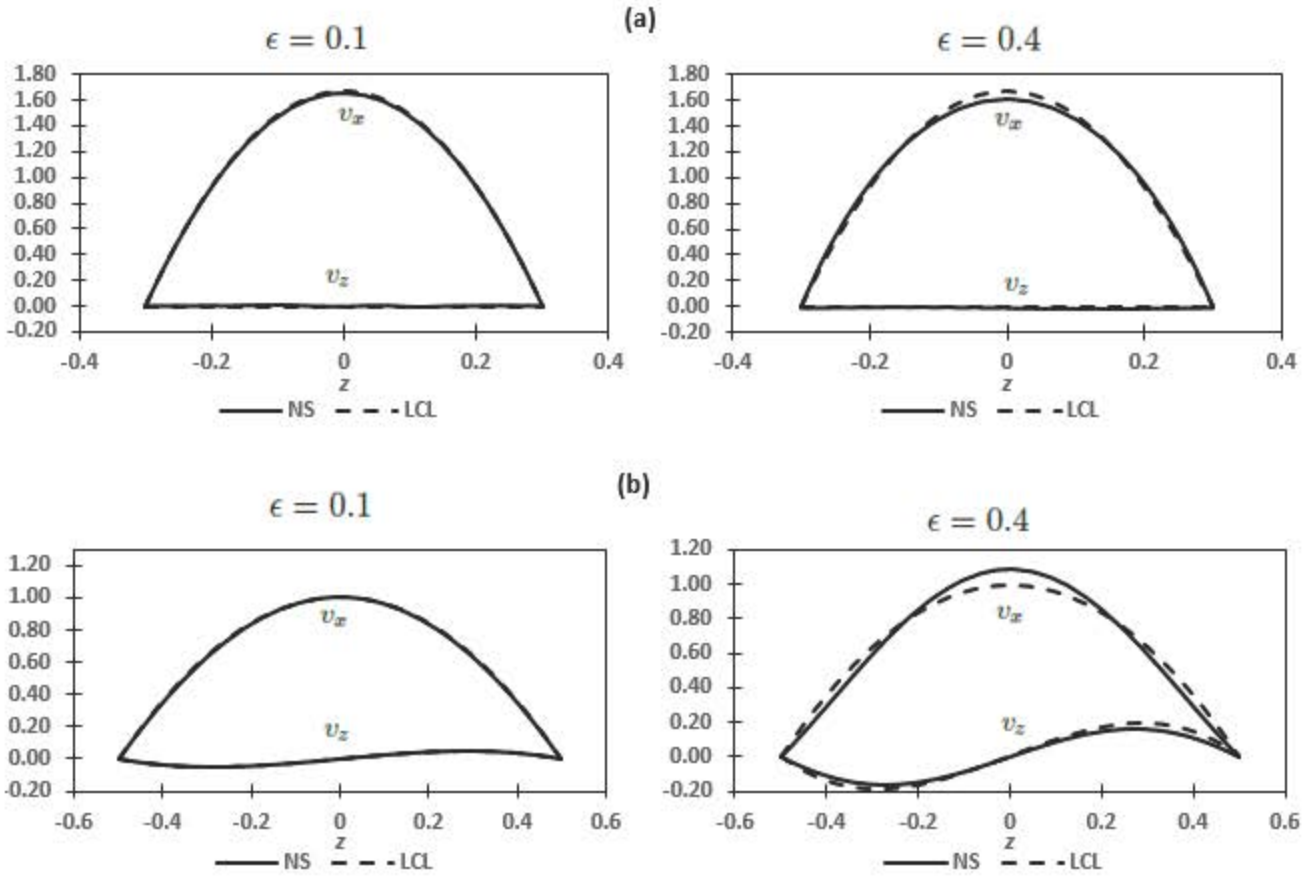

Figure 2.7: Dimensionless velocity profiles given by the LCL (dashed lines) and NS (solid lines) solutions for aspect ratios $\epsilon = 0.1$ and $\epsilon = 0.4$ in the case of a channel with mirror symmetric walls. (a) velocity profiles on cut line 1. (b) velocity profiles on cut line 2

fact that the deviation between the LCL and NS is greater in the channel with parallel walls.

The variation of the relative error between the LCL and NS solutions as a function of δ_0 is plotted in Figure (2.8) for all channel configurations. δ_0 was varied in the range [0, 0.4] because $\delta_0 = 0.5$ in the mirror symmetrical channel would lead the two walls to be in contact one with each other.

The relative error between the LCL and NS solutions does not increase significantly in the mirror symmetrical configuration for all possible values of δ_0 and remains around 1 %. We conclude that the variation of δ_0 has a small effect on the deviation of the LCL in this configuration. Nonetheless, the relative error increases with the increase of δ_0 in the channel with arbitrary walls, and in a greater extent in the channel with parallel walls. The deviation

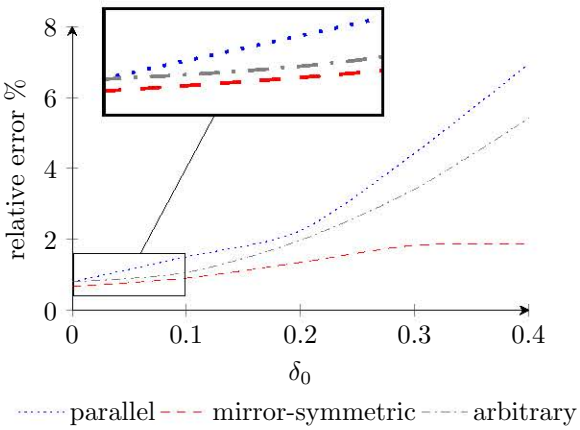

Figure 2.8: Variation of the relative error between the LCL and NS solutions as a function of the dimensionless corrugation amplitude δ_0 for for channels with parallel walls, with mirror symmetric walls and with arbitrary walls (Table (2.2)).

of the LCL with the respect to the NS solutions due to the increase of δ_0 is then maximum in a channel with parallel walls and minimum in a channel with mirror symmetrical walls.

The variation of the relative error between the LCL and NS solutions as a function of γ is plotted in Figure (2.9). γ was varied from 0 (a channel having two identical walls) to 1 (a channel having a flat wall, representing the maximal possible asymmetry between the two walls).

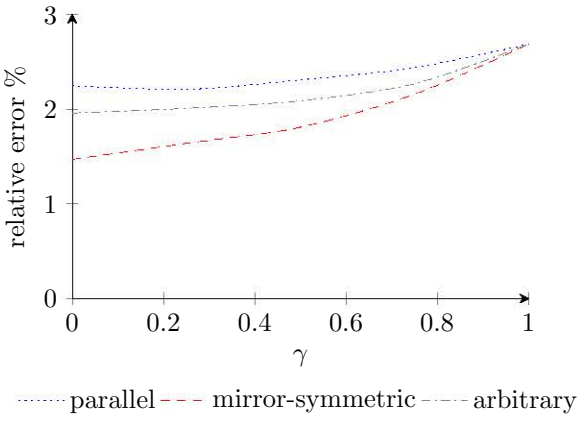

Figure 2.9: Variation of the relative error between the LCL and NS solutions as a function of the corrugations asymmetry γ for channels with parallel walls, with mirror symmetric walls and with arbitrary walls (Table (2.2)).

For the three channels, the relative error between the two solutions remains between 1.5 % and 2.5 % when γ increases. Thus, increasing γ has a negligible effect on the deviation of

the LCL solution with respect to that of NS equations.

The dimensionless phase shift Δx was varied between 0 and 1 to take into account all the possible phase shifts between the two walls. The variation of the relative error between the LCL and NS solutions as a function of Δx are plotted in Figure (2.10).

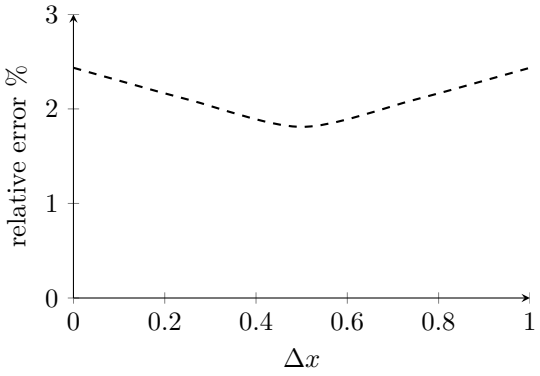

Figure 2.10: Variation of the relative error between the LCL and NS solutions as a function of the phase shift Δx.

The variation of the pressure as a function of Δx presents a symmetry around $\Delta x = 0.5$. This is due, as shown in section 3, to the fact that the hydraulic aperture is independent of the direction of the phase shift between the two walls. The flow in a channel where the bottom wall is offset from the top wall is thus identical to that in a channel where the top wall is offset from the bottom one, if the offset is equal. One can notice that the relative error is minimum for $\Delta x = 0.5$ and maximum for $\Delta x = 0$.

2.4.3 High Re (> 1)

When Re increases, the relation between the pressure gradient along the fracture and the flow rate does not remain linear (as in equation (2.16)) due to the effect of fluid inertia that becomes more important. For the same applied pressure gradient, the flow rate decreases, or vice versa, maintaining a given flow rate through the fracture requires increasing the applied pressure gradient.

On the other hand, we recall that the LCL was established under the assumption of a Stokes flow inside the fracture and therefore for $Re << 1$. In its dimensional form (equa-

tion(2.20)), the pressure is independent of Re although it is expected to increase as Re increases. The validity of the LCL for high Re must then be assessed. Moreover, the velocity profiles are no more ideally parabolic., and depending on the channel geometry, recirculation zones may appear inside the fracture. They are due to the viscous shear stresses resulting from the fluid momentum mismatch in the fracture center and the near-wall regions. The fluid particles located in the central part of the fracture move faster than the quasi-stagnant ones located in the channel hollows. This results in the formation of fluid recirculations near the rough walls. These recirculation zones can also appear under Stokes flow conditions (Kitanidis and Dykaar [77], Malevich et al. [78]) but under stronger geometrical constraints. Such recirculation zones greatly affect the validity of the LCL. Investigating the onset of creation of these zones as well as the effect of the fracture geometry on their appearance are out of the scope of this study. Instead, we focus on studying the range of Re to which the LCL can still be used to model flow in fractures, and the effect of the fracture geometry on this validity.

To do so, we use the reference fractures defined in the previous section (Table 2.2), and calculate the dimensionless pressure gradient p to compare the LCL and NS solutions for Re varying in the range $[6.7 \times 10^{-2}, 6.7 \times 10^{1}]$. We then compare the relative error between the two solutions for several geometrical configurations corresponding to different values of ϵ, δ_0, γ and ΔX.

2.4.3.a. Relative error between the LCL and NS solutions for the reference geometries

First, we study the variation of the dimensionless pressure p as a function of Re according to the LCL and to NS solutions for each reference geometry (Table 2.2). The variation of the relative error between the two solutions is plotted in Figure (2.11). For high Re (i.e. $Re > 40$), the deviation between the LCL and NS solutions is maximal in the mirror-symmetrical configuration and minimal in the channel with parallel walls. This result is different than the one found for low Re (section 4.2.1). It can also be noted that the relative error remains constant for $Re < 15$ in all the geometrical configurations. It then increases progressively, although remaining relatively low, i.e. below 2 %, for Re values less than 30.

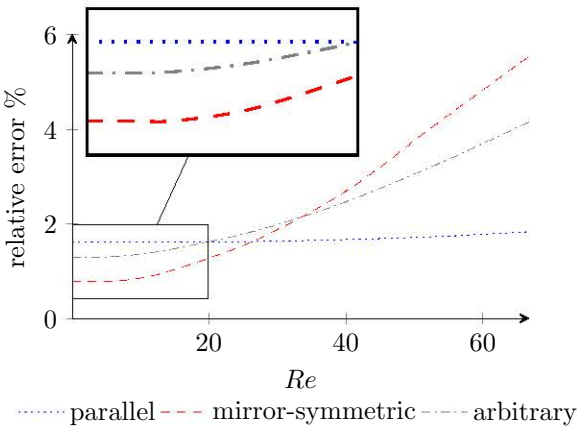

Figure 2.11: Variation of the relative error between the LCL and NS solutions as a function of Re for the reference geometries (Table 2.2).

To further investigate this effect, the dimensionless velocity profiles are compared for $Re = 6.6 \times 10^{-2}$ and $Re = 6.6 \times 10^{1}$, in the cases of fractures with parallel and mirror symmetric walls (Figures (2.12) and (2.13)). One can see that the velocity profile calculated by the LCL coincides exactly with the profile predicted by NS solution when $Re = 6.6 \times 10^{-2}$, for the two cases. For $Re = 6.6 \times 10^{1}$, the two profiles also coincide for the fracture with parallel walls but a deviation appears for the fracture with mirror symmetric walls, which confirms that the error is more important in the latter case (Figure 2.11).

In order to study the effect of the fracture geometry on the validity of the LCL for higher values of Re, we computed the variation of the relative error between the two solutions as a function of Re for each geometry, changing a parameter each time.

2.4.3.b. Influence of ϵ, δ_0, γ and Δx on the relative error between the LCL and NS solutions

In the reference geometries (Table 2.2), ϵ was fixed equal to 0.1. Here, the LCL and NS solutions are computed for the same geometries but with $\epsilon = 0.2$ to study the effect of the aspect ratio on the relative error. The variation of the relative error as a function of Re for each value of ϵ and for each geometry is plotted in Figure (2.14).

In all fractures, the relative error between the LCL and NS solutions is higher for $\epsilon = 0.2$, compared to the one obtained for $\epsilon = 0.1$. At low Re, the deviation of the LCL from NS solution due to the increase of ϵ is greater in the case of parallel walls (as seen in section

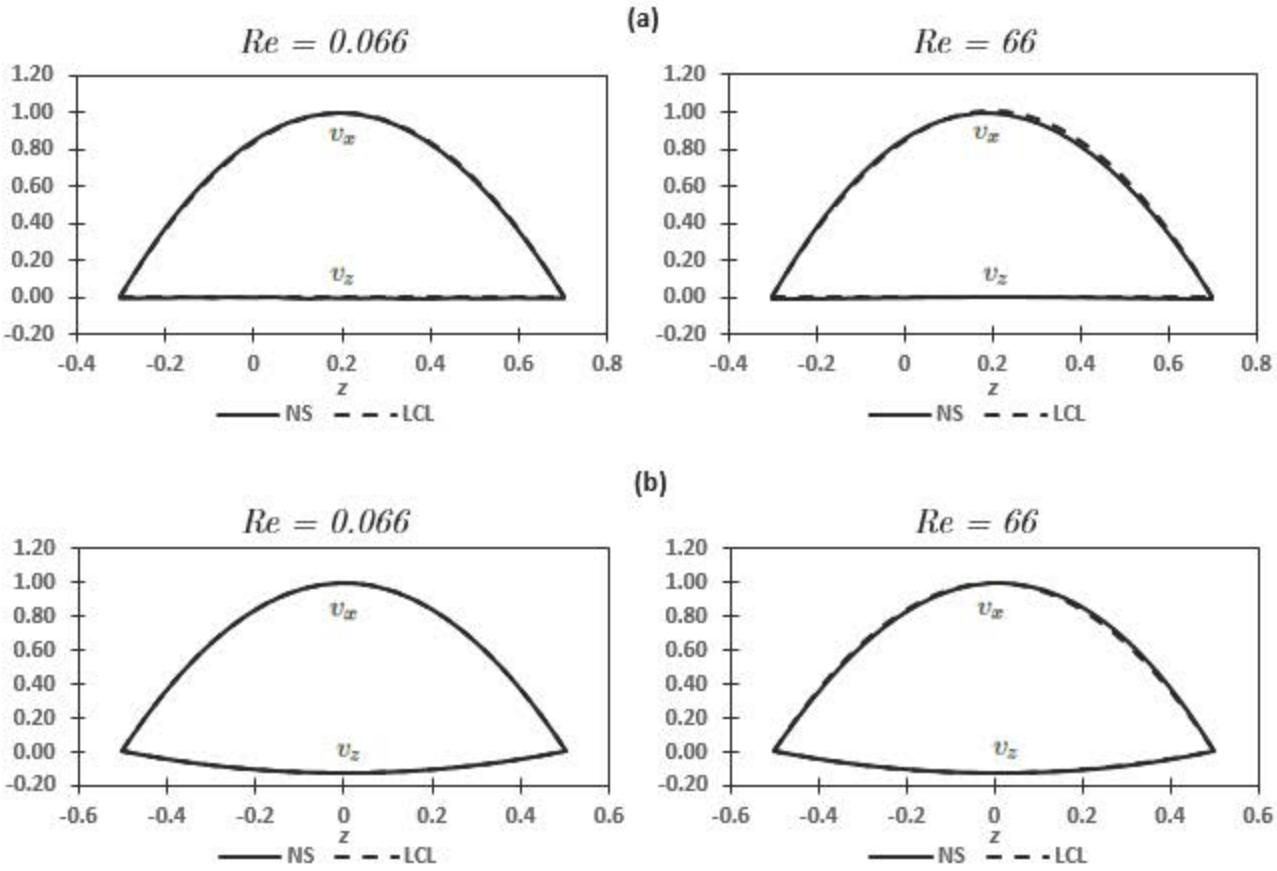

Figure 2.12: Dimensionless velocity profiles given by the LCL and NS solutions for $Re = 6.6 \times 10^{-2}$ and $Re = 6.6 \times 10^{1}$ in the case of a fracture with parallel walls. (a) velocity profiles on cut line 1. (b) velocity profiles on cut line 2

4.2.1). However, at high Re, the deviation becomes more important in the case of a channel with mirror symmetrical walls. In the case of a channel with arbitrary walls, the relative error tends to increase with the increase of ϵ and Re but remains nonetheless inferior to the error obtained for mirror symmetrical walls.

To study the effect of δ_0, different values are tested and compared to the reference geometries where δ_0 was fixed equal to 0.2. To investigate the effect of the walls corrugation amplitude, and therefore the walls roughness, on the deviation between the LCL and NS solutions, the two solutions are now computed for the same geometries but with $\delta_0 = 0.4$. The variation of the relative error as a function of Re for each value of δ_0 and for each geometry is plotted in Figure (2.15).

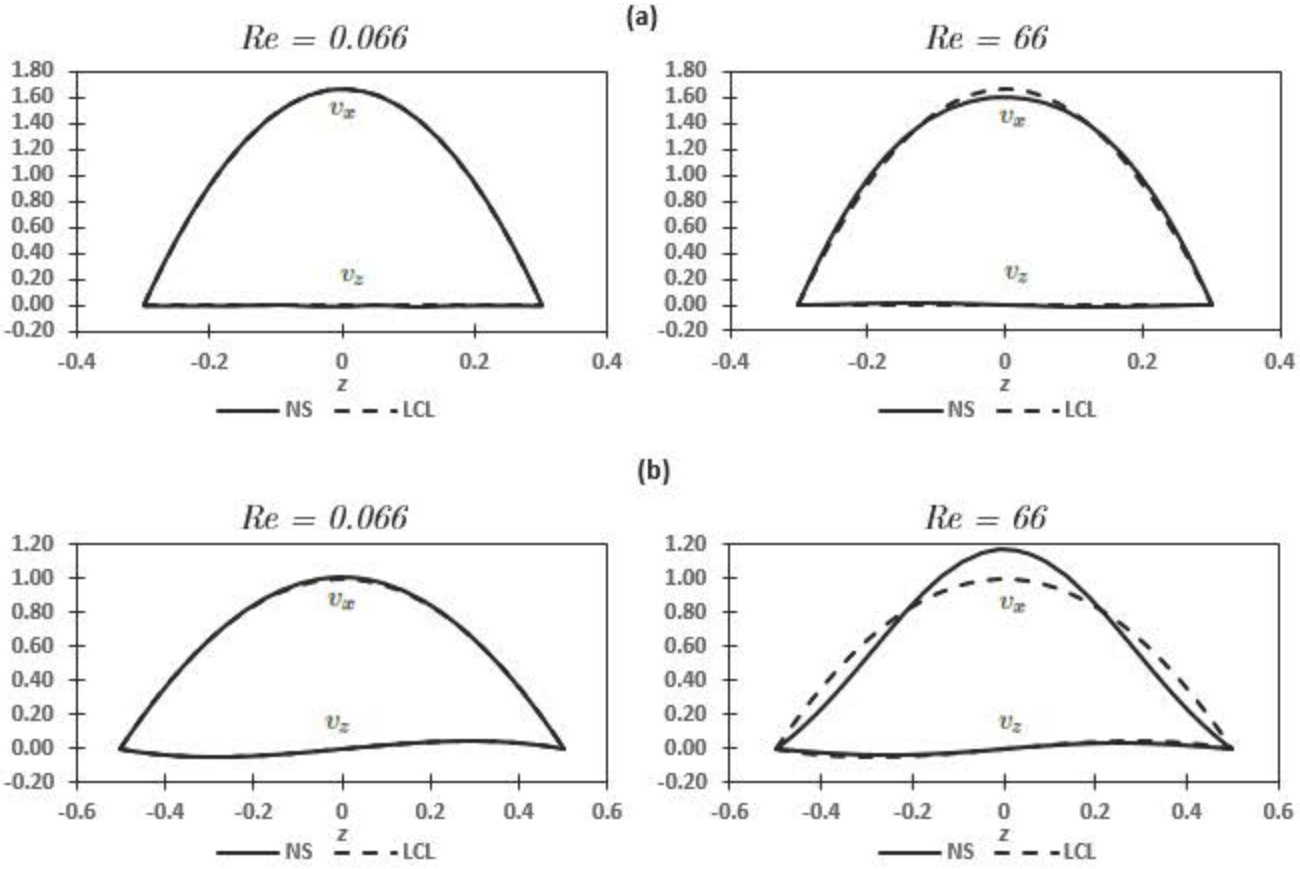

Figure 2.13: Dimensionless velocity profiles given by the LCL and NS solutions for $Re = 6.6 \times 10^{-2}$ and $Re = 6.6 \times 10^{1}$ in the case of a fracture with mirror symmetric walls. (a) velocity profiles on cut line 1. (b) velocity profiles on cut line 2

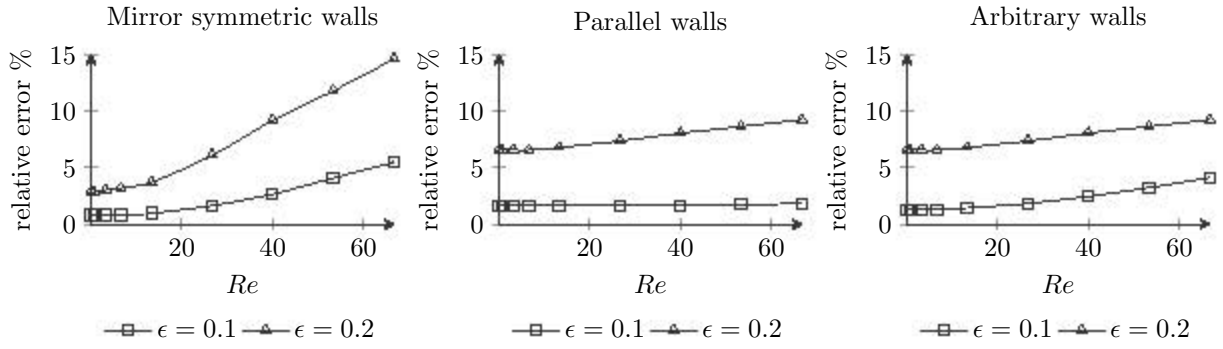

Figure 2.14: Variation of the relative error between the LCL and NS solutions as a function of Re. Comparison between $\epsilon = 0.1$ and $\epsilon = 0.2$ for fractures with parallel walls, mirror symmetric walls, and arbitrary walls.

For all the geometries, the relative error is higher for $\delta_0 = 0.4$, whatever the value of Re. However, for small Re, increasing δ_0 does not affect the relative error, while the error is

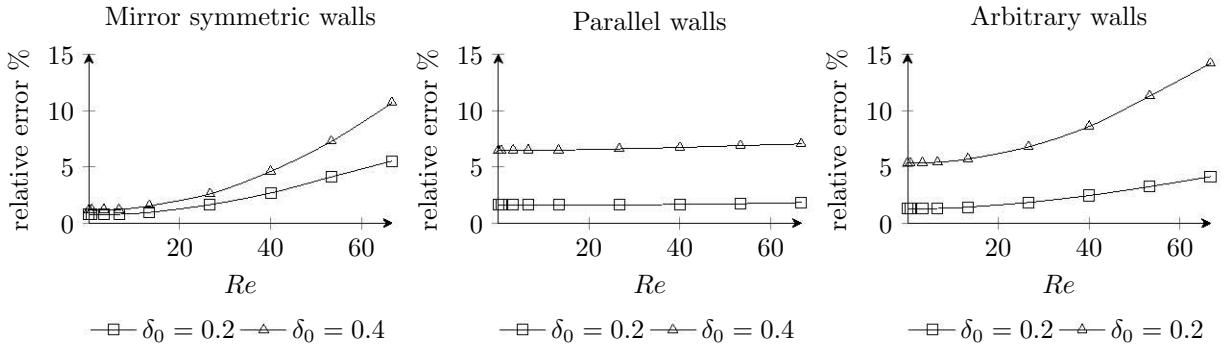

Figure 2.15: Variation of the relative error between the LCL and NS solutions as a function of Re. Comparison between $\delta_0 = 0.2$ and $\delta_0 = 0.4$ for fractures with parallel walls, mirror symmetric walls, and arbitrary walls.

higher for $\delta_0 = 0.4$ when Re is higher than 15.

In the reference geometries (Table 2.2), when the channels have parallel and mirror symmetric walls, $\gamma = 0$ because the walls have the same corrugation amplitude. We investigate the influence of the corrugation asymmetry by setting $\gamma = \frac{1}{3}$. In addition, we compare these two cases to the case of a fracture having a flat wall ($\gamma = 1$) to evaluate the effect of the asymmetry between the two walls on the validity of the LCL for high Re. The variation of the relative error as a function of Re for each geometry and for each reference geometry is plotted in Figure (2.16).

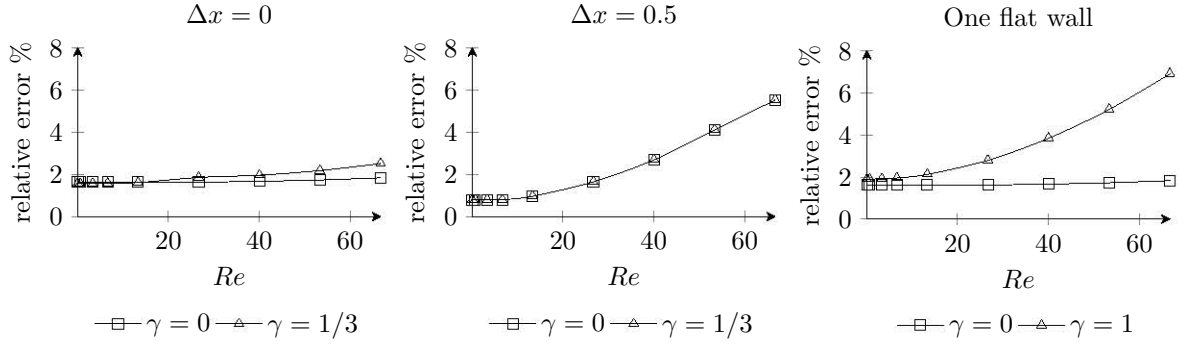

Figure 2.16: Variation of the relative error between the LCL and NS solutions as a function of Re for different values of the corrugations asymmetry γ.

When the phase shift between the two walls is maximum ($\Delta x = 0.5$), the variation of γ has no effect on the relative error whatever the value of Re. When the two walls are in phase ($\Delta x = 0$), the relative error increases slightly when Re increased. This increase is

more important in the case of a channel having a flat wall.

Once again, it is important to note that in all the cases studied in this section, the relative error remains relatively constant for $Re < 15$, meaning that the results obtained in section 4.2., on the effects of the fracture geometry on the validity of the LCL at low Re, remain valid for Re up to 15.

2.5 Discussions

2.5.1 Relation between the hydraulic and the mean apertures

The effect of the geometrical properties of a fracture on the discrepancy between its hydraulic aperture H_h and its mean aperture H_0 has been investigated. H_h and H_0 were compared to estimate the conditions under which the LCL, developed with respect to the hydraulic aperture H_h, can be replaced by the CL, developed with respect to the mean aperture H_0.

Analytical expressions of H_h based on Reynolds equation or the zeroth order solution of NS equations exist for specific geometries, like fractures having mirror-symmetric walls (Zimmerman et al. [81]), parallel and shifted walls (Basha and El Asmar [71]), and non-identical walls (Nizkaya [27]). These expressions show that H_h deviates from H_0 and depends clearly on the fracture geometry. Instead of considering specific geometries, we directly calculated H_h using equations (2.18) and (2.19), and plotted the variation of $\frac{H_h}{H_0}$ as a function of the average corrugation amplitude δ_0, the corrugations asymmetry γ and the horizontal phase shift Δx between the bottom and top walls (Figures (2.2) and (2.3)).

The results show clearly that, in most cases, H_h is smaller than H_0. This leads to a systematic overestimation of the flow rate by the CL compared to the LCL. However, these two apertures are equal in fractures with identical parallel walls ($\gamma = 0$ and $\Delta x = 0$) independently of the corrugation amplitude. This is consistent with the result of Basha and El Asmar [71] who found that the zeroth order solution of NS equations for such fractures does not depend on any geometrical parameter. In fact, in this particular case, even if δ_0 increases, the local aperture remains constant along the fracture length and is always equal to the mean aperture (Table 2.1(a)).

The deviation of H_h from H_0 increases when the walls are shifted and is maximum when the phase lag between the two walls is maximum ($\Delta x = 0.5$). This can be explained by the narrowing that appears inside the fracture with the increase of the phase shift (Table 2.1(b)). This narrowing leads to a decrease in the local aperture and therefore to a higher deviation between H_h and H_0. The same narrowing effect explains the diminution of H_h with the increase of the walls roughness and with the increase of the asymmetry between the two walls corrugations (Table 2.1(c)).

Therefore, the deviation of H_h from H_0 is not only due to the surface roughness, as these two apertures are equal in fractures with rough parallel walls. The deviation appears when the two walls are not in phase or when the two walls do not have the same corrugation amplitude, as a result of the variation in the local aperture.

It is important to note that H_h is calculated here using Reynolds equation (or the zeroth order solution of NS equations). Considering higher order solutions leads to additional terms that can not be considered using Reynolds equation alone (Sisavath et al. [86], Liu et al. [88]). These terms are not taken into account in the formulation of H_h in the current study.

2.5.2 Validity of the local cubic law for different Reynolds numbers

The validity of the LCL for modeling flow in rough fractures has been assessed for Re ranging from 6.7×10^{-2} to 6.7×10^{1} by comparing its solution to the numerical solution of NS equations and considering different geometries.

- **Low Reynolds number**: Although Reynolds equation is generally considered valid for $Re < 1$, the numerical results obtained cosidering $Re = 0.1$ show that the LCL solution can deviate significantly from the NS solution depending on the fracture geometry. This is consistent with the experimental results of Nicholl [93] who showed that Reynolds equation can overestimate the flow rate for Re as low as 0.06, and Lee et al. [94] who found that Reynolds equation is not always valid even for Re between 0.014 and 0.86.

The numerical results show that for $Re = 0.1$, the relative error between the LCL and the NS solutions increases for higher ϵ and δ_0. However, this error is minimal when the

walls are totally shifted and maximal when the walls are in phase. The asymmetry between the two walls γ has little effect on the deviation between the two solutions. This confirms that the validity of the LCL is highly dependent on the fracture geometry. This may also explain the discrepancy in the previous geometrical criterion proposed for the applicability of Reynolds equation ($\epsilon\delta_0 < 0.14$ suggested by Zimmerman et al. [81] for a mirror-symmetric fracture, $\epsilon^2\delta_0 < 0.01$ by Yeo and Ge [87] for a fracture with parallel walls and $\epsilon < 0.33$ by Zimmerman et al. [72] for a fracture with one flat wall and one sinusoidal one).

To understand the origin of this discrepancy, Lee et al. [94] performed direct visualizations of flow velocity through rough-walled fractures for Re ranging between 0.014 and 0.86, and found that inertial forces are negligible with respect to viscous forces. This means that the fracture geometrical properties are solely responsible for the deviation between the LCL and NS solutions for low Re. In fact, walls roughness causes curvature in the flow streamlines that induces flow tortuosity and energy dissipation. In order to analyze the impact of the fracture geometry on the flow streamlines, the flow streamlines obtained numerically for $Re = 0.1$ considering four different geometries are plotted in Figure 2.17. For all the cases, ϵ was fixed equal to 0.1, so that he assumption $\epsilon << 1$ is verified.

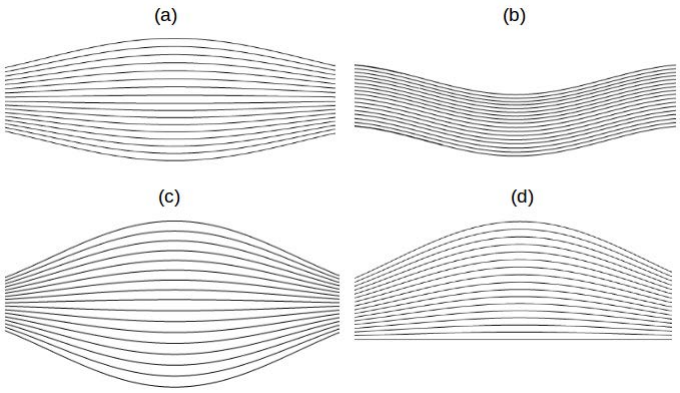

Figure 2.17: Flow streamlines plotted for four different fracture geometries: (a) $\Delta x = 0.5$, $\delta_0 = 0.25$ and $\gamma = 0$. (b) $\Delta x = 0$, $\delta_0 = 0.25$ and $\gamma = 0$. (c) $\Delta x = 0.5$, $\delta_0 = 0.4$ and $\gamma = 0$. (d) $\delta_0 = 0.25$ and $\gamma = 1$. $Re = 0.1$ and $\epsilon = 0.1$ are fixed in all the cases

The effect of the horizontal phase shift Δx can be highlighted by comparing cases (a) and (b) where $\delta_0 = 0.25$ and $\gamma = 0$ in both cases (Figure (2.17)). For $\Delta x = 0.5$, the streamlines are mainly curved near the fracture walls and this curvature decreases when approaching the fracture center where the streamlines become quasi flat. For $\Delta x = 0$, the streamlines

are curved independently of their position inside the fracture. Therefore, for higher Δx the overall curvature of the streamlines reduces, which explains why the deviation of the LCL from NS solution is greater for lower phase shift between the walls (Figure (2.10)).

Comparing cases (a) and (c) (Figure (2.17)) shows that for the same values of $\Delta x = 0.5$ and $\gamma = 0$, increasing the dimensionless corrugation amplitude δ_0 from 0.2 to 0.4 produces streamlines with higher curvature. This explains why increasing δ_0 leads to a higher error when comparing the LCL and the NS solutions (Figure (2.8)).

Case (d) corresponds to a fracture having a bottom flat wall and a top corrugated wall ($\gamma = 1$), with $\delta_0 = 0.25$. Near the bottom wall, the streamlines are straight and their curvature increases when they are closer to the top wall. This is similar to case (a) where $\Delta x = 0.5$ but different than (b) where $\Delta x = 0$. This explains why increasing γ has a stronger effect on the deviation of the LCL solution for lower Δx than for higher Δx (Figure (2.9)).

These results suggest that the deviation between the LCL and NS solutions increases when the overall curvature of the streamlines increases. This is due to several effects. First, the curvature of the streamlines leads to a tortuous flow. Tortuosity represents the ratio of the length of the trajectory of the flow between two points and the distance between these two same points. In fact, equation (2.17) is established assuming that a fluid particle travels a distance equal to L_0, which would be valid in a channel with flat walls. However, in rough channels, because of the curvature of the streamlines (especially near the walls), fluid particles travel longer distances. Second, the viscous dissipation is more significant when the streamlines are curved due to their disruption especially near the channel throats (Basha and El Asmar [71]). In fact, as the viscous dissipation is proportional to the velocity gradient, it increases when the streamlines are narrowed. All these effects point to the fact that the curvature of the streamlines is the source of deviation between the LCL and NS solutions at low Re, as confirmed by the numerical results.

- **High Reynolds number**: If Re increases, flow inertial effects become significant and the fracture flow does not exhibit a Darcian behavior ([102], [107]). This leads to a higher deviation of the LCL with respect to the NS solution.

From our study, it appears that, for every case studied, the relative error between the two

solutions remained quasi-constant for $Re < 15$, implying that the conclusions drawn for low Re can be valid for Re values up to 15. It confirms the analytical solution obtained by Nizkaya [27] for mirror-symmetric channels. It is somewhat consistent with the result obtained by Zimmerman et al. [72] who, using an order of magnitude analysis of NS equations for a channel having one flat wall and one sinusoidal wall, argued that inertial effects become significant for $Re > 10$. It is also in agreement with the results suggested by Zimmerman et al. [107] who conducted experimental and numerical simulations on flow in a natural fracture and showed that inertial effects become important for Re starting between 10 and 20. As the condition $Re > 15$ was found in all the geometries that we considered (Figures 2.14, 2.15 and 2.16), one can generalize the result for any fracture geometry.

Our numerical results show that the relative error does not change as a function of Re in the case of parallel walls. This is in agreement with the analytical results of Basha and El Asmar [71] and Nizkaya [27] who found that inertial terms are null in the first and second order terms of the NS expansion solution. On the other hand, this error is maximum when the phase shift between the two walls Δx is maximum.

In all cases, the relative error between the LCL and NS solutions for higher Re increases with increasing ϵ. This error is higher when the walls are shifted than when they are in phase. A similar tendency appears when δ_0 and/or γ increase. The deviation is more important when the asymmetry between the walls increases, and reaches its maximum in channels having one flat wall.

These results prove that for high Re, the fracture geometrical properties should be taken into account to describe the deviation between LCL and NS . This confirms the result obtained by Qian et al. [102] who showed that fracture flow depends both on Re and on the walls roughness.

In order to study the impact of the fracture geometry on the flow inertial effects, the flow streamlines obtained numerically for $Re = 26.66$ considering four different geometries are plotted in Figure 2.18. Comparing cases (a) and (b) that have the same δ_0 and γ, shows that when the horizontal phase shift $\Delta x = 0$, the velocity remains constant on the same streamline so that the velocity variation is only in the vertical direction, like in the case of flat walls. In case (a) where $\Delta x = 0.5$, one can see that the flow is slower in the channel when

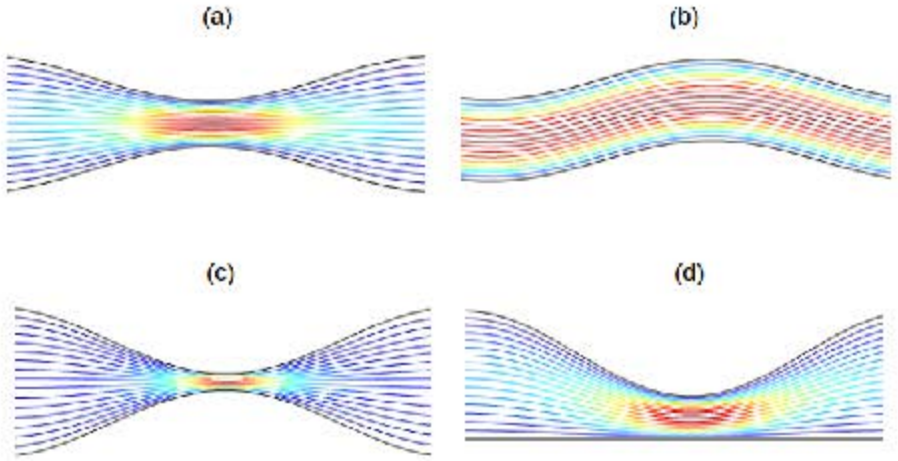

Figure 2.18: Flow streamlines in four different fracture geometries for $Re = 26.66$ and $\epsilon = 0.1$ (a) $\Delta x = 0.5$, $\delta_0 = 0.25$ and $\gamma = 0$. (b) $\Delta x = 0$, $\delta_0 = 0.25$ and $\gamma = 0$. (c) $\Delta x = 0.5$, $\delta_0 = 0.4$ and $\gamma = 0$. (d) $\delta_0 = 0.25$ and $\gamma = 1$. The streamlines are colored according to the velocity of the fluid flow. The blue color corresponds to low flow velocities and red color corresponds to high velocities

the local aperture is at its maximum and accelerates when the aperture is constricted causing an alternation of repeated acceleration and deceleration along the fracture length. This effect becomes more important when Re increases. This phenomena explains why increasing Δx leads to a higher error between the LCL and NS solutions as Re increases.

Comparing cases (a) and (c) shows that for the same ϵ, γ and Δx, the alternation in the fluid movement is more pronounced when the dimensionless amplitude δ_0 is higher. This is due to the fact that the flow becomes faster as the channels aperture is narrowing. This explains why the deviation of the LCL from NS solution is greater for higher δ_0 (Figure (2.15)).

Case (d) corresponds to a fracture having a lower flat wall and a top corrugated wall ($\gamma = 1$), with $\delta_0 = 0.25$. The repeated acceleration-deceleration of the flow in this case is similar to case (a) and it is also due to the aperture variation. This explains why for higher Re, a higher value of γ increases the deviation of the LCL from NS solution (Figure (2.16)).

These results suggest that for higher Re, inertial effects become significant due to repeated acceleration and deceleration of the fluid inside the fracture. The fracture geometry gives rise to this alternation in the fluid movement by inducing variation in the local aperture along the flow direction. Therefore, the deviation between the LCL and the NS solutions at

high Re in rough-walled fractures is due to the increase of inertial effects that result directly from the fracture geometry.

To sum up, the fracture geometrical properties affect greatly the flow. At low Re, the curvature of the streamlines induced by the fracture geometry increases tortuosity and energy dissipation, leading to a deviation between the LCL and NS solutions. At high Re, typically higher than 15, this deviation is due to inertial effects that are more or less pronounced depending on the fracture geometry.

2.6 Conclusion

In this chapter, the effects of the geometry of rough fractures on the applicability of the CL and the LCL have been investigated, considering fractures with sinusoidal walls.

Our results confirm that care must be taken when using the CL to model flow in rough-walled fractures. More specifically, if the CL can replace the LCL as long as the walls corrugations are relatively small or when the walls are identical and parallel, it clearly overestimates the flow once the corrugations amplitude become significant in fractures having walls that are shifted and/or with different corrugation amplitudes.

The LCL is valid to model fluid flow in rough-walled fractures at low Re, especially in fractures with small aspect ratios and low corrugation amplitudes. However, the deviation between the LCL and NS solutions increases even at low Re when the walls are in phase and when both walls present high corrugation amplitude. This deviation is due to the curvature of the streamlines which increases the tortuosity and energy dissipation inside the fracture, depending on the geometrical properties of the fracture.

When Re increases, inertial effects become significant for $Re > 15$. This means that the conclusions drawn for low Re can be valid for Re up to 15. Above this limit, the LCL can still be valid to model the flow provided that the fracture presents small aspect ratio, corrugation amplitudes, and small variations in the local aperture along the flow direction. When these conditions are not respected, the repeated acceleration and deceleration of the flow due to the variation of the local aperture tends to promote the inertial effects and therefore enhances the deviation between the LCL and NS solutions.

In conclusion, a quantitative estimation of the error made when using the LCL, and even the CL, to model fluid flow in rough fractures was given. It is shown that, because fracture flows are strongly dependent on the fracture geometry, the criteria proposed in the literature for applying the cubic law and the local cubic law are not sufficient to be generalized for random fracture geometries. However, the LCL is valid to model the flow for low Re in channels with low aspect ratio ϵ.

Chapter 3

TRANSPORT AND DEPOSITION OF WEAKLY-INERTIAL PARTICLES IN FRACTURE FLOWS

This chapter is devoted to the study of particle transport in fractures, assuming that the flow can be described by the LCL as discussed in chapter 2. The particles are non-Brownian, passive, and much smaller than the fracture aperture. Their inertia is considered very small so that it can be neglected in the equation of motion. The equation of motion is coupled to the flow velocity field as predicted by the LCL to provide a model that can predict the particles' behavior inside the fracture (transport and/or deposition) as well as their trajectories. In order to validate this simplified model, its predictions are systemically verified against numerical simulations where the full NS equations are solved, taking into account particle inertia and flow inertial effects. Based on the trajectory equation, regime diagrams that can predict the behavior of particles entering closed fracture flows are built. These diagrams enable to forecast if the particles entering the flow will be either deposited or transported along the fracture. The influence of the fracture geometry on the particle behavior is then investigated

by considering channels with flat and sinusoidal walls. In particular, the effect of the corrugation amplitude, of the asymmetry and of the phase lag between the walls on the extent of the transport and deposition regimes is evaluated. Here again, the results are systemically verified against numerical experiments taking into account particle inertia and fully resolving the NS equations. The main results of this chapter have been published in the European Journal of Mechanics B/Fluids (Hajjar et al. [1]).

Introduction

As shown in chapter 1, the motion of particles immersed in a fluid flow is very difficult to predict due to different effects related to the particle properties and flow characteristics.

Many previous works on particle motion in closed channel flows focused on the phenomena of lift-induced particle migration across the streamlines, principally because of its crucial implication in microfluidics (Di Carlo et al. [35], Martel and Toner [36]). These works targeted the effect of the particle size and flow characteristics on the order of magnitude of the different inertial lift forces. Because lift-induced particle migration occurs when particle motion is dominated by the inertial lift forces, particle inertia has not been generally considered.

Taking into account particle inertia, Jebakumar et al. [108] investigated the effects of Stokes number on particle trajectories in wall-bounded vertical channel flow and found that for small Stokes number, particles behave similarly to neutrally buoyant particles. However, few works have investigated the effect of gravity on the behavior of non neutrally buoyant particles in horizontal channel flows. For example, Chen et al. [109], [110] studied the deposition of charged particles in straight and convergent channels, investigating the contribution of gravity and image forces in the particle deposition process. Even less works considered particle transport and deposition in fractures and in closed channels with corrugated walls. For instance, based on migration conditions formulated initially by Sapsis and Haller [111], Nizkaya et al. [16] neglected fluid inertia and studied particle focusing in channels with periodic corrugated walls. In particular, they showed that, even if the fluid inertial effects

are neglected, focusing can occur due to particle inertia and to the waviness of the streamlines imposed by the walls corrugation. These authors also defined a trapping diagram that predicts the presence of inertial focusing as a function of the channel geometry and of the flow Froude number.

In the present work, particle inertia, which is defined by Stokes number and the particle response time, is so small that the focusing phenomenon predicted by Nizkaya et al. [16] is not expected to occur. The flow is unidirectional, laminar and follows the LCL. In addition, the particles are assumed to be sparsely distributed inside the fluid so that the flow affects the motion of the particles, but not vice versa. In other words, only one way coupling between the solid and fluid phases is considered.

Chapter outline: In section 1, the trajectory equations of particles immersed in fluid flows occurring in channels with both flat and corrugated walls are developed. In section 2, these equations are verified through numerical simulations using a hybrid technique combining a finite element method and a Lagrangian particle tracking method. In section 3, the diagram defining different particle transport regimes is established, and its validity is demonstrated by comparing their predictions against numerical experiments. In section 4, the main results obtained in this chapter are summarized and discussed.

3.1 Governing equations

We consider 2D flows. The domain is represented in a reference frame (X, Z) where X corresponds to the horizontal direction (the main flow direction) and Z to the vertical one. Gravity is taken into account and applies perpendicularly to the main flow direction (along Z). To simplify the problem, We consider a solid spherical particle of radius a and density ρ_p moving at a velocity V_p in a fluid of density ρ_f and dynamic viscosity μ flowing at a velocity V_f.

3.1.1 Forces acting on each particle

The forces involved when a particle is being driven by a closed channel flow are:

- Gravity and buoyancy forces F_g: they are significant when there is a noticeable dif-

ference between the particle and the fluid respective densities. The fluid applies an upward thrust upon the particle which is equal to the weight of an equal volume of the liquid displaced. Combining the weight and thrust forces, the resulting force is equal to:

$$F_g = \frac{4}{3}\pi a^3(\rho_p - \rho_f)g \tag{3.1}$$

g being the gravity acceleration. This force is equal to zero for non-buoyant particles.

- Drag force F_d: this force results from the pressure and the viscous frictional forces exerted by the fluid on the surface of the particle, in the case of uniform continuous flow. The mathematical expression of the drag force depends on the flow regime around the particle. It is characterized by the particle Reynolds number $Re_p = \frac{\rho_f(V_p - V_f)2a}{\mu}$. In the Stokes or viscous regime, when $Re_p << 1$, the resolution of Stokes equations leads to the following mathematical expression of the drag force:

$$F_d = -6\pi\mu a(V_p - V_f) \tag{3.2}$$

- Added mass force F_{am} (Auton et al. [112]): during its motion, the particle displaces a volume of the surrounding fluid. An additional inertia therefore arises from the acceleration of the displaced fluid mass. This phenomenon produces the added mass force of which the expression, in the case of a spherical particle, is given by:

$$F_{am} = \frac{m_f}{2}(\frac{DV_f}{Dt} - \frac{dV_p}{dt}) \tag{3.3}$$

$m_f = \frac{4}{3}\rho_f\pi a^3$ being the mass of the fluid displaced by the sphere and $\frac{DV_f}{Dt}$ the total derivative with respect to time.

- Tchen Force F_{Tchen} ([113]): it represents the action exerted by the undisturbed flow on the volume of fluid occupied by the particle. It is calculated by integrating the pressure gradient exerted by the undisturbed fluid on the particle volume and by subtracting the hydrostatic contribution (which corresponds to the buoyancy thrust). This force

involves only the characteristics of the fluid and is expressed as follows:

$$F_{Tchen} = m_f \frac{DV_f}{Dt} \tag{3.4}$$

- History force F_h: known also as the Basset-Boussinesq force ([114]), it is due to the non-stationarity of the disturbance flow around the particle and reflects the effect of the delay caused by the viscous diffusion of the momentum. Indeed, the particle displaces a quantity of fluid, which disturbs the established flow and a time is therefore necessary for the stationary regime to be recovered. This force is expressed in an integral form retaining the whole history of the particle acceleration, as follows:

$$F_h = -6\pi a^2 \sqrt{\mu \rho_f} \int_{-\infty}^{t} \frac{1}{\sqrt{\pi(t-t')}} \frac{d}{dt'} [\vec{V_p} - \vec{V_f}] dt' \tag{3.5}$$

  In this thesis, we consider that the disturbance flow around the particle is steady so that the history force is neglected.

- Lift forces F_l: these inertial forces occur when there is a pressure gradient in the direction orthogonal to that of the particle motion. This pressure gradient results from a rotational movement or the shear in the flow of the carrier fluid. Lift forces are nil in the case of Stokes regime ($Re_p = 0$). The lift forces acting on a particle in the case of a channel flow are detailed below.

Four types of lift forces develop in channel flows: rotation-induced (Magnus), shear-slip (Saffman), shear gradient, and wall-induced lift forces (Figure 3.1). The reviews of Zhang et al. [115] and Martel and Toner [36] explain in detail the effect of each one of these forces and how they are scaled to Re and to the ratio of the particle diameter to the channel height. We recall here a brief summary of these forces and their effects.

- Magnus rotation-induced lift force: this force appears when a particle is rotating in a uniform flow, so it is not limited to bounded or channel flows. Suppose that the rotational velocity ω of a spherical particle is in the direction of the flow, the particle perturbs the surrounding velocity field asymmetrically and drags the fluid faster around

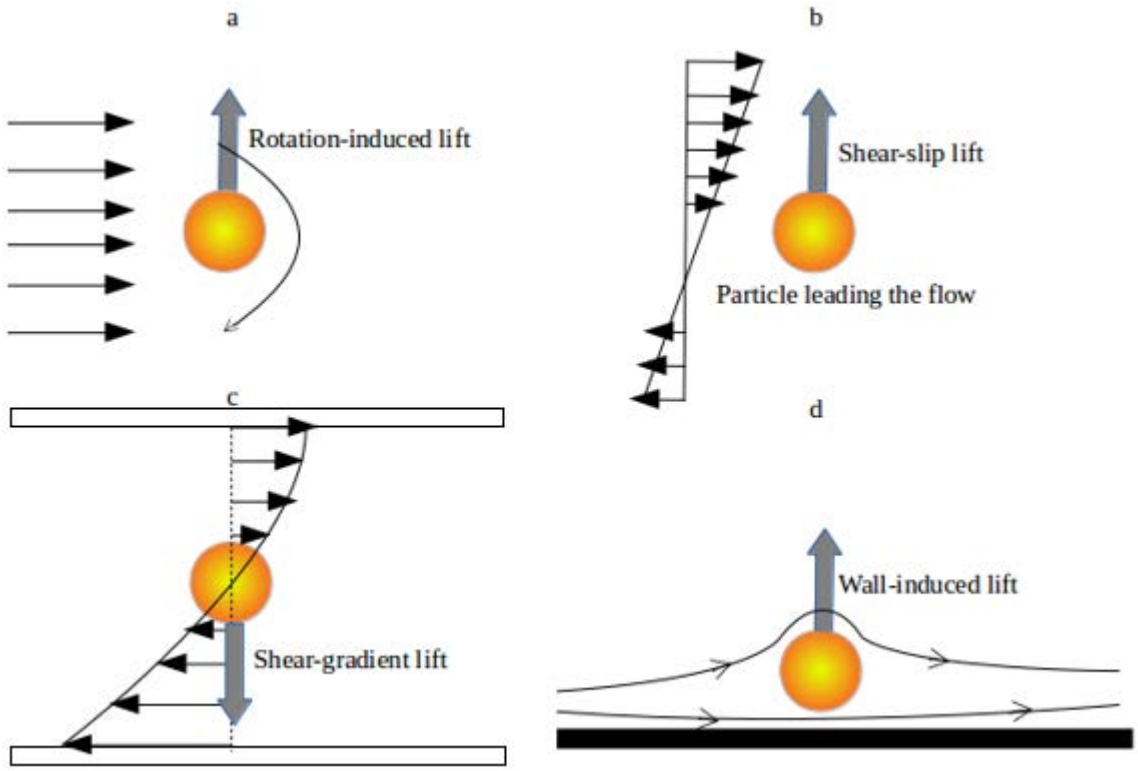

Figure 3.1: Different types of lift forces: (a) Magnus rotation-induced, (b) Saffman shear-slip, (c) shear-gradient and (d) wall-induced forces

its upper side. Bernoulli principle states that when the fluid velocity increases, the pressure decreases. Therefore, the pressure difference which appears between the lower and upper sides of the spherical particle creates a force in the direction of the pressure gradient. This force, perpendicular to the flow direction, is called the Magnus force ([116]).

- Saffman shear-slip lift force: this force acts on particles that lead or lag the fluid in shear flows. The difference between the particle and the fluid velocities generates a force directed towards the high velocity region. The Saffman force is significant when external forces (gravitational, electric, magnetic) affect the particle relative velocity with respect to the fluid. Examples include the case of non-neutrally buoyant particles transported in a vertical flow, where the gravity can accelerate or decelerate the particle according to the relative difference between the particle and the fluid respective densities.

- Shear-gradient lift force: This force acts on particles immersed in Poiseuille flows and is induced by the shear gradient resulting from the curvature of the velocity profile in the channel. In fact, due to the presence of the walls, the velocity is zero at the channel walls (no-slip) and increases gradually to reach its maximum at the channel center, leading to a parabolic velocity profile. In the presence of a particle, the relative velocity of the fluid to the particle is lower in the channel center region than the near-wall region, and thus leading to a force directed toward the channel walls.

- Wall-induced lift force: This force acts on the particles in the near-wall region. excess pressure is created in the constriction between the particle and the wall, causing a force directed away from the wall. In fact, the flow streamlines are more curved on the side of the particle directed toward the channel center than in the constriction between the particle and the wall leading to higher velocity in the curved region and therefore to a higher pressure in the constriction. The resulting lift force is directed toward the channel center.

Net inertial lift force: the effect of inertial lift forces can be understood by their implication in the appearance of inertial focusing behavior. Ho and Leal [117] and Vasseur and Cox [118] found analytically that the balance between the shear-gradient lift force and the wall-induced lift force explains the particle migration toward equilibrium positions inside the channel. Their results further showed that the Saffman shear-slip and Magnus rotation-induced lift forces are respectively one order and three orders of magnitude smaller than the shear-gradient lift force. Saffman and Magnus forces are therefore generally neglected when studying of inertial focusing.

The main effect of inertial lift forces on particle transport in closed channel flows is to produce a lateral migration of particles with respect to the flow direction, especially for non-buoyant particles. Bretherton [119] demonstrated theoretically that lateral migration can not occur under Stokes flow conditions. Lift forces can thus be neglected when no inertial migration is expected to occur. Di carlo et al. [35] have shown through experimental observations that for very low particle Reynolds number (defined as $R_p \simeq \frac{U_0 a^2}{\nu H_0}$ in this case), non-buoyant particles do not migrate across streamlines and therefore inertial lift forces

are negligible with respect to other forces. They also showed that in serpentine channels, even for higher R_p, lift forces remain negligible for particle radius to channel width ratios $a/H_0 < 0.035$. This result was later verified by Zhang et al. [120] who performed numerical simulations without considering the inertial lift forces and found a very good agreement with their experimental observations. These results confirm that for very low Rp and small $\frac{a}{H_0}$, it is reasonable to neglect inertial lift forces. Therefore, in the developments presented throughout the following sections, we neglect the inertial lift forces by making the assumption that flow inertial effects are negligible (LCL model) and that the particles are much smaller than the channel aperture.

3.1.2 Particle motion equation and particle trajectory equation

The particle motion equation is obtained by applying Newton's second law of motion to a single particle, stating that the sum of forces acting on a particle is equal to the product of its mass by its acceleration. When the particle diameter is small and when Re as well as the velocity gradient around the particle are small, the equation of motion of a solid spherical particle of radius a and density ρ_p moving in a fluid of density ρ_f and dynamic viscosity μ, as derived by Maxey and Riley [121] and Gatignol [122], with corrected added mass term (Auton et al. [112]) can be written, in the dimensionless form, as:

$$\begin{aligned}\frac{d\vec{v_p}}{dt} &= (1-\frac{3R}{2})\vec{G} \\ &\quad -\frac{1}{\tau}(\vec{v_p}-\vec{v_f}-\frac{a^2}{6L_0}\nabla^2\vec{v_f}) \\ &\quad -\frac{3R}{2}\frac{D}{Dt}[(\vec{v_f}+\frac{a^2}{20L_0}\nabla^2\vec{v_f})] \\ &\quad \frac{3\sqrt{R}}{\sqrt{2\tau}}\int_{-\infty}^{t}\frac{1}{\sqrt{\pi(t-t')}}\frac{d}{dt'}[\vec{v_p}-\vec{v_f}-\frac{a^2}{6L_0}\nabla^2\vec{V_f}]dt'\end{aligned} \tag{3.6}$$

where the total length of the fracture L_∞ is selected as a horizontal length scale, and V_0 as a velocity scale, so that the following dimensionless parameters were defined: $h^* = \frac{H_0}{L_\infty}$, $x = \frac{X}{L_\infty}$, $z = \frac{Z}{H_0}$, $v_f^x = \frac{V_f^x}{V_0}$ and $v_f^z = \frac{1}{h^*}\frac{V_f^z}{V_0}$. $\frac{d}{dt}$ denotes the derivative with respect to time taken along the particle trajectory, and $\vec{G} = \vec{e_z}/Fr$, $Fr = \frac{V_0^2}{L_0 g}$ being Froude's

number. The forces taken into account in this equation are (according to their order of appearance): gravity and buoyancy forces, drag force, added mass contribution, force due to the pressure gradient of the unperturbed flow, and Basset history force due to unsteadiness of the disturbance flow around the particle. We assume that this disturbance flow is steady so that Basset force can be neglected. The terms proportional to the Laplacian of the velocity field, known as Faxen corrections ([123]), are due to the non-uniformity of the fluid flow at the particle scale. They are neglected under the assumption that the particle radius is substantially small compared to the characteristic length L_0 of the flow.

Under these conditions, i.e. neglecting Basset force and Faxen corrections terms, and developing the terms of the right-hand side of equation (1), we can write:

$$\frac{L_0}{V_0}\frac{d\vec{V_p}}{dt} = \frac{1}{\tau}(\vec{V_f} - \vec{V_p} + \frac{2}{9}\frac{a^2(1-k)g}{\nu}\frac{\vec{g}}{|g|}) + \frac{L_0}{V_0}\frac{3R}{2}\frac{D}{Dt}(\vec{V_f}) \tag{3.7}$$

In this case, $\tau = \frac{2}{9R}\frac{a^2 V_0}{\nu L_0} = \frac{St}{R}$ represents the particle dimensionless response time, St being the Stokes number and $R = \frac{2\rho_f}{2\rho_p+\rho_f} = \frac{2}{2k+1}$ a dimensionless number where $k = \frac{\rho_p}{\rho_f}$ is the ratio of particle density to fluid density, V_0 is the flow mean velocity and ν is the fluid kinematic viscosity. The fluid flow is governed by the LCL. As shown in chapter 2, the flow velocity components are equal to:

$$V_f^X = \frac{3V_0H_0}{4H(X)}(1-\eta^2) \text{ and } V_f^Z = \frac{3V_0(\phi'(X)+\eta H'(X))}{4H(X)}(1-\eta^2) \tag{3.8}$$

where $H'(x)$ and $\Phi'(x)$ correspond respectively to the variations of the dimensionless fracture aperture and fracture middle line along the flow direction

Particle inertia can be measured by the dimensionless response time τ, defined as the ratio between the particle characteristic time (particle relaxation time) and the flow characteristic time $T_0 = \frac{L_0}{V_0}$. In this study, we consider weakly inertial particles i.e. $\tau << 1$. A similar assumption was made by Nizkaya [27] to study particle focusing in channels with periodic walls. Nonetheless, in the current thesis, particle inertia will be neglected (in the analytical developments) so that focusing is not expected to occur. In the next section, we recall briefly the result obtained by Nizkaya [27] to highlight the difference between her approach and the approach adopted in the present thesis. Then, we define, according to the order of magnitude

of each term in the particle motion equation, the value of τ under which we assume that particle inertia can be neglected.

3.1.2.a. Focusing of weakly inertial particles in channels with periodic walls

L_0 and H_0 are set as length scales, and V_0 as velocity scale. The solution of equation (3.7) is known to converge exponentially to the first order equation ([121], [8]):

$$\vec{v_p} = \vec{v_f} + \tau(\frac{3R}{2} - 1)(\frac{D\vec{vf}}{Dt} - \vec{G}) + O(\tau^2) \tag{3.9}$$

The components of equation (3.9) are respectively equal to:

$$v_p^x = v_f^x - \tau(\frac{3R}{2} - 1)\frac{D}{Dt}(v_f^x) \;\; and \;\; v_p^z = v_f^z - \tau(\frac{3R}{2} - 1)G - \tau(\frac{3R}{2} - 1)\frac{D}{Dt}(v_f^z) \tag{3.10}$$

In order for particle focusing to occur, the trajectories of moving particles are assumed to coincide with an attracting streamline. A flow streamline is defined by $\frac{dz_f}{dx_f} = \frac{v_f^z}{v_f^x}$ whereas the particle trajectory is defined by $\frac{dz_p}{dx_p} = \frac{v_p^z}{v_p^x}$. When the particle trajectory and a flow streamline coincide, the particle follows the streamline and its trajectory is defined by the streamline equation, meaning that:

$$\frac{v_p^z}{v_p^x} = \frac{v_f^z}{v_f^x} \tag{3.11}$$

Replacing the particle velocity components using equation (3.10) leads to:

$$\frac{v_f^z - \tau(\frac{3R}{2} - 1)G - \tau(\frac{3R}{2} - 1)\frac{D}{Dt}(v_f^z)}{v_f^x - \tau(\frac{3R}{2} - 1)\frac{D}{Dt}(v_f^x)} = \frac{v_f^z}{v_f^x} \tag{3.12}$$

which gives:

$$\frac{\frac{D}{Dt}(v_f^z) - G}{\frac{D}{Dt}(v_f^x)} = \frac{v_f^z}{v_f^x} \tag{3.13}$$

In the case of stationary flow, equation (3.13) can be written as:

$$\frac{v_f^x \frac{d}{dx}(v_f^z) + v_f^z \frac{d}{dz}(v_f^z) - G}{v_f^x \frac{d}{dx}(v_f^x) + v_f^z \frac{d}{dz}(v_f^x)} = \frac{v_f^z}{v_f^x} \tag{3.14}$$

Noting $\beta(x,z) = \frac{v_f^z}{v_f^x}$, equation 3.14 can be developed, for the case of a steady flow, and leads to:

$$(v_f^x)^2(\frac{d\beta}{dx} + \beta\frac{d\beta}{dz}) - G = 0 \tag{3.15}$$

Replacing the expressions of v_f^x, β, and G into equation (3.15) leads to a relation between z and x which defines the preferential trajectory.

For a flow following the LCL, $\beta = \epsilon(\phi'(x) + \eta h'(x))$ and equation (3.15) gives:

$$\frac{16h(x)^2 G}{9(1-\eta^2)^2} - [\epsilon(\phi''(x) + \eta h''(x)) + \epsilon^2 \frac{h'(x)}{h(x)}(\phi'(x) + \eta h'(x))] = 0 \tag{3.16}$$

The η coordinate of the attracting streamline is the solution of equation (3.16). In a specific channel, the expressions of $h(x)$ and $\phi(x)$ are known and their derivatives can be calculated. Equation (3.16) can be numerically solved to find the expression of η. To do so, equation (3.16) is integrated along one wavelength (x between 0 and 1), with $\phi'(0) = \phi'(1)$ and $h'(0) = h'(1)$, and gives:

$$\gamma_z^1 - (1-\eta^2)^2(\Delta + \eta) = 0 \tag{3.17}$$

$\gamma_z^1 = \frac{16G}{9(2\epsilon - \epsilon^2)J_h}$ being the inverse Froude number, and $\Delta = \frac{J_{\phi h}}{J_h}$, with $J_h = \int_0^1 \frac{h'(x)^2 dx}{h(x)^3}$ and $J_{\phi h} = \int_0^1 \frac{h'(x)\phi'(x)dx}{h(x)^3}$ two shape factors that characterize the channel geometry.

3.1.2.b. Trajectory equation of inertia-free particles

We consider the case where the particle response time τ is very small so that the term proportional to $1/\tau$ is dominant in equation (3.7) compared to the two other terms, and

equation (3.7) can thus be simplified to:

$$\vec{V_p} = \vec{V_f} + \frac{2}{9}\frac{a^2(k-1)g}{\nu}\frac{\vec{g}}{|g|} \tag{3.18}$$

where $\frac{\vec{g}}{|g|}$ is a vertical unit vector pointing in the downward direction. This equation applies to inertia-free sedimenting particles and has been already used in the past (e.g. Stommel [20]). Bergougnoux et al. [124]) studied experimentally the motion of solid particles in a spherical flow field and found that particle inertia can be safely neglected for $\tau < 10^{-2}$. Similarly, we assume that the model that we will develop for inertia-free particles is valid for $\tau \leq 10^{-3}$. In order to ensure this hypothesis, we consider particles such that $\tau < 10^{-4}$ throughout the present study.

According to equation (3.18), in 2D, the two components of the particle velocity are thus:

$$V_p^x = V_f^x = \frac{dX_p}{dt} \quad \text{and} \quad V_p^z = V_f^z + \frac{2}{9}\frac{a^2(1-k)g}{\nu} = \frac{dZ_p}{dt} \tag{3.19}$$

where X_p and Z_p are the particle coordinates. This equation shows that neutrally buoyant inertia-free particles ($k = 1$ and $\tau \to 0$) follow exactly the flow streamlines. For heavy particles (denser than the fluid such as $k > 1$), we have $V_p^z < V_f^z$, and for particles lighter than the fluid such as $k < 1$, we have $V_p^z > V_f^z$. For the general case, the trajectory of the particle is then defined by:

$$\frac{dZ_p}{dX_p} = \frac{dZ_p}{dt}\frac{dt}{dX_p} = \frac{V_f^z + \frac{2}{9}\frac{a^2(1-k)g}{\nu}}{V_f^x} \tag{3.20}$$

The total length of the fracture L_∞ is selected as a horizontal length scale. The following dimensionless parameters are introduced:

$h^* = \frac{H_0}{L_\infty}$, $x = \frac{X}{L_\infty}$, $z = \frac{Z}{H_0}$, $v_f^x = \frac{V_f^x}{V_0}$ and $v_f^z = \frac{1}{h^*}\frac{V_f^z}{V_0}$.

Equation (3.20) can then be rewritten in the dimensionless form:

$$\frac{dz_p}{dx_p} = \frac{dz_p}{dt}\frac{dt}{dx_p} = \frac{v_f^z - \dfrac{W}{h^*}}{v_f^x} \tag{3.21}$$

with $W = \dfrac{2}{9}\dfrac{a^2(k-1)g}{\nu V_0}$ a dimensionless number that represents the ratio between the particle sedimentation Stokes velocity and the flow mean velocity V_0.

Knowing the particle initial position (x_p^0, z_p^0), and knowing the components of the fluid velocity (v_f^x and v_f^z) at each point (x, z) of the flow domain, the integration of equation (3.21) gives the position of the particle. In the next section, $\vec{v_f}$ will be calculated for a closed channel flow, assuming that the flow follows the LCL.

Using equations (3.21) and (3.8), the trajectory of an inertia-free particle in a closed channel LCL flow can be defined by:

$$\frac{dz_p}{dx_p} = \frac{-4h(x)}{3(1-\eta^2)}\frac{W}{h^*} + (\phi'(x) + \eta h'(x)) \tag{3.22}$$

The trajectory of the particle thus depends on the channel geometrical parameters $h(x)$ and $\phi(x)$, and on the ratio $\dfrac{W}{h^*}$.

Equation (3.22) can then be exploited to determine particle trajectories in channels with flat and sinusoidal walls.

3.1.2.c. Channel with flat walls

We consider the simple case of a horizontal channel of total length L_∞ made up by two parallel flat walls. The aperture between the walls is H_0. In this case, $\phi_1(x) = -1/2$, $\phi_2(x) = 1/2$, $h(x) = 1/2$, $\phi(x) = 0$, $h'(x) = \phi'(x) = 0$, $\eta = 2z$, and equation (3.22) becomes:

$$\frac{dz_p}{dx_p} = \frac{-2}{3(1-4z^2)}\frac{W}{h^*} \tag{3.23}$$

Integrating equation (3.23) between the initial position of the particle (x_p^0, z_p^0) and its actual position (x_p, z_p), the equation of the particle trajectory in a channel with flat walls

can be expressed as:

$$3(z_p - z_p^0) - 4(z_p^3 - (z_p^0)^3) = 2\frac{W}{h^*}(x_p^0 - x_p) \tag{3.24}$$

In the case of a closed channel flow, equation (3.24) enables to predict the final position of a particle injected at a defined initial position inside the channel. More specifically, it allows to know if the particle will settle inside the channel or if it will be transported till the outlet. In fact, by replacing x_p by 1 (which corresponds to $X_p = L_\infty$) and by searching for the corresponding z_p, the particle will exit the channel if $z_p > -\frac{1}{2}$, it will settle inside if $z_p < -\frac{1}{2}$.

3.1.2.d. Channel with sinusoidal walls

For the case of a channel with sinusoidal walls, in the dimensional form, the walls are defined by:

$$\Phi_1(X) = \frac{H_0}{2} + A_1 Sin(\frac{2\pi}{L_0}(X - \frac{\Delta X}{2})) \quad \text{and} \quad \Phi_2(X) = \frac{H_0}{2} + A_2 Sin(\frac{2\pi}{L_0}(X + \frac{\Delta X}{2})) \tag{3.25}$$

where A_1 is the lower wall amplitude, A_2 is the upper wall amplitude, and ΔX is the horizontal shift between the two walls (Figure 1 in chapter 2). The dimensionless form of $\Phi_1(X)$ and $\Phi_2(X)$ are given in chapter 2 (equation (2.1)). In this case, the expressions of the dimensionless local aperture $h(x)$ and channel middle line $\phi(x)$ and their derivatives are more complex so an equation in the form of equation (3.24) is difficult to obtain analytically. Nonetheless, it is possible to find the position of a particle by numerically integrating equation (3.20) over $[x_p^0, 1]$ considering $z(x_p^0) = z_p^0$ as the initial condition. For the simple case of channels having two parallel walls, making the substitution $z^*(x) = z(x) - \phi(x)$ leads to an equation relating $z^*(x)$ and x similar to equation (3.24). Therefore, the behavior of particles transported in corrugated channels with parallel walls is identical to the one occurring in channels with parallel walls, when studied with the channel middle line as reference.

3.2 Numerical verification

In this section, we verify equations (3.22) and (3.24) by performing numerical simulations. These equations were developed under the assumption that particle inertia can be neglected (equation (3.18)) and the flow velocity components were calculated using the LCL which assumes that the flow is dominated by viscous forces. The numerical simulations presented here aim to challenge the validity of these assumptions and to verify equations (3.22) and (3.24) by taking into account particle inertia and by fully resolving the continuity and the NS equations governing the fluid flow inside the channel.

The algorithm of the numerical simulations is shown in Figure 3.2. The finite element

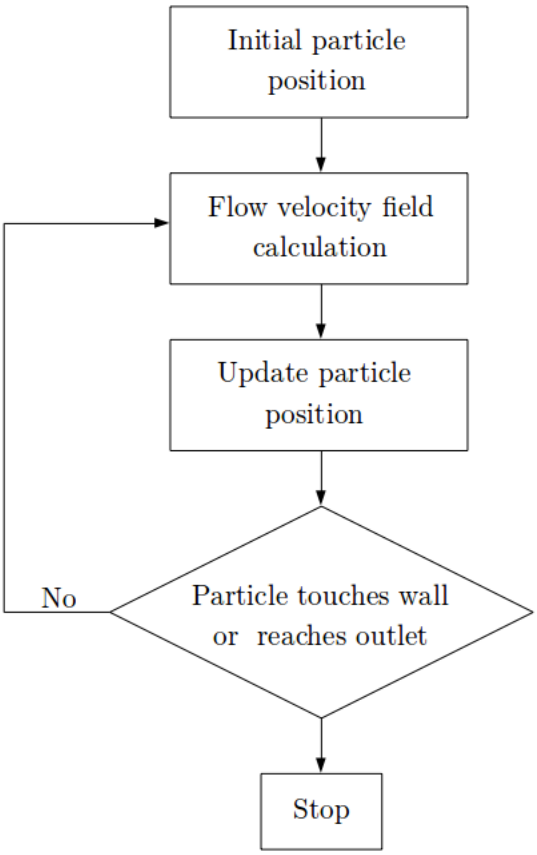

Figure 3.2: The algorithm used in the numerical simulations.

method (FEM) is used to solve the flow equations (cf. chapter 2) and a Lagrangian particle tracking technique is used to simulate particles motion in the flow by integrating equation (3.7). For each particle, an ordinary differential equation (ODE) is solved for each position

vector component (2 equations are solved in 2D) using a fourth order Runge-Kutta method with an adaptive time step. At each time step, the forces acting on each particle are obtained from the calculated fields at the current particle position. The positions of the particles are then updated. This process is repeated until the preset simulation time is reached or when the particle comes in contact with a boundary.

The ODE considered in the simulations is equation (3.7). It corresponds to equation (3.7), with Faxen corrections and Basset history force neglected under the assumptions that particle size is small compared to the channel aperture and that the disturbance flow due to the particle is quasi-steady.

3.2.1 Simulation procedure

The geometry of the channel is first defined. In the case of a channel with flat walls, it is represented by a horizontal rectangle defined by the channel aperture as its width and the channel total length as its length. In the case of a channel with sinusoidal walls, the two walls are constructed according to the expressions of $\Phi_1(X)$ and $\Phi_2(X)$ (cf. Chapter 2, equation (2.1)). The channel is then built by defining its mean aperture and the horizontal shift. The channel inlet consists of a square part to ensure a parabolic velocity profile.

The computational domain is discretized with a triangular mesh (Figure (3.3)). The mesh is refined in the near wall regions and gradually coarsened when moving towards the channel center. A preliminary grid independence test has been performed to determine the optimal number of elements with regards to computational cost and numerical precision. On a total meshed area of 0.0049 m^2, the average element surface area is 0.0192 mm^2. The mesh chosen for this case consists of 252364 elements.

A parabolic velocity profile with a mean flow velocity V_0 is defined at the inlet, a zero pressure is imposed at the outlet $P_{outlet} = 0$ (Figure (3.3)), and no-slip boundary conditions are imposed on the channel walls ($\vec{V_f} = \vec{0}$).

The continuity and NS equations governing the steady incompressible flow in the channel are solved, and the pressure and velocity fields are computed.

The properties of the particles (density ρ_p and radius a) and their number are determined based on the value of W (see section 3.2.2). The particles are then released with zero initial

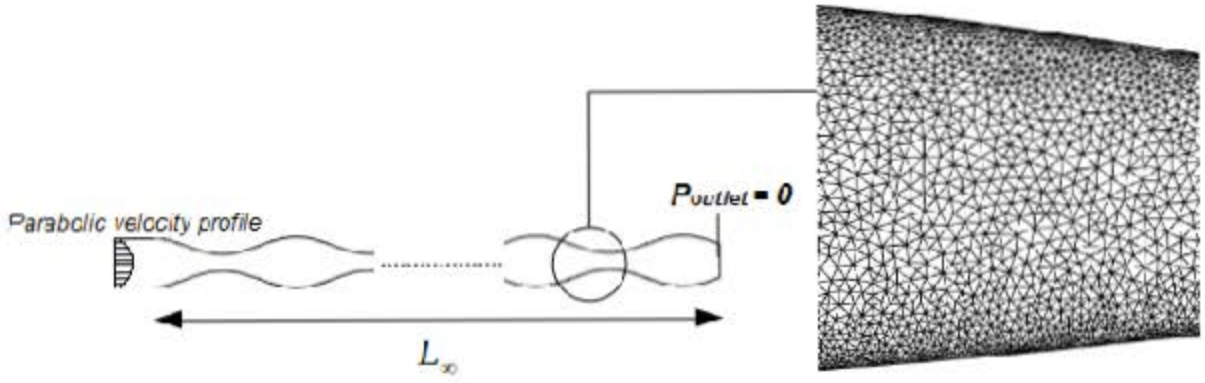

Figure 3.3: Boundary conditions applied on a channel with sinusoidal walls (left) and the triangular mesh used in the numerical simulations (right).

velocity at $X = 0$ and at different vertical positions.

The last step of the simulation consists in calculating the particle trajectories by solving the equation of motion for each particle (equation (3.7)). When a particle comes in contact with a wall, it sticks to it and it is considered as deposited. The calculation of its trajectory is then terminated.

3.2.2 Results

Before validating the analytical model (equations (3.22) and (3.24) for $\tau < 10^{-4}$, numerical simulations were performed for $\tau = 0.01$ to verify the presence of inertial focusing as predicted by equation (3.17). The aim of these first simulations is to check the ability of the numerical method that we used to verify analytical models and more particularly to take into account particle inertia. In fact, the focusing in this case is only due to inertia. Therefore, if the numerical simulations can capture the focusing effect then particle inertia is indeed taken into account.

3.2.2.a. Particle focusing

A first numerical simulation was performed under the following conditions: 10 particles are injected at different initial vertical positions in a mirror-symmetrical channel with $H_0 = 0.3mm$, $\epsilon = 0.1$, and $\delta_0 = 0.25$. The particle properties and the flow characteristics are set to ensure that $\tau = 0.01$ and that equation (3.17) is resolved so that an attracting streamline is

expected to appear in the flow. The variation of the particle vertical positions with respect to time is plotted in Figure 3.4.

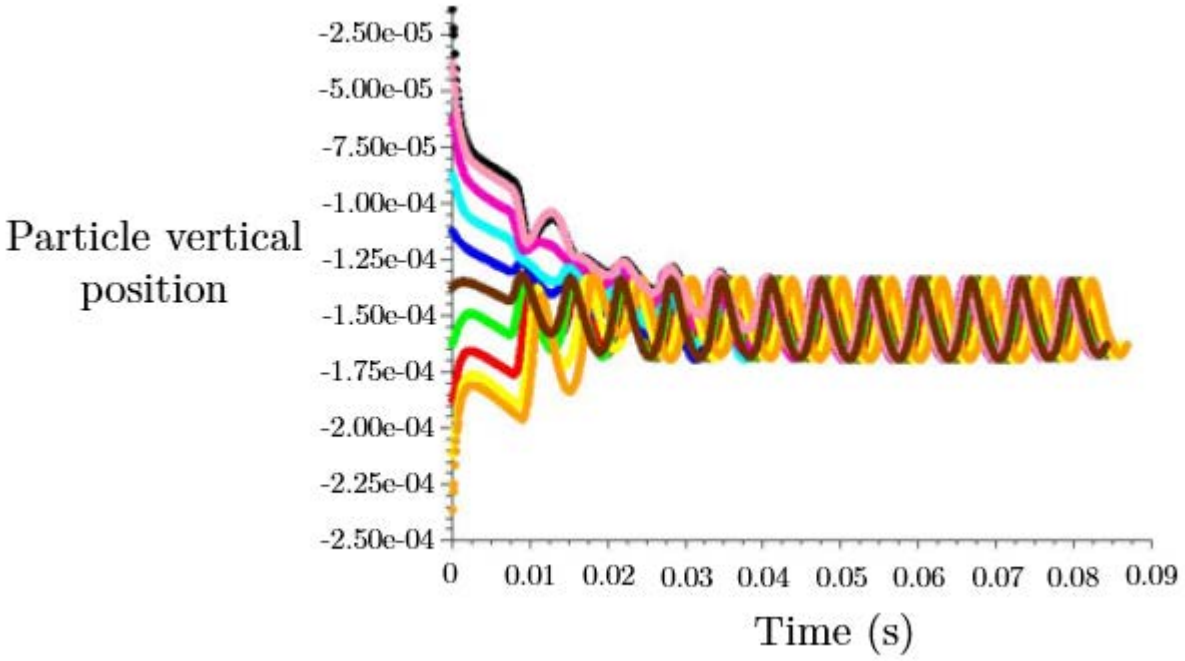

Figure 3.4: Evolution of the vertical position of 10 particles initially located at different heights in a sinusoidal channel for $\tau = 0.01$ as predicted by FEM numerical simulations.

It is clear that particles tend to follow the same trajectory after a certain distance and that particle focusing indeed occurred inside the channel. This result confirms that equation (3.17) is valid and that particle inertia is indeed taken into account in its formulation.

3.2.2.b. Particle trajectories

In this section, particle trajectories are calculated such ensuring that $\tau < 10^{-4}$.

i. Channel with flat walls

To verify equation (3.24), we computed numerically the trajectories of particles in a channel with flat walls considering the full equation (equation (3.7)). We set up a numerical experiment with a channel of total length $L_\infty = 1\,m$ and of aperture $H_0 = 5\,mm$. 5 particles of radius $a = 5\,\mu m$ and density ratio $k = 2.5$ are injected in the channel at the same initial horizontal position x_p^0 but at different initial vertical positions z_p^0. The fluid used is

water and the mean flow velocity V_0 fixed equal to $0.01\,m/s$. In this case $W = 0.00817$ and $\tau = 1.66 * 10^{-7}$. The final distance x_p^f traveled by each particle until they come in contact with the bottom wall was calculated for each particle initial vertical position z_p^0 and comparisons were made with respect to the predictions of equation (3.24). As shown in Figure (3.5), the two approaches are in very good agreement with a maximum relative error between the predicted final particle positions equal to $0.2\,\%$.

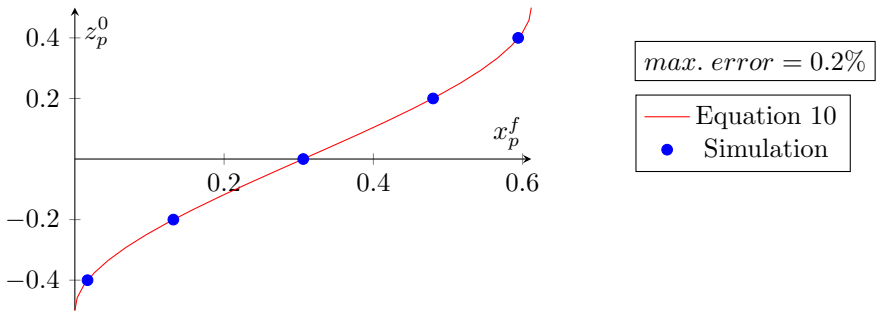

Figure 3.5: Distances x_p^f traveled by particles with different initial vertical positions z_p^0 in a channel with flat walls such as $W = 0.00817$ and $\tau = 1.66 * 10^{-7}$. Comparison between equation (3.24) (solid line) and particle tracking numerical simulations (symbols).

ii. Channel with corrugated walls

To verify equation (3.22) for the case of corrugated channels, we considered a channel made up by two sinusoidal walls with $H_0 = 5mm$, $L_0 = 5\,cm$, $L_\infty = 0.98\,m$, $A_1 = 1.5\,mm$, $A_2 = 2\,mm$, and $\Delta X = 0.25\,L_0$. This configuration corresponds to a general case of a random geometry because the channel walls are neither identical nor parallel. The particle properties and initial positions were chosen equal to the ones used in the previous section (case of channel with flat walls) and the flow mean velocity was also fixed equal to $V_0 = 0.01\,m/s$. In this case $W = 0.00817$ and $\tau = 3.33 * 10^{-6}$. The distances x_p^f traveled by the particles for different initial vertical positions z_p^0 are plotted in Figure (3.6), considering the solutions predicted by equation (3.22) and by the numerical model. The two approaches are here again in good agreement with a maximum relative error of about 3.3 % between their respective predictions. The origin of this relative error is further investigated in section 3.2.2.d.

To further compare the two approaches, the trajectories predicted by the analytical model or the numerical model for the particle with $z_p^0 = -0.2$ are plotted in Figure 3.7. One can see

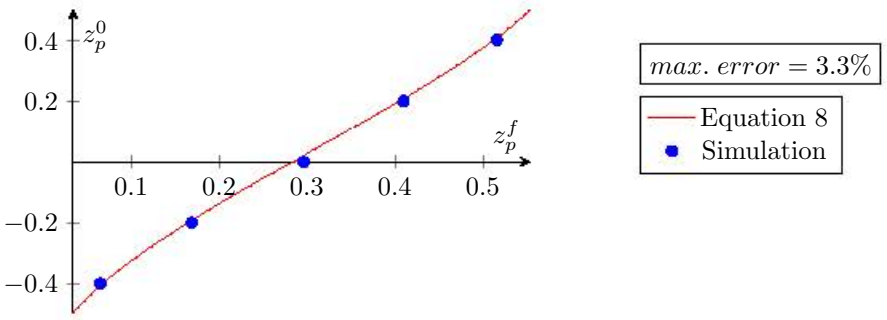

Figure 3.6: Distances x_p^f traveled by particles with different initial vertical position z_p^0 in a corrugated channel such as $W = 0.00817$ and $\tau = 3.33 * 10^{-6}$. Comparison between equation (3.22) (solid line) and particle tracking numerical simulations (symbols).

that the trajectories are quasi-identical and have exactly the same corrugated shape, which further demonstrates the validity of the proposed analytical approach.

Figure 3.7: Comparison between particle trajectories in the same channel as found in the numerical simulation and as predicted by the analytical model

iii. Dependence of the particle trajectory on W

In the two previous sections, we verified the particle trajectory equations in channels with flat and corrugated walls for specific geometries. However, according to equation (3.22), the trajectory depends on the geometry of the channel ($\phi'(x)$ and $h'(x)$) and on the ratio $\frac{W}{h^*}$. For a specified channel geometry (h^* is constant), W is the only dimensionless parameter affecting particle trajectories. More precisely, if, in the same channel, two particles with different properties are injected in flows with different characteristics (velocity, viscosity), the particles should follow the same trajectory if they present the same dimensionless number W.

In order to verify the dependency of particle trajectories on W, we conducted a sensitivity analysis. To do so, we first studied 5 cases (cases 1 to 5 in Table (3.1)) in which the particle properties and fluid mean velocities were different but W was kept quasi constant (≈ 0.0043).

For each case, 8 particles were injected in the channel at different initial vertical positions z_p^0. The distances x_p^f traveled by the particles are plotted in Figure (3.8) as a function of their initial positions for different initial vertical positions. The maximum relative error between the numerical and the analytical solutions of the distances traveled by the particles is 5.1 %. To sum up, particles injected at the same initial altitude travel approximately the same distance before sedimentation if W is kept constant.

Parameter	W	τ	ϵRe_H	$a(\mu m)$	k	$V_0(m/s)$
case 1	0.0043	$4.26 * 10^{-7}$	2.5	2.5	2.58	0.005
case 2	0.00429	$1.89 * 10^{-6}$	4	5	1.63	0.008
case 3	0.00431	$1.55 * 10^{-7}$	1	3	1.44	0.002
case 4	0.00429	$4.62 * 10^{-6}$	5	7.5	1.35	0.01
case 5	0.00432	$1.8 * 10^{-5}$	10	10.5	1.36	0.02
case 6	0.00809	$5.35 * 10^{-7}$	1.5	4.5	1.55	0.003
case 7	0.00809	$9.45 * 10^{-7}$	2.5	4	2.16	0.005
case 8	0.00809	$6.97 * 10^{-6}$	3.75	11	1.23	0.0075
case 9	0.00809	$7.07 * 10^{-6}$	7.5	8	1.87	0.015
case 10	0.00809	$1.47 * 10^{-5}$	10	7	2.59	0.021

Table 3.1: Flow characteristics and particles properties used in the simulation to ensure $W \simeq 0.0043$ (cases 1 to 5) and $W \simeq 0.00809$ (cases 6 to 10).

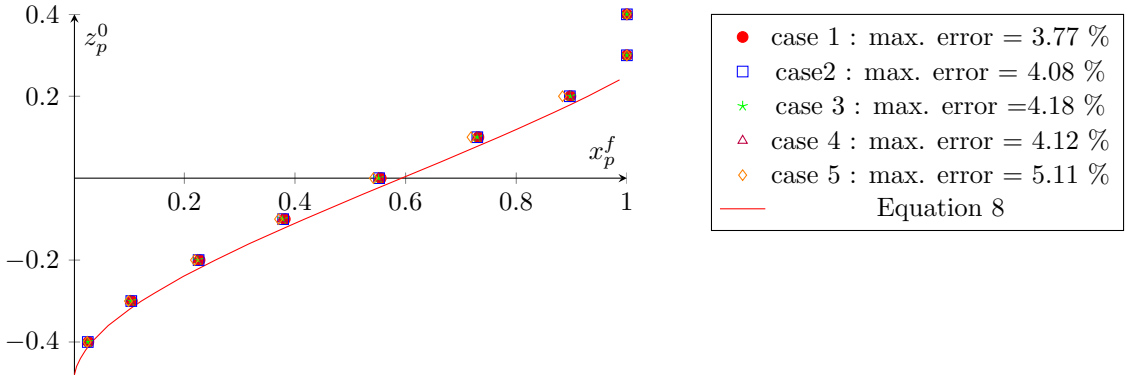

Figure 3.8: Distances x_p^f traveled by particles with different initial positions z_p^0 for different configurations presenting same $W \simeq 0.004$. Comparison between equation (3.22) (solid line) and particle tracking numerical simulations (symbols).

To further verify this dependency on W, 5 additional cases (cases 6 to 10 in Table 3.1) were tested for a value of $W \approx 0.0081$. The results of this second series of tests are plotted in Figure (3.9). Here again, the dependency of particle trajectory on W in the non inertial

regime is verified, validating furthermore its ability for determining the behavior of particles immersed in channel flows.

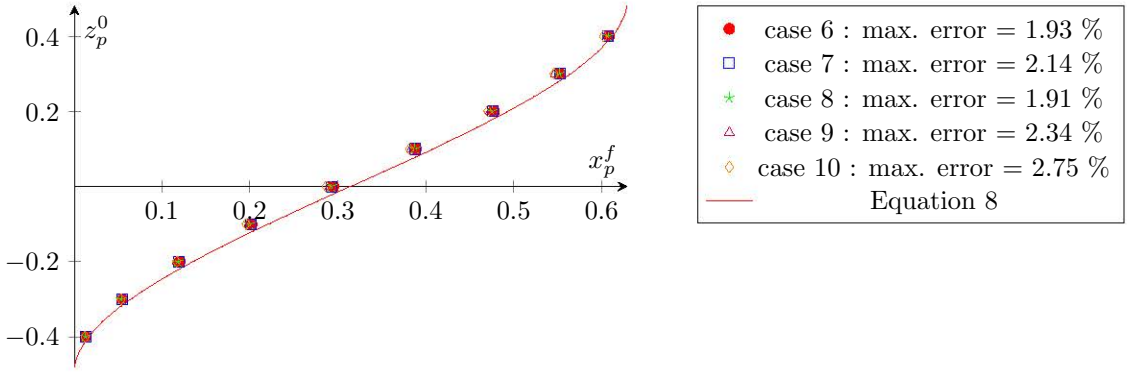

Figure 3.9: Distances x_p^f traveled by particles with different initial positions z_p^0 for different configurations presenting same $W \simeq 0.0081$. Comparison between equation (3.22) (solid line) and particle tracking numerical simulations (symbols).

iv. Relative error between the numerical and analytical solutions

The error between the numerical and the analytical solutions can be due to: (i) errors in the numerical simulations, (ii) the assumptions under which the analytical model was developed such as the use of the LCL as a solution of the NS equations or, (iii) the negligence of particle inertia. To investigate the origin of this error, the numerical solution obtained for case 5, where the maximum relative error is equal to 5.11 %, was recalculated 4 times under different conditions. The outcomes of this series of tests are as follows:

- When the mesh size is reduced by half, the maximum relative error remains equal to 5.11 %.
- When the time step used to update the particle position is reduced by a factor of 2, the maximum relative error remains equal to 5.11 %.
- When the particle inertia is neglected, the maximum relative error decreases slightly to 5 %.
- When Stokes equation is solved instead of the NS equations (to neglect fluid inertia), the maximum relative error decreases to 4.08 %.

Taking into account these results, it is clear that the numerical errors are limited since the relative error between the two solutions remains similar whatever the mesh or time step refinement. On the other hand, neglecting particle and fluid inertia seems to reduce the relative error between the two approaches. We can certainly argue that the error is due to the use of the LCL in equation (3.22) as it cannot ensure a perfect representation of the velocity field. Nonetheless, The error is expected to remain limited if ϵ and Re are small (cf. chapter 2)

3.3 Particle transport regime diagrams

As illustrated in the previous section, the trajectories of small particles with very low inertia, in channel flows satisfying the LCL approximation, depend on the channel geometry and on the dimensionless number W. In this section, we try to characterize the different transport regimes of these particles. To do so, we assume a uniform distribution of the particles at the inlet, and we define three arbitrary regimes that can occur based on the amount of particles that settle inside the channel:

- **Transport**: at least 75 % of the particles are transported in the channel till the outlet. All the particles having an initial vertical position $z_p^0 \in [-1/4, 1/2[$ are transported till the outlet of the channel, and particles with $z_p^0 \; \epsilon \;]-1/2, -1/4]$ settle inside the channel.

- **Sedimentation**: at least 75 % of the particles settle inside the channel. Particles with $z_p^0 \in]1/4, 1/2[$ exit the channel, and the ones with $z_p^0 \in]-1/2, 1/4]$ settle inside the channel.

- **Transition**: less than 75 % but more than 25 % of the particles exit the channel. This regime describes the transition between the transport and the sedimentation regimes described previously.

The arbitrary selection of the separating percentages 25 % and 75 % defining the different regimes will be discussed later on. The dependence of these regimes on W is studied first in

a channel with flat walls, and then in corrugated channels presenting different geometrical properties (wavelength, amplitude, horizontal shift between the walls).

3.3.1 Channel with flat walls

The channel geometry is defined by the dimensionless parameter $h^* = \frac{H_0}{L_\infty}$. Based on equation (3.24), the three arbitrary regimes defined previously correspond respectively to different values of $\frac{W}{h^*}$:

- Transport: $\frac{W}{h^*} < 0.156 = \frac{W_{cr1}}{h^*}$
- Sedimentation: $\frac{W}{h^*} > 0.84 = \frac{W_{cr2}}{h^*}$
- Transition: $0.156 < \frac{W}{h^*} < 0.84$

where W_{cr1} and W_{cr2} are critical values of W characterizing the transition between the respective regimes. W_{cr1} and W_{cr2} vary linearly as a function of h^*. Diagrams of transport regimes can thus be established for channels with flat walls. In Figure (3.10) (a), a 2D diagram is built where three different regimes corresponding to the transport, transition and sedimentation zones are delimited by the linear variation of W_{cr1} and W_{cr2} as functions of h^*. In Figure (3.10) (b), a 1D diagram is built where these zones are presented according to the single parameter $\frac{W}{h^*}$. Although the 1D representation could be considered more relevant in terms of delimitation of the three zones than the 2D one, it does not reflect clearly the respective contribution of parameters W and h* on the variation of the zones in the diagram. Consequently, we keep the 2D representation along the chapter as it gives a better graphical representation of the effects of either the channel geometry (h*) or the particle and flow properties (W) on the transport regimes. This will enable us to highlight the effects of the geometrical parameters of the channel on the variation of the different zones in the diagram. Similar diagrams will be plotted subsequently to highlight the effect of the channel geometrical parameters on the transport regimes.

The particle transport regimes were arbitrarily defined so that the diagram depends on the percentages of particles that can be transported or deposited inside the channel. When

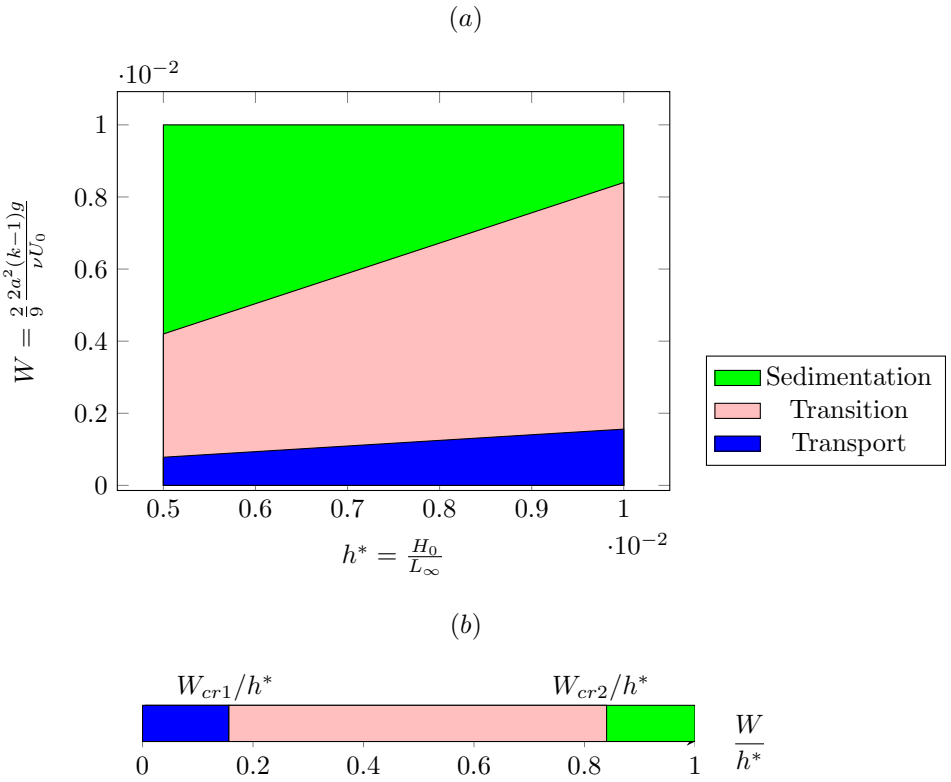

Figure 3.10: Transport regimes diagram for weakly inertial particles in a closed channel with flat walls. (a) 2D representation of the different zones according to the variation of W as a function of h^*. (b) 1D representation of these zones according to $\dfrac{W}{h^*}$.

changing these percentages, the variation of W_{cr1} and W_{cr2} as functions of h^* remains constant so that the regimes diagram keeps the same form but the transport and sedimentation zones will be wider or narrower. The variation of the ratios W_{cr_1}/h^* and W_{cr_2}/h^* as functions of the percentages of particles transported or sedimented is plotted in Figure (3.11).

The critical ratio W_{cr_2}/h^* tends to increase when the arbitrary sedimentation regime corresponds to a higher fraction of transported particles. Inversely, W_{cr_1}/h^* tends to decrease when the fraction of transported particles is bigger.

To verify numerically the regime diagram obtained for channels with flat walls, a numerical experiment was conducted using the particle tracking technique presented in section 3.2, consisting this time in injecting 100 particles at the channel inlet for three different values of the pair (h^*, W). These three values correspond respectively to configurations located in the transport ($h^* = 0.008$, $W = 0.001$), transition ($h^* = 0.008$, $W = 0.007$), and sedimentation ($h^* = 0.008$, $W = 0.007$) zones presented in Figure (3.10). For each case, the number of

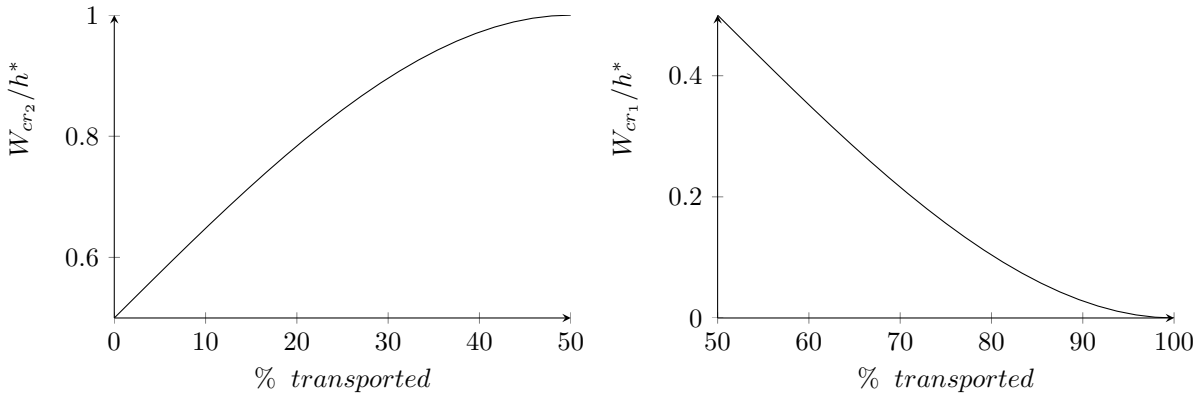

Figure 3.11: Variation of W_{cr_1}/h^* and W_{cr_2}/h^* as a function of the percentage of particles transported inside the channel.

particles deposited inside the channel corresponds to the percentage of sedimented particles.

		% of sedimented particles	
(h^*, W)	$\frac{W}{h^*}$	Numerical experiment	Diagram prediction
$(0.008, 0.001)$	0.125	21	< 25 (Transport)
$(0.008, 0.0035)$	0.437	43	ϵ $[25, 75]$ (Transition)
$(0.008, 0.0075)$	0.937	80	> 75 (Sedimentation)

Table 3.2: Percentages of sedimented particles in a channel with flat walls for configurations corresponding respectively to the transport regime ($h^* = 0.008$, $W = 0.001$), the transition regime ($h^* = 0.008$, $W = 0.0035$), and the sedimentation regime ($h^* = 0.008$, $W = 0.0075$) presented in Figure (3.10). Comparison between the regime diagram predictions (Figure 3.10) and particle tracking numerical simulations results.

As illustrated in Table (3.2), the percentages of sedimented particles obtained numerically for each case are in good agreement with the regimes predicted by the regime diagram and thus confirms the validity of the proposed approach.

3.3.2 Corrugated channel with sinusoidal walls

The channel is here defined by the following dimensionless parameters: the average corrugation amplitude $\delta_0 = \frac{A_0}{H_0} = \frac{A_1+A_2}{2H_0}$, the phase shift $\alpha = \frac{2\pi\Delta X}{L_0}$, the asymmetry between the wall corrugations $\gamma = \frac{A_2-A_1}{A_1+A_2}$ and $l^* = \frac{L_0}{L_\infty}$. In this case, $h^* = \epsilon l^*$.

The study for this type of channel is slightly more complex than for channels with flat walls because three additional geometrical parameters need to be taken into account (δ_0, α, γ). To do so, we first rewrote equation (3.22) as a function of these parameters. Then, we

applied the criteria defining the three transport regimes using this equation. The strategy consists in varying one parameters while keeping the other two constant so that its influence on the regime diagram can be assessed.

The main emerging result is that, whatever the walls amplitudes and horizontal shift are, the variations of W_{cr1} and W_{cr2} as functions of h^* remain linear. Therefore, even for channels with sinusoidal walls, the diagram is similar to the one obtained for channels with flat walls (Figure (3.10)). The difference lies in the extension or reduction of the transport and sedimentation zones depending on the channel geometry. In order to assess the influence of the channel geometry on the regime diagram, we studied three main configurations:

- channel having in phase walls ($\alpha = 0$, $\gamma \neq 0$)
- channel having out of phase identical walls ($\alpha \neq 0$, $\gamma = 0$)
- channel having walls with maximum phase lag ($\alpha = \pi$, $\gamma \neq 0$)

3.3.2.a. Channel with in phase walls

In this case, there is no horizontal shift ΔX between the two walls and $\alpha = 0$. The two walls do not have necessarily the same amplitude (Figure (3.12)).

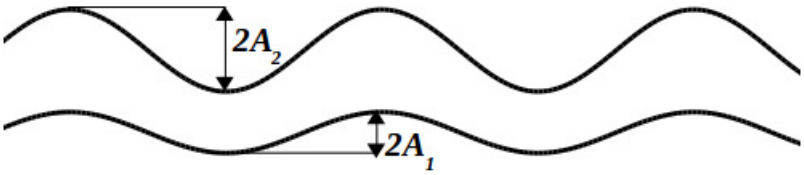

Figure 3.12: Channel with in phase sinusoidal walls. Here, the upper wall is more corrugated than the lower wall meaning that $\gamma \neq 0$.

By varying the amplitudes of the walls A_1 and A_2, the corrugations wavelength L_0 and the channel aperture H_0, we find that in all cases, $W_{cr1} = 0.156h^*$ and $W_{cr2} = 0.84h^*$. These values are identical to the ones obtained in section 3.3.1. Consequently, the diagram obtained for channels with flat walls (Figure (3.10)) can also be used to characterize transport regimes in corrugated channels without horizontal shift between the walls. To verify this hypothesis, the numerical experiments presented in section 3.3.1 were conducted in a

channel with sinusoidal in phase walls using the same values of (h^*, W). The percentages of sedimented particles obtained numerically are summarized in Table (3.3).

		% of sedimented particles	
(h^*, W)	$\frac{W}{h^*}$	Numerical experiment	Diagram prediction
$(0.008, 0.001)$	0.125	22	< 25 (Transport)
$(0.008, 0.0035)$	0.437	44	ϵ $[25, 75]$ (Transition)
$(0.008, 0.0075)$	0.937	79	> 75 (Sedimentation)

Table 3.3: Percentages of sedimented particles in a sinusoidal channel with in phase walls for configurations corresponding respectively to the transport regime ($h^* = 0.008$, $W = 0.001$), the transition regime ($h^* = 0.008$, $W = 0.0035$), and the sedimentation regime ($h^* = 0.008$, $W = 0.0075$) presented in Figure (3.10). Comparison between the regime diagram predictions (Figure 3.10) and particle tracking numerical simulations results.

Again, the percentages of sedimented particles agree well with the predictions of the regime diagram, confirming therefore the validity of the regime diagram for corrugated channels with in phase walls. Interestingly, the diagram is identical to the one obtained for channels with flat walls.

3.3.2.b. Channel with out of phase identical walls

In this case, the two walls are identical, i.e. they have the same corrugation amplitude $A_1 = A_2$ and thus $\gamma = 0$. α and δ_0 can vary respectively such as:

- δ_0 will be modified by changing the walls amplitude and/or the channel mean aperture.
- α will be modified by changing the phase lag between the upper wall and the lower wall. $\alpha = 0$ corresponds to channels with parallel walls and $\alpha = \pi$ corresponds to channels with mirror-symmetrical walls

i. Influence of δ_0

Let's consider $W_{cr1} = c_1 h^*$ and $W_{cr2} = c_2 h^*$ with c_1 and c_2 two constants describing their linear variation. The variations of c_1 and c_2 as functions of δ_0 are plotted in Figure (3.13). When δ_0 increases, c_1 increases as well, which means that the transport zone increases. Conversely, c_2 decreases when δ_0 increases, leading to a decrease of the sedimentation zone.

To further illustrate these variations, we compared two different cases considering δ_0 equal respectively to 0.1 and 0.4 while keeping $\alpha = \pi$ constant and plotted the associated

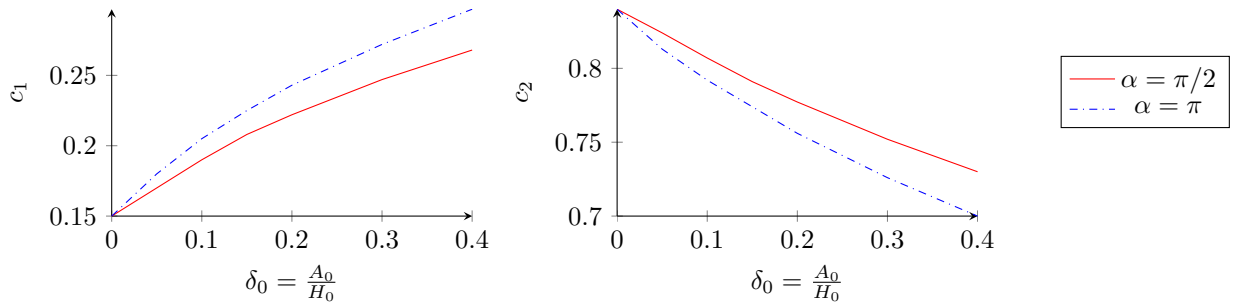

Figure 3.13: Variation of c_1 (left) and c_2 (right) as a function of δ_0 for two cases: $\alpha = \pi/2$ and $\alpha = \pi$.

regimes on the same diagram (Figure (3.14)). One can see that increasing the corrugation amplitude (by increasing δ_0) leads to an increase of both the transport and sedimentation zones.

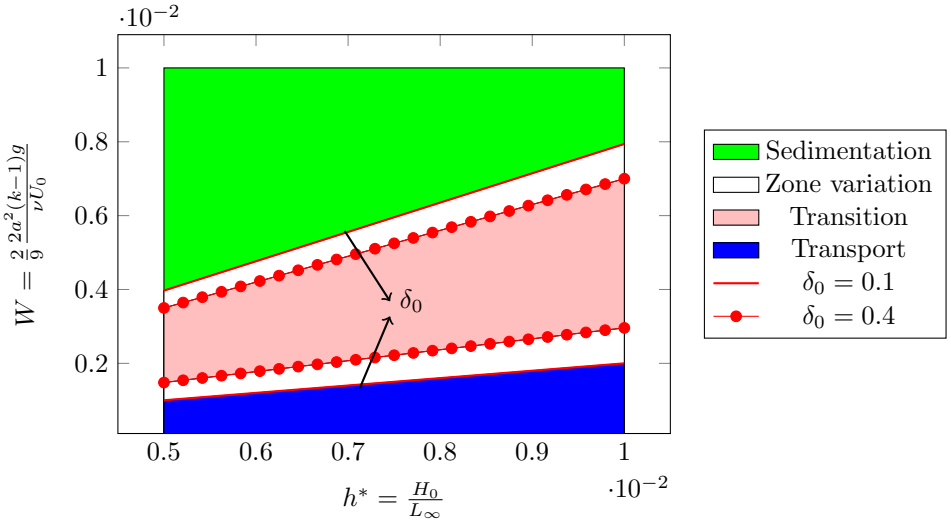

Figure 3.14: Effect of increasing the dimensionless corrugation amplitude δ_0 on particle transport regimes for channels having out of phase identical walls. The red solid lines present the limits between the regimes for a channel with $\delta_0 = 0.1$ and the red dotted lines present the limits between the regimes after increasing the walls corrugations ($\delta_0 = 0.4$). The white zones present the variations in the transport and sedimentation zones respectively.

Here again, numerical experiments were conducted to verify the diagram's predictions. Two configurations corresponding to two pairs of (h^*, W) located respectively in the two variation zones of the diagram were used considering $\delta_0 = 0.1$ and $\delta_0 = 0.4$. The results are summarized in Table (3.4).

For ($h^* = 0.01$, $W = 0.0021$), when $\delta_0 = 0.1$, the percentage of the deposited particles is

			% of sedimented particles	
(h^*, W)	$\frac{W}{h^*}$	δ_0	Numerical experiment	Diagram prediction
$(0.01, 0.0021)$	0.21	0.1	30	ϵ [25, 75] (Transition)
		0.4	10	< 25 (Transport)
$(0.01, 0.0074)$	0.74	0.1	70	ϵ [25, 75] (Transition)
		0.4	80	> 75 (Sedimentation)

Table 3.4: Percentages of sedimented particles in sinusoidal channels with out of phase identical walls defined respectively by $\delta_0 = 0.1$ and $\delta_0 = 0.4$, for two configurations corresponding to ($h^* = 0.01$, $W = 0.0021$) and ($h^* = 0.01$, $W = 0.0074$). Comparison between the regime diagram predictions (Figure 3.14) and particle tracking numerical simulations results.

equal to 30 % (transition), while this percentage is equal to 10% when $\delta_0 = 0.4$ (transport). For ($h^* = 0.01$, $W = 0.0074$), when $\delta_0 = 0.1$, the percentage of the sedimented particles is equal to 70 % (transition), while this percentage is equal to 80% when $\delta_0 = 0.4$ (sedimentation). The numerical experiments confirm the effect of δ_0 on the regime diagram.

ii. Influence of α

To investigate the effect of the phase lag between the walls on particle transport, α was varied from 0 to 2π for two cases: $\delta_0 = 0.1$ and $\delta_0 = 0.2$. The variation of c_1 and c_2 as a function of α is plotted in Figure (3.15).

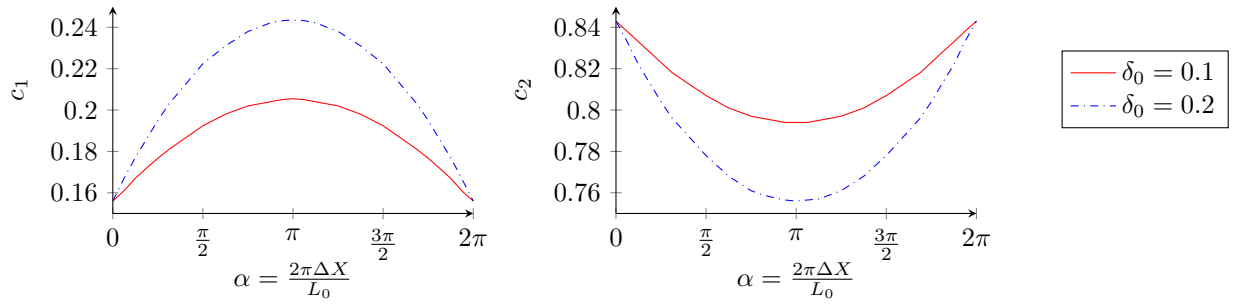

Figure 3.15: Variation of c_1 (left) and c_2 (right) as a function of α for two cases: $\delta = 0.1$ and $\delta = 0.2$.

Firstly, one can see that the behavior of the particles does not change when the phase lag between the walls is in the opposite direction ($\pm\,\alpha$). For example, if the lower wall is shifted from the upper wall by $\Delta X = L_0/4$ ($\alpha = \pi/2$), the particles settle at the same distance as if the shift was $\Delta X = -L_0/4$ ($\alpha = 3\pi/2$) (Figure (3.16)).

Secondly, c_1 reaches its maximal value when the phase lag between the walls is maximum

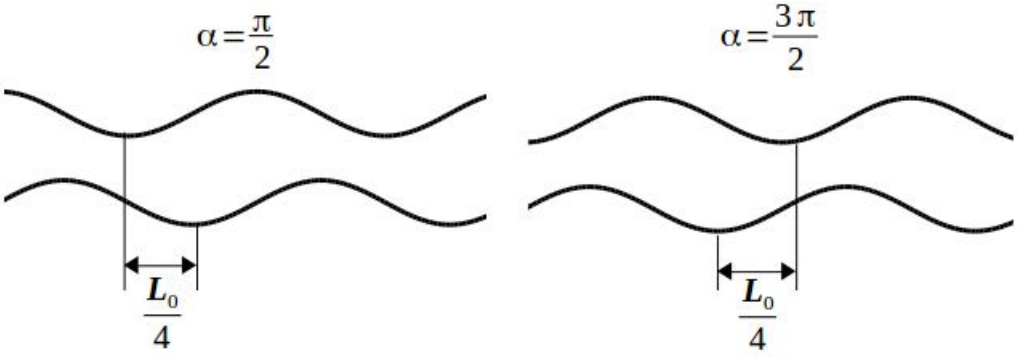

Figure 3.16: Channel with sinusoidal walls with positive horizontal shift $\alpha = \pi/2$ (left) and negative horizontal shift $\alpha = 3\pi/2$ (right).

($\alpha = \pi$). This means that the transport zone increases with the increase of the phase lag. Similarly, c_2 is minimum for $\alpha = \pi$ and therefore the sedimentation zone also increases when the phase lag increases.

To further illustrate these variations, we compared two different cases considering α equal respectively to 0 and π while keeping $\delta = 0.2$ constant (Figure (3.17)). One can see that increasing the phase lag between the walls leads to an increase of both the transport and sedimentation zones in the diagram, their maximum extents being reached when the channel walls are mirror symmetric ($\alpha = \pi$).

Here again, numerical experiments were conducted to verify the diagram's predictions. Two configurations corresponding to two pairs of (h^*, W) located respectively in the two variation zones of the diagram were used considering $\alpha = 0$ and $\alpha = \pi$. The results are summarized in Table (3.5).

			% of sedimented particles	
(h^*, W)	$\frac{W}{h^*}$	α	Numerical experiment	Diagram prediction
$(0.009, 0.0016)$	0.177	0	26	ϵ [25, 75] (Transition)
		π	20	< 25 (Transport)
$(0.0085, 0.0065)$	0.764	0	66	ϵ [25, 75] (Transition)
		π	80	> 75 (Sedimentation)

Table 3.5: Percentages of sedimented particles in sinusoidal channels with out of phase identical walls defined respectively by $\alpha = 0$ and $\alpha = \pi$, for two configurations corresponding to ($h^* = 0.009$, $W = 0.0016$) and ($h^* = 0.0085$, $W = 0.0065$). Comparison between the regime diagram predictions (Figure 3.17) and particle tracking numerical simulations results.

It is shown that for ($h^* = 0.009$, $W = 0.0016$), when $\alpha = 0$, the percentage of the

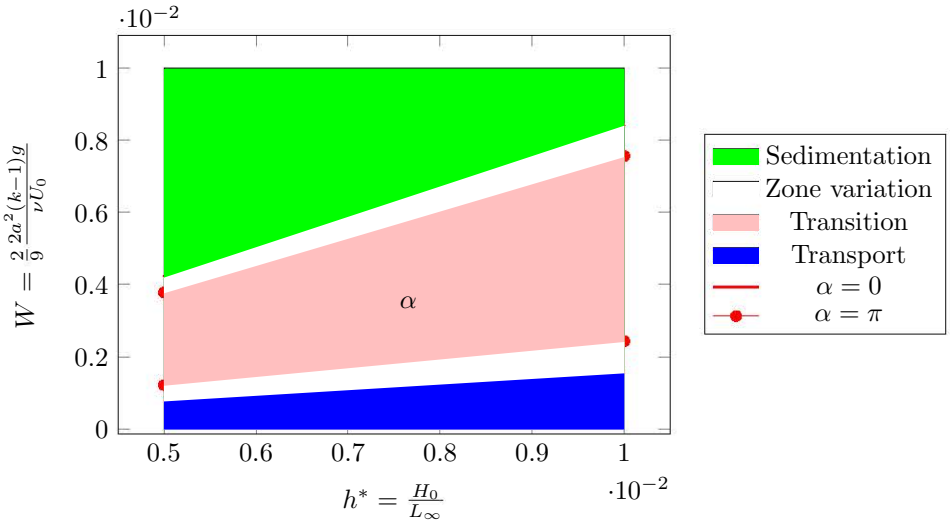

Figure 3.17: Effect of increasing α on particle transport regimes for channels having out of phase identical walls. The red solid lines present the limits between the regimes for a channel with $\alpha = 0$ and the red dotted lines present the limits between the regimes after increasing the phase lag to $\alpha_0 = \pi$. The white zones present the variations in the transport and sedimentation zones respectively.

deposited particles is equal to 26 % (transition), while this percentage is equal to 20% when $\alpha = \pi$ (transport). For ($h^* = 0.0085$, $W = 0.0065$), when $\alpha = 0$ the percentage of the sedimented particles is 66 % (transition), while this percentage is 80% when $\alpha = \pi$ (sedimentation). The effect of α on the regime diagram is again confirmed by the numerical experiment.

3.3.2.c. Channel with maximum phase lag between the walls

In this type of channel, the horizontal shift between the walls is maximum ($\Delta X = L_0/2$ or $\alpha = \pi$). When the two walls have the same corrugation amplitude ($\gamma = 0$), the channel presents a mirror-symmetrical geometry (Figure (3.18)). When the walls are not identical, γ varies between -1 when the upper wall is flat ($A_2 = 0$) and 1 when the lower wall is flat ($A_1 = 0$). $\gamma < 0$ means that the lower wall is more corrugated than the upper wall and vice versa.

To assess the influence of the corrugation amplitude asymmetry on particle transport, we studied the variation of c_1 and c_2 as a function of γ for two different average corrugation amplitudes $\delta_0 = 0.1$ and $\delta_0 = 0.2$ (Figure (3.19)).

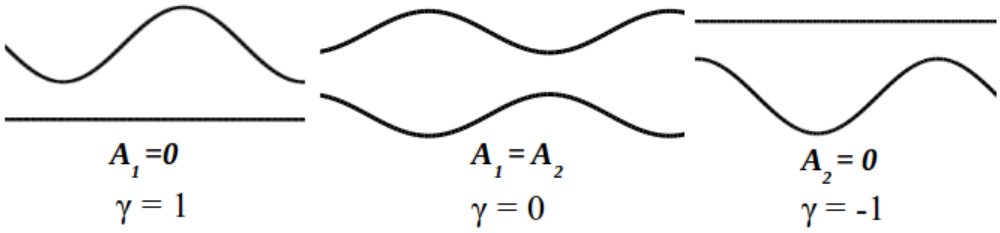

Figure 3.18: Channels with lower flat wall (left), mirror-symmetrical walls (center) and upper flat wall (right).

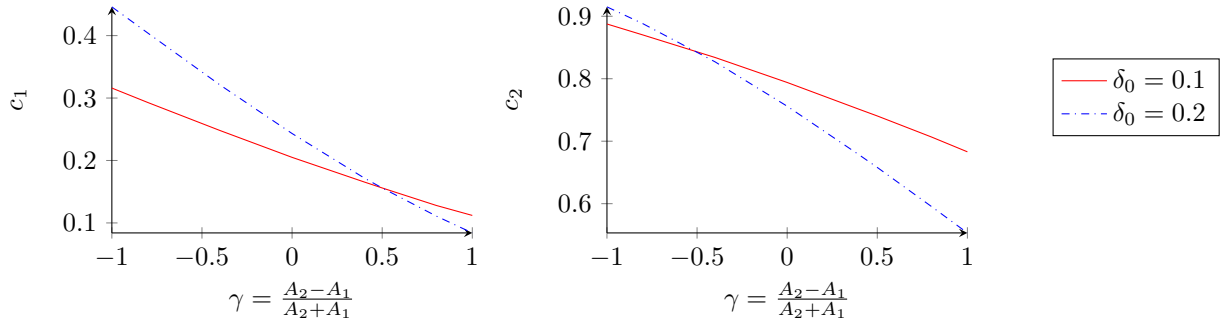

Figure 3.19: Variation of c_1 (left) and c_2 (right) as a function of γ for two different average corrugation amplitudes $\delta_0 = 0.1$ and $\delta_0 = 0.2$.

c_1 decreases when γ increases. It is maximal when the upper wall is flat ($\gamma = -1$) and minimal when the lower wall is flat ($\gamma = 1$). This means that the transport zone in the diagram is maximal when the upper wall is flat. The transport zone decreases when increasing the upper wall corrugation or decreasing the lower wall corrugation, to become minimal when the lower wall is flat. However, when $\gamma = 0.5$ (the upper wall corrugation is equal to three times the lower wall corrugation), the value of c_1 is the same for the two values of δ_0. Further calculations showed that for this case ($\gamma = 0.5$), c_1 is constant and independent of δ_0. When $\gamma < 0.5$, c_1 increases when δ_0 increases and, as a result, the transport zone increases. $\gamma > 0.5$ leads to the opposite result.

c_2 also decreases when γ increases. Similarly to what can be observed in the variation of c_1, when $\gamma = -0.5$ (the lower wall corrugation is equal to three times the upper wall corrugation), the value of c_2 is constant and independent of δ_0. When $\gamma < -0.5$, c_2 increases when δ_0 increases and, as a result, the sedimentation zone increases. The opposite result appears for $\gamma > -0.5$.

To further illustrate these variations, we compared two different cases considering the

γ equal respectively to 1 and -1 while keeping $\delta = 0.2$ constant (Figure (3.20)). For each case, the pair c_1, c_2 are respectively equal to 0.11, 0.68 and 0.31, 0.88. The analysis of this figure shows that increasing the upper wall corrugation relatively to the lower wall leads to a decrease of the transport zone and to an increase of the sedimentation zone.

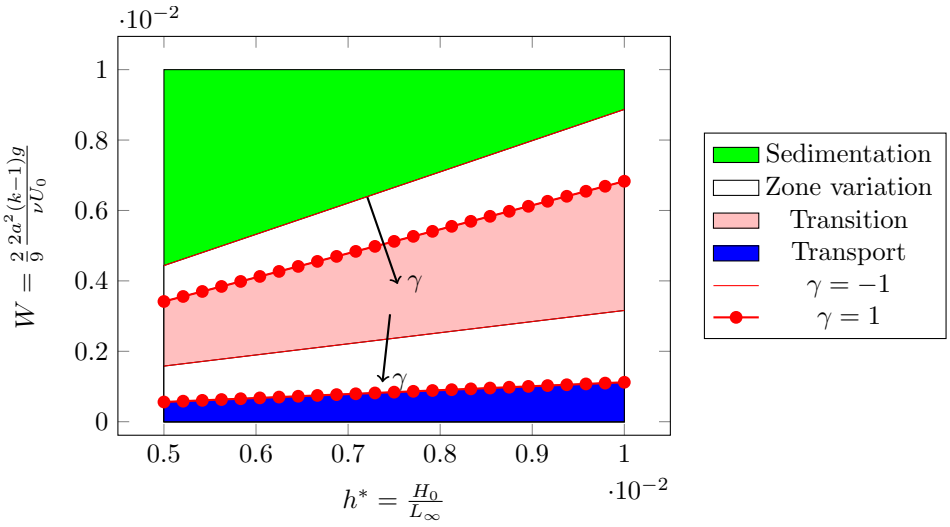

Figure 3.20: Effect of inverting the asymmetry of wall corrugations amplitudes γ on particle transport regimes. The red solid lines present the limits between the regimes for a channel with a flat upper wall ($\gamma = -1$) and the red dotted lines present the limits between the regimes for a channel with a flat lower wall ($\gamma = 1$). The white zones present the variations in the transport and sedimentation zones respectively.

Here again, we verified the predictions of the regime diagram against the numerical experiment performed using 100 particles. Two configurations corresponding to two pairs of (h^*, W) located respectively in the two variation zones of the diagram were used considering $\alpha = 0$ and $\alpha = \pi$. The results are summarized in Table 3.6.

			% of sedimented particles	
(h^*, W)	$\frac{W}{h^*}$	γ	Numerical experiment	Diagram prediction
$(0.01, 0.001)$	0.1	-1	0	< 25 (Transport)
		1	30	ϵ [25, 75] (Transition)
$(0.01, 0.0075)$	0.75	-1	53	ϵ [25, 75] (Transition)
		1	80	> 75 (Sedimentation)

Table 3.6: Percentages of sedimented particles in sinusoidal channels with out of phase identical walls defined respectively by $\gamma = -1$ and $\gamma = 1$, for two configurations corresponding to ($h^* = 0.01$, $W = 0.001$) and ($h^* = 0.01$, $W = 0.0075$). Comparison between the regime diagram predictions (Figure 3.20) and particle tracking numerical simulations results.

For ($h^* = 0.01$, $W = 0.001$), when $\gamma = -1$, no particles are deposited inside the channel (transport), while 30% of the particles are deposited when $\gamma = 1$ (transition). For ($h^* = 0.01$, $W = 0.0075$), when $\gamma = -1$, the percentage of the sedimented particles is equal to 53 % (transition), while this percentage is equal to 80% when $\gamma = 1$ (sedimentation). The effect of γ on the regime diagram is once again verified by the numerical experiments.

3.3.3 Summary

The behavior of weakly inertial particles injected in a channel laminar flow depends on the dimensionless number W and on the channel geometry. The separation between the transport, sedimentation and transition regimes is characterized by the linear variation of two critical values of W, W_{cr1} and W_{cr2} respectively. These two values are functions of the ratio between the aperture and the total length of the channel, which is characterized by the dimensionless number $h^* = \dfrac{H_0}{L_\infty}$. $W_{cr1} = c_1 h^*$ defines the limit between the transport and transition zones, while $W_{cr2} = c_2 h^*$ defines the limit between the transport and the sedimentation zones. This leads to the definition of a regime diagram that is valid for arbitrary channel geometries.

It was found that configurations involving a channel with flat walls and a channel with in phase sinusoidal walls ($\alpha = 0$) share the same values of c_1 and c_2. When the top and bottom walls are shifted, the direction of this shift does not affect the distance traveled by the particles. However, transport and sedimentation zones are optimum when the phase lag between the two walls is maximum($\alpha = \pi$).

In channels with identical walls ($\gamma = 0$), increasing the wall corrugation (δ_0) or the horizontal shift (α) tends to enlarge both the transport and the sedimentation zones. In channels having nonidentical walls ($\gamma \neq 0$) and a maximum phase lag ($\alpha = \pi$), the increase of the upper wall corrugation compared to the lower one leads to a narrower transport zone and to a larger sedimentation zone. The transport zone increases when the upper wall corrugation decreases, and reaches its maximum size when the upper wall becomes flat ($\gamma = -1$). Conversely, increasing the upper wall corrugation promotes sedimentation, and the sedimentation zone reaches its maximum size when the lower wall becomes flat ($\gamma = 1$).

3.4 Conclusion

This chapter was devoted to the study of the transport regimes of particles with low inertia, in 2D fracture flows. The flow was assumed to be laminar and dominated by viscous forces, characterized by low values of ϵ and Re, ϵ being the fracture aspect ratio and Re the flow Reynolds number estimated on the fracture mean aperture. Channels with flat and sinusoidal walls were considered to represent different fracture geometries.

We showed that when particle inertia is neglected, the particle behavior can be characterized by the channel geometry and a dimensionless number W which represents the ratio between the particle settling velocity and the flow mean velocity. A differential equation defining the particle trajectory in corrugated channels and an exact equation of this trajectory in channels with flat walls were derived under the assumption that particle inertia can be neglected and that the flow velocity components can be explicitly calculated using the LCL. These equations were verified against numerical experiments based on a particle tracking technique combining the particle motion equations together with the flow field obtained by solving the NS equations. The numerical simulations were performed taking into account both particle and fluid inertias. The numerical results confirmed the assumptions under which the analytical approach was developed. Furthermore, it confirmed that the particle trajectory can be directly predicted according to the value of W and to the channel geometry without the need for further calculations or numerical simulations.

Based on these developments, a regime diagram was established, which predicts the transport or the sedimentation of particles as a function of W and of a geometrical parameter h^*, representing the ratio between the channel mean aperture and its total length. For channels with corrugated walls, the regime diagram is similar to the one obtained for channels with flat walls, but the zones of transport and sedimentation tend to increase or decrease depending on the channel geometry, related to the corrugation wavelength and amplitude and to the phase lag between the channel walls. It is shown that for a corrugated channel having two in phase walls, the regime diagram is identical to the one obtained for a channel with flat walls. When the two walls are out of phase, increasing the wall corrugation leads to an increase of the zones of transport and sedimentation in the diagram. Taking into account

the asymmetry between the two walls corrugations, increasing the upper wall corrugation relatively to the lower one tends to decrease the transport zone and to increase the sedimentation zone. The regime diagram and the effects of the geometrical parameters on its zones variation were verified by numerical experiments which were conducted by releasing 100 particles in the channel and by computing the percentages of particles that deposited inside the channel.

The results presented in this chapter describe in which way the geometry of a fracture affect the transport and the deposition of particles as well as the distance at which they will deposit inside the fracture.

In the following chapter, the experimental device that was designed to verify the analytical results is presented.

Chapter 4

EXPERIMENTAL INVESTIGATION OF PARTICLE TRANSPORT IN FRACTURE FLOWS

An analytical model describing the transport of weakly inertial particles in closed channels with flat and corrugated walls has been proposed in chapter 3, under the assumptions that particle inertia is neglected and that the flow follows the local cubic law (LCL). This analytical model has been verified numerically taking into account particle inertia and fully solving the Navier-Stokes (NS) equations. To go further, an experimental validation is required. In order to consider real situations and to assess the validity of the analytical model on a practical basis. In this chapter, the experimental apparatus that was designed and built up to this end is presented. The first part of the chapter is devoted to the presentation of the design and the setup of the physical model. Then, the experimental procedure and the methodology used to process the experimental data are described. Finally, several preliminary results are presented and discussed with respect to the initial objectives of the study.

Introduction

The experimental apparatus is first described and explanations are given regarding the design of each one of its components. In the past, numerous experiments have been performed to investigate flow and particle transport in open and closed channel flows. Laboratory scale open channels are commonly used to reproduce phenomena occurring in earth-surface liquid flows such as sediment transport in rivers (Best [125],Yilmaz [126], Wang et al. [127]) and sand transport in near-shore regions (Jarno-Druaux et al. [128], Chu et al. [129]).

Similarly, laboratory scale closed channels have been used to model flows in either natural (e.g. Hakami and Larsson [41]) or synthetic (e.g. Qian et al. [102]) fractures. Synthetic fractures can be made either by creating surface roughness replicating that of real fractures (Yeo et al. [130], Ju et al. [131]), or by considering fracture walls with idealized roughness. For instance, Qian et al. [102] glued small square plates on flat surfaces to generate surface roughness. Crosnier [53] used disks with crenelated surface to study flow in radial fractures. In the present work, we made the choice to model rough fractures as channels with sinusoidal walls (cf. chapters 1 and 2). Our experimental apparatus and its schematic representation are shown respectively in Figures 4.1 and 4.2. It consists of a transparent long open channel in which a fluid is circulating in a closed circuit. Inside the channel, two Plexiglas plates are inserted to simulate the fracture. These plates can be flat or sinusoidal. Fluid flow is created by applying a pressure drop between the inlet and the outlet of the fracture. In such a configuration, the hydraulic gradient can be controlled directly by adjusting the liquid level difference between inflow and outflow flumes (e.g. Qian et al. [102]) or by placing the fracture in an open channel flow (e.g. Rush et al. [132]). In our experiments, we opted for the second option. Liquid circulation is assured by three centrifugal pumps that move the liquid from the reservoir toward the channel and regulate the flow rate. A digital camera is used to track the movement of the particles inside the fracture. The camera is fixed on a conveyor belt (charlyrobot) whose movement follows the flow main direction. To illuminate the zone of the recordings in order to improve the quality of the pictures, two light projectors are placed above the fracture. A computer connected to both the charlyrobot and the camera allows to control the displacement of the camera and the quality of the captured pictures.

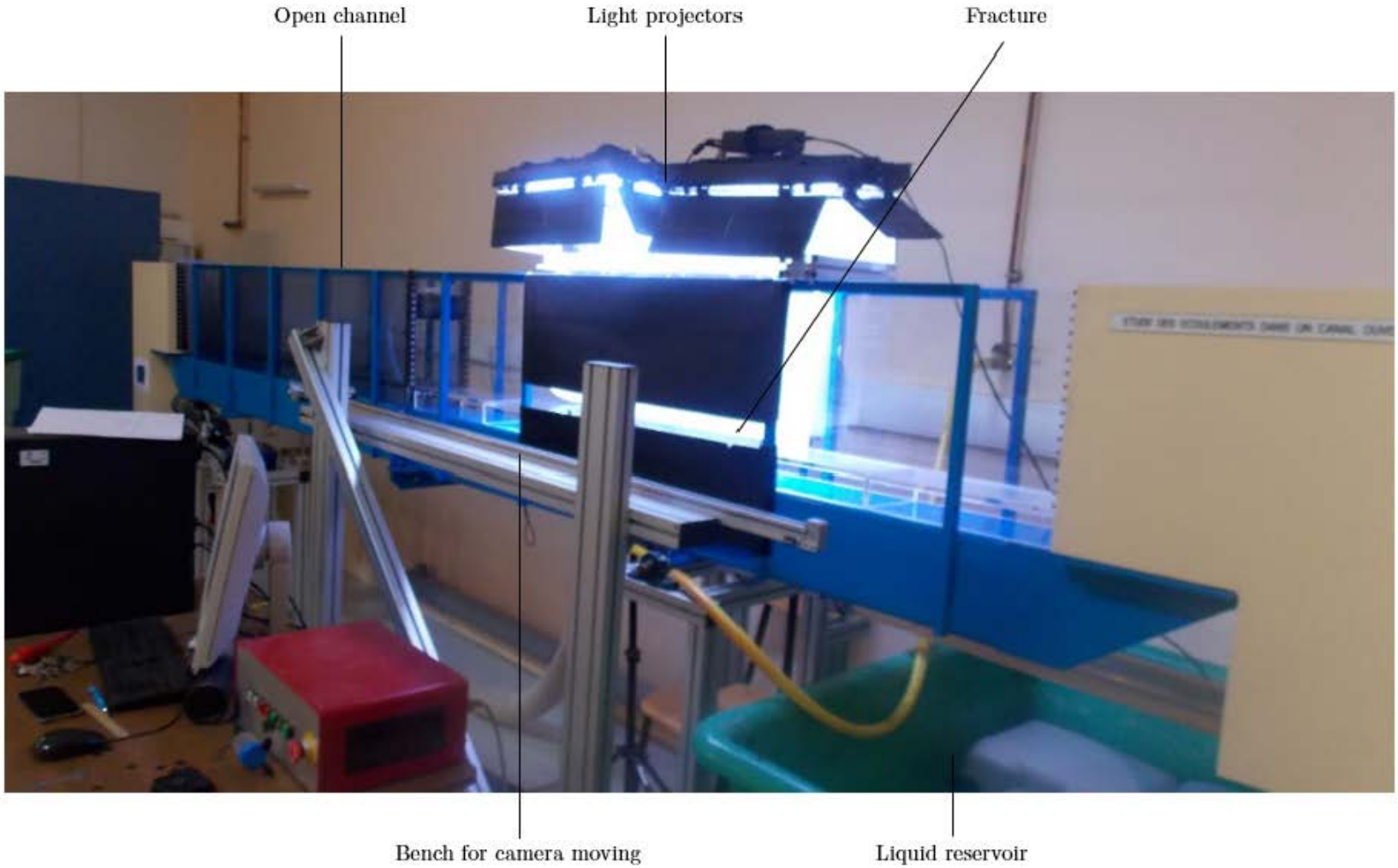

Figure 4.1: Picture of the experimental apparatus

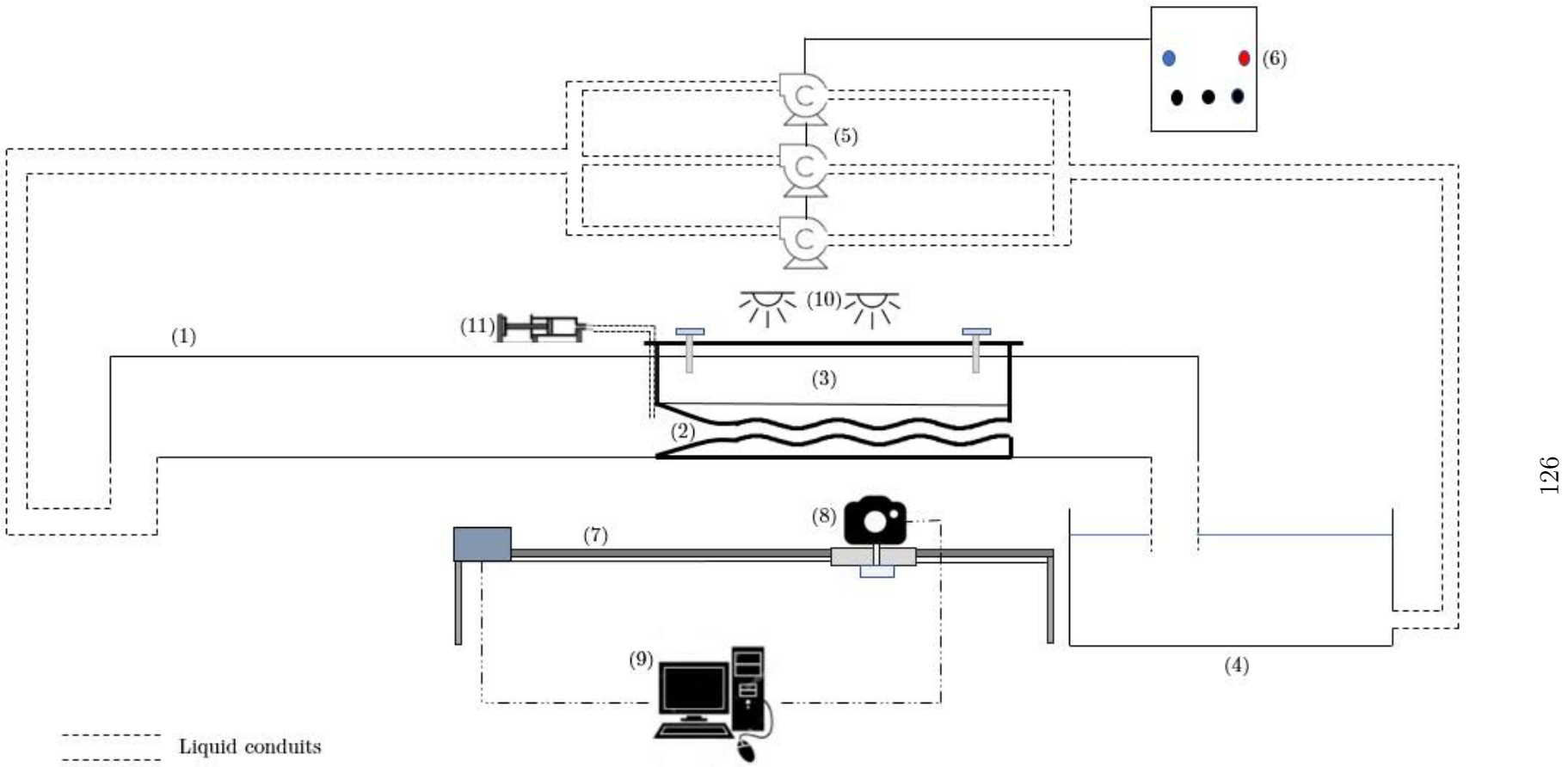

Figure 4.2: Schematic representation of the experimental apparatus

Since the aim of this apparatus is to assess the analytical solution developed in chapter 3, the experimental setup was designed in such a manner that it satisfies the theoretical assumptions. In particular, two main constraints were considered to define the dimensions of the fracture walls. First, the flow through the fracture must be unidirectional and must follow the LCL. It is obvious that this latter condition implies a certain constraint on the flow rate through the cross-section of the fracture. Second, the corrugations of the fracture walls must be smooth (cf. chapter 2), and it should be possible to adjust the aperture and the phase shift between the fracture walls so as to investigate different fracture configurations..

A detailed description of the experimental apparatus as well as the choice of the fracture walls dimensions are presented in the next sections.

4.1 Experimental setup and procedure

4.1.1 Open channel with closed circuit flow

The channel is designed and manufactured by *DIDATEC Technologies*. It was initially dedicated to study open channel systems but we modified it by inserting a fracture model into the flume (Figure 4.3).

The channel has a total length of 400 cm and a cross section of 16×34 cm^2 (width $\times$ height). The side walls are made of transparent reinforced glass, to ease the visualization of the flow. All the other components in contact with the liquid are made of stainless steel or glass reinforced plastic to prevent corrosion. The inclination of the channel can be finely adjusted using a screw system and inclinometer that indicates the angle of inclination. In our experiments, the channel has been always placed in a horizontal position. All the equipment is set up on an steel coated frame. The frame is equipped with adjustable rubber feet to avoid vibrations.

Upstream, a polyethylene stilling tank is connected to the centrifugal pumps, with a drain valve in its lower part. A honeycomb (flow straightener) is placed in the tank at the channel inlet to reduce turbulence (Figure 4.3(c)). Downstream, another tank is placed with direct evacuation into the main reservoir. The reservoir is a tank made of fiberglass with a capacity of 500 L and is connected to the liquid pumps. It has a transparent lid and a drain

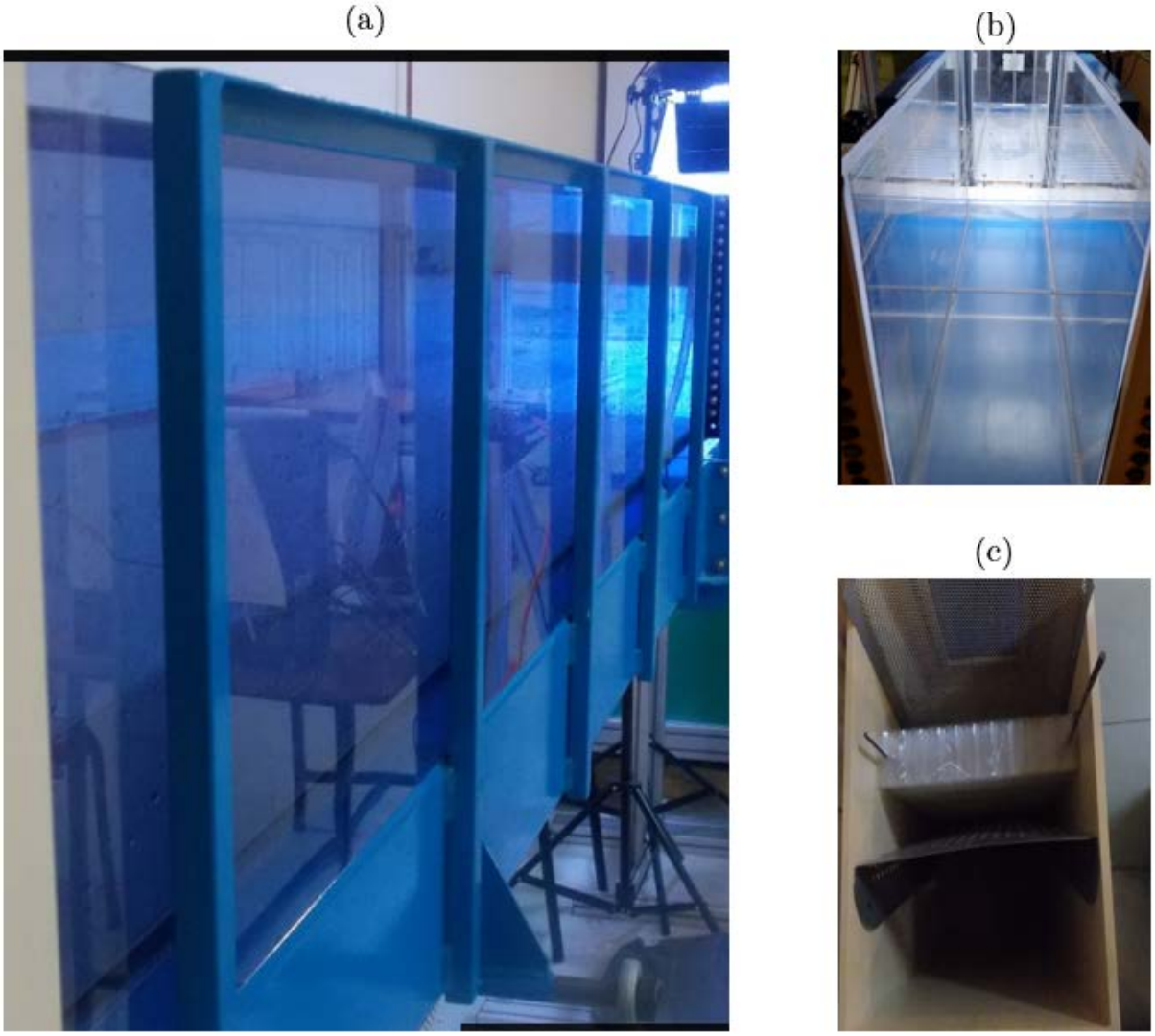

Figure 4.3: The open channel used in the experiments. (a) Side view showing the channel walls. (b) Inside view of the channel. (c) The honeycomb (flow straightener) inserted at the channel inlet.

valve and is equipped with a low-level sensor that turns off the pumps as soon as the liquid level is lower than the inlet of the pumps.

Liquid circulation between the reservoir and the channel is ensured using a pumping system. This system consists of three centrifugal pumps, an electromagnetic flow meter, an electrical control box, and different valves (Figure 4.4). Each pump has a flow rate that can be adjusted between 50 and 350 L/min (3 and 21 m^3/h). The speed of the pumps is controlled by a manual set point frequency. A flow meter measures the total flow rate of the

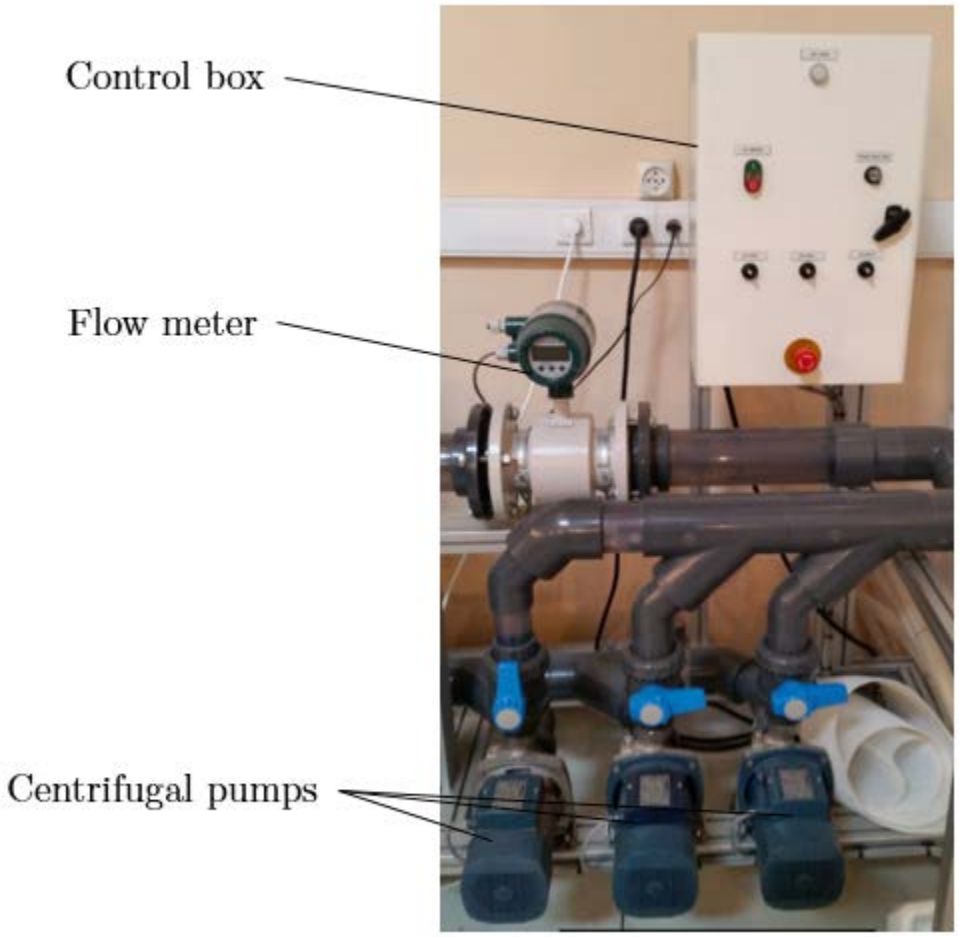

Figure 4.4: Pumping system consisting of centrifugal pumps, a flow meter, and electrical control box.

liquid transported from the reservoir to the channel. The flow rate is adjusted by actuating one or more pumps.

4.1.2 Fractures with flat and sinusoidal walls

The fractures used in the experiments have flat and/or sinusoidal walls (Figure 4.5). The fracture model is placed at 2.5 m from the open channel inlet. The fracture walls are made of PMMA Plexiglas (Poly(methyl methacrylate)) and have a thickness of 2.8 cm, a total length of 68 cm and a width of 16 cm, so as to match the width of the open channel. In every configuration, the lower wall is fixed to the bottom of the open channel using three

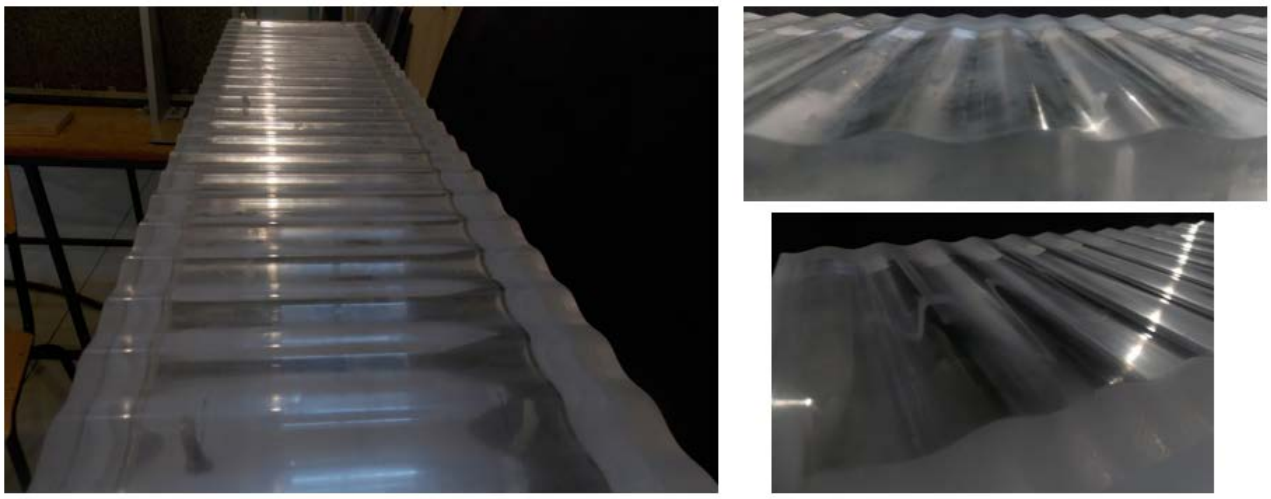

Figure 4.5: Top and side views of the sinusoidal walls used in the experiments.

drywall screws on each side. The upper wall is fixed, using 6 machine screws, on a hollow slab which is also made of PMMA (Figure 4.6).

Figure 4.6: The hollow slab holding the upper wall and the bolts used to raise and lower the slab.

On the upper part of the slab, six bolts are inserted and their heads are placed on the upper edge of the side walls of the open channel. Turning these bolts out increases the distance between the slab and the channel walls and raises the slab. Therefore the distance between the upper and lower walls of the fracture, which corresponds to the aperture, can

be adjusted. In the same way, by turning the bolts in the opposite direction, the fracture aperture can be decreased. The mean aperture of the fracture H_0 can be varied between 0 (When the bolts are fully inserted and the two walls are completely in contact one with each other) and 2 cm (when the bolts are pulled out to the maximum). Similarly to the method used to move the slab vertically, two bolts were inserted on the right side of the slab and allowed it to move horizontally. In this way, the phase shift between the upper and lower wall can be modified in order to control the phase lag between them (cf. chapter 2).

4.2.2.a. Fracture geometrical properties

Fractures with flat walls are only defined by their mean aperture H_0 which, in our case, can vary between 0 and 2 cm as mentioned in the previous section. The total length of the walls is equal to $L_\infty = 69\ cm$. For sinusoidal walls, the fracture roughness is defined by the wavelength L_0 and the amplitude A of the wall corrugations (A_0 is the mean corrugation amplitude between the two walls), the horizontal phase shift between the two walls ΔX.

Two identical sinusoidal walls were machined with $A = 1.25\ mm$ and $L_0 = 2.5\ cm$ (Figure 4.7). These two parameters were selected in order to have smooth wall corrugations, which is a condition for the LCL to be valid and for eliminating the risk of having recirculation zones in the fracture furrows (cf. chpater 2).

By combining the flat and sinusoidal walls, 4 geometrical configurations of the fracture can be studied respectively:

i with two flat walls

ii with a lower flat wall and an upper sinusoidal wall

iii with a lower sinusoidal wall and an upper flat wall

iv with two sinusoidal walls

The geometrical properties of the fracture can be adjusted in the following way:

- $\epsilon = \dfrac{H_0}{L_0}$ can be varied between 0 (when the two walls are in contact) and 0.8 (when H_0 is maximum). Practically, ϵ is varied between 0.1 and 0.4 to ensure that $\epsilon \leq 0.4$ (cf. chapter 2).

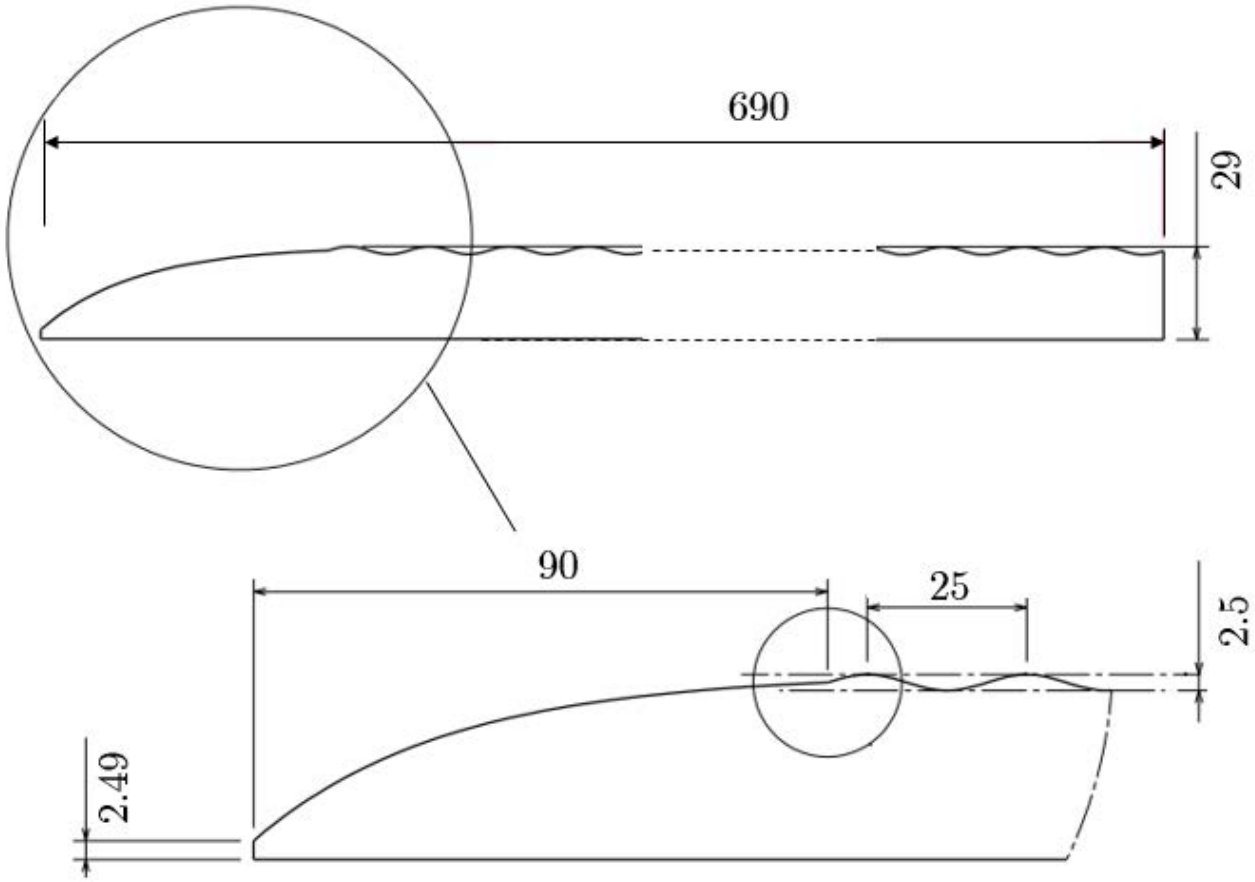

Figure 4.7: The dimensions of the sinusoidal walls (in mm).

- $\delta_0 = \dfrac{A_0}{H_0}$ can be varied between 0.03 when one of the walls is flat and the aperture is maximum, and 0.5 when the two walls are sinusoidal and the aperture is minimum.

- $\gamma = \dfrac{A_2 - A_1}{A_2 + A_1}$ (A_2 corresponds to the upper wall and A_1 to the lower one) can be varied between -1 (in the case (iii)) above, 0 (case (iv)) and 1 (case (ii)).

- $\Delta x = \dfrac{\Delta X}{L_0}$ can be varied between 0 when the walls are in phase, and 0.5 when the phase shift is maximum.

The walls inlet follows an exponential profile instead of a rectangular one to ensure a smooth laminar flow and to avoid any stagnant zone that may appear at the lower wall inlet (Figure 4.7). The flow through the fracture is created by a hydraulic head difference Δh (pressure difference $\Delta P = \rho g \Delta h$) between the inlet and the outlet.

4.2.2.b. Particle injection

In order to verify the theoretical results, the particles must be small, typically less than 1 mm in diameter. In addition, the analytical model was developed in 2D. To be able to reproduce the 2D conditions experimentally, particles must stay away from the side walls of the open channel to avoid any particle-wall interaction that may affect their behavior.

The first technique adopted for injecting the particles in the flow consisted in dropping them off directly in the closed circuit and tracking them as soon as they enter the fracture. This technique is the less restrictive and is eased by the fact that the centrifugal pumps allow the passage of suspended solids up to 10 mm in diameter. However, many difficulties arose when using this technique. First, the particles are randomly dispersed in the flow, meaning that they can enter the fracture at different positions along the width and at different times. Particles can then be very close to the open channel side walls which may thus affect their behavior. This technique would be fine for studying particle transport in tubes (e.g. Segré and Silberberg [28], Matas et al. [32]), but it is not convenient in our case. Second, as will be discussed later on, some particles can be located out of the camera focus. Finally, the moment at which particles enter the fracture can not be precisely estimated and the recording start time is thus unknown.

To overcome these difficulties, another technique was chosen. It consists in injecting the particles manually and directly at the fracture inlet, at the center of the flow path. To make this possible, a rubber hose was fixed on the slab holding the fracture upper wall (cf. section 2.2) with one end directly positioned at the fracture inlet (Figure 4.8). The other end is connected to a plastic syringe used to inject the particles. The syringe has a volume of 50 mL and the internal diameter of its tip is 2 mm. To avoid the appearance of air bubbles in the flow, the particles are placed in the syringe without the liquid and the piston is fully pushed in. The syringe is then attached to the hose and the liquid is sucked up directly from the open channel. In this way, the nozzle only contains liquid without any air bubbles. Finally, the syringe is shaken to disperse the particles in the liquid before injecting the suspension into the fracture.

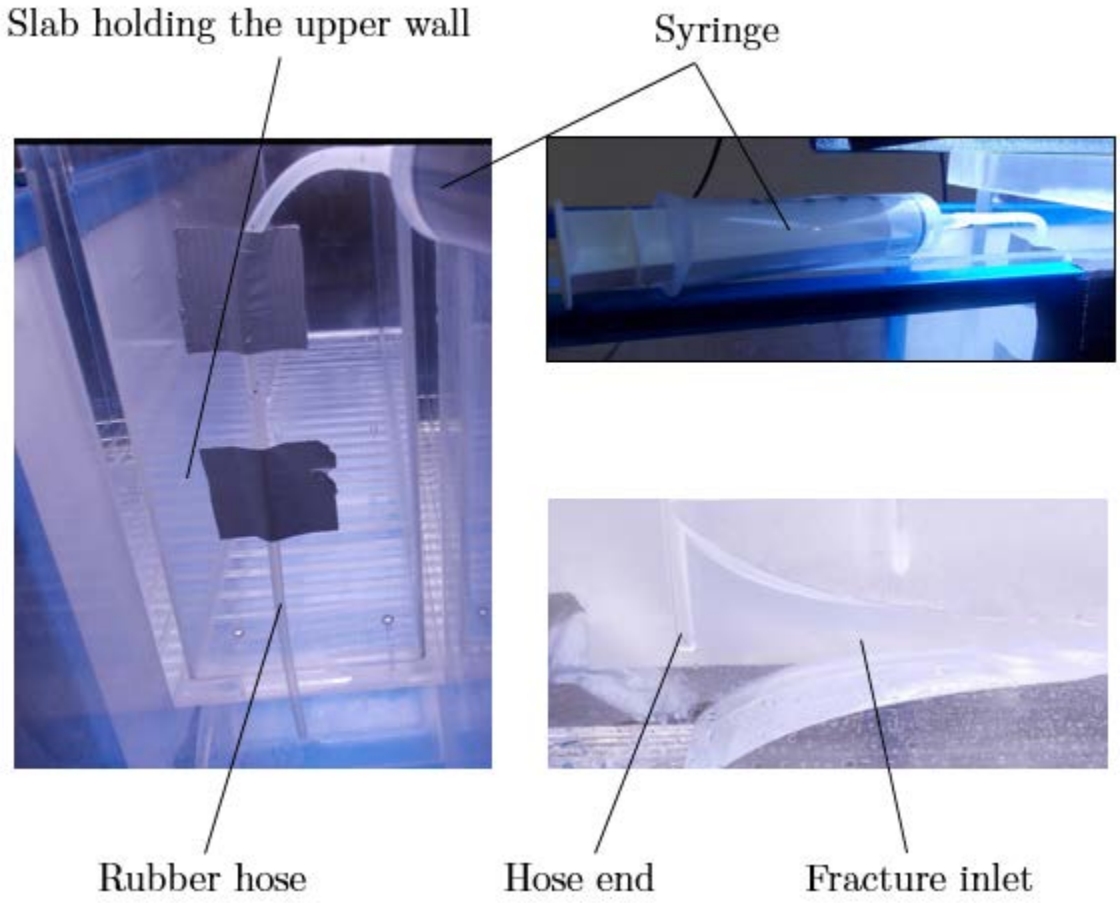

Figure 4.8: The syringe and the rubber hose used to inject particles at the fracture inlet.

4.1.3 Liquid properties

At first, we intended to work with water as a liquid. The problem that appeared was that this option could only provide too high Re with regards to the assumptions made concerning the study of particle transport (cf. chapter 3). As an example, to assure $Re = 5$ in a fracture having two flat walls with $H_0 = 5\,mm$, the hydraulic head must be $\Delta h = 0.03\,mm$ which is, from an practical point of view, impossible to set up. Therefore, the use of another fluid has been considered to match the purpose of the study. Nonetheless, we performed some preliminary tests with water to verify the capability of our experimental device to produce lift induced particle focusing, as a validation step.

In order to reduce inertial effects and Re, a liquid with higher viscosity was considered. We chose to work with glycerin which is odorless, colorless and has a viscosity theoretically about 1000 times higher than water. The problem with the glycerin alone is that its very high

viscosity risks to reduce significantly the hydraulic characteristics of the centrifugal pumps. As glycerin is soluble in water, we decided to mix glycerin and water with a volumetric ratio 1L of water/4L of glycerin. This ratio was selected because according to the empirical formula of Cheng [133], the viscosity of the mixture at $20°C$ is expected to be in the order of $65cSt$, which is a moderately high viscosity with respect to water. The liquid reservoir was then filled approximately with 50 L of water and 200 L of glycerin. The selected glycerin has a degree of purity higher than 99.5% and a water content inferior to 0.5%. The kinematic viscosity of the mixture ν_f was measured with a glass capillary (U-tube) viscometer, for temperatures ranging from $20°C$ to $31°C$. The variation of ν_f as a function of the temperature is plotted in Figure 4.9.

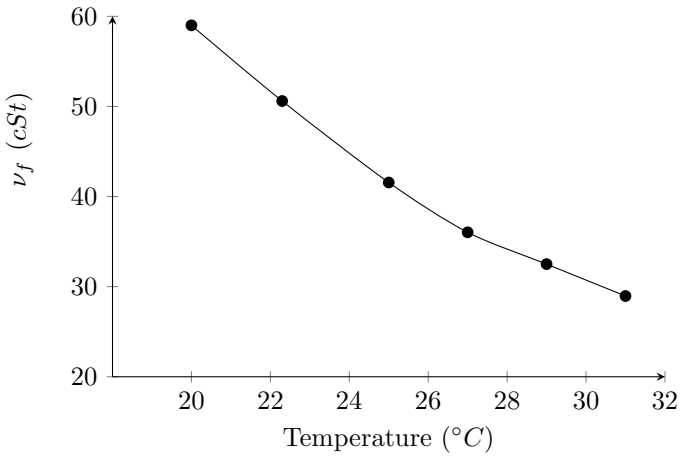

Figure 4.9: Variation of the kinematic viscosity of the water-glycerin mixture as a function of the temperature, as measured by the glass capillary viscometer.

Moreover, as the density varies slightly with the temperature, the mixture density ρ_f was measured at room temperature ($20°C$). This was done by measuring the weight m_f of a predefined volume V_f. To take into account the measurement errors that may occur, the weights of different volumes were measured (Table 4.1).

Throughout the experimental study, we considered $\rho_f = 1211kg/m^3$.

Table 4.1: Density of the mixture as the ratio between measured weights m_f and volumes V_f.

V_f (mL)	m_f (g)	ρ_f $(g/L$ or $kg/m^3)$
50	60.33	1206.6
100	121.02	1210.2
150	182	1213.3
200	242	1213.5
Mean density		1210.9

4.1.4 Visualization and image treatment

4.2.4.a. Lighting

To improve the tracking of the particles with the camera, two light projectors were placed above the fracture. These projectors were adjusted to shed white light on the fracture, so that particles with different color can be easily detected. To isolate the fracture walls from the rest of the channel, two black cardboards were glued to the side walls above the upper wall and below the lower wall so that only the fracture walls and the gap between them are visible (Figure 4.10).

4.2.4.b. Camera and bench

The camera utilized in the experiments (*Canon EOS 6D*) is a 20.2-Megapixel full-frame CMOS digital single-lens reflex camera. It is equipped with a $24 - 105\ mm$ zoom lens with optical image stabilization. Throughout the experiments, the lens was set with a maximum zoom in. Each setting of the camera is controlled by the application *EOS Utility* which is also used for remote shooting and for download and display. Videos recorded by the camera have a 1920×1080 full high definition recording quality and the frame rate was set to 50 fps.

The camera is fixed on a bench equipped with a motor-driven belt conveyor (Figure 4.11). The total length of the bench is $1.7\,m$. The stepping motor allows to define a moving velocity up to $1.5\,m/s$. It is controlled by the application *MINIMOVE* which allows to set the position and the displacement velocity. The camera can be then fixed at any position alongside the fracture. It can be also moved along the fracture length to follow the displacement of the

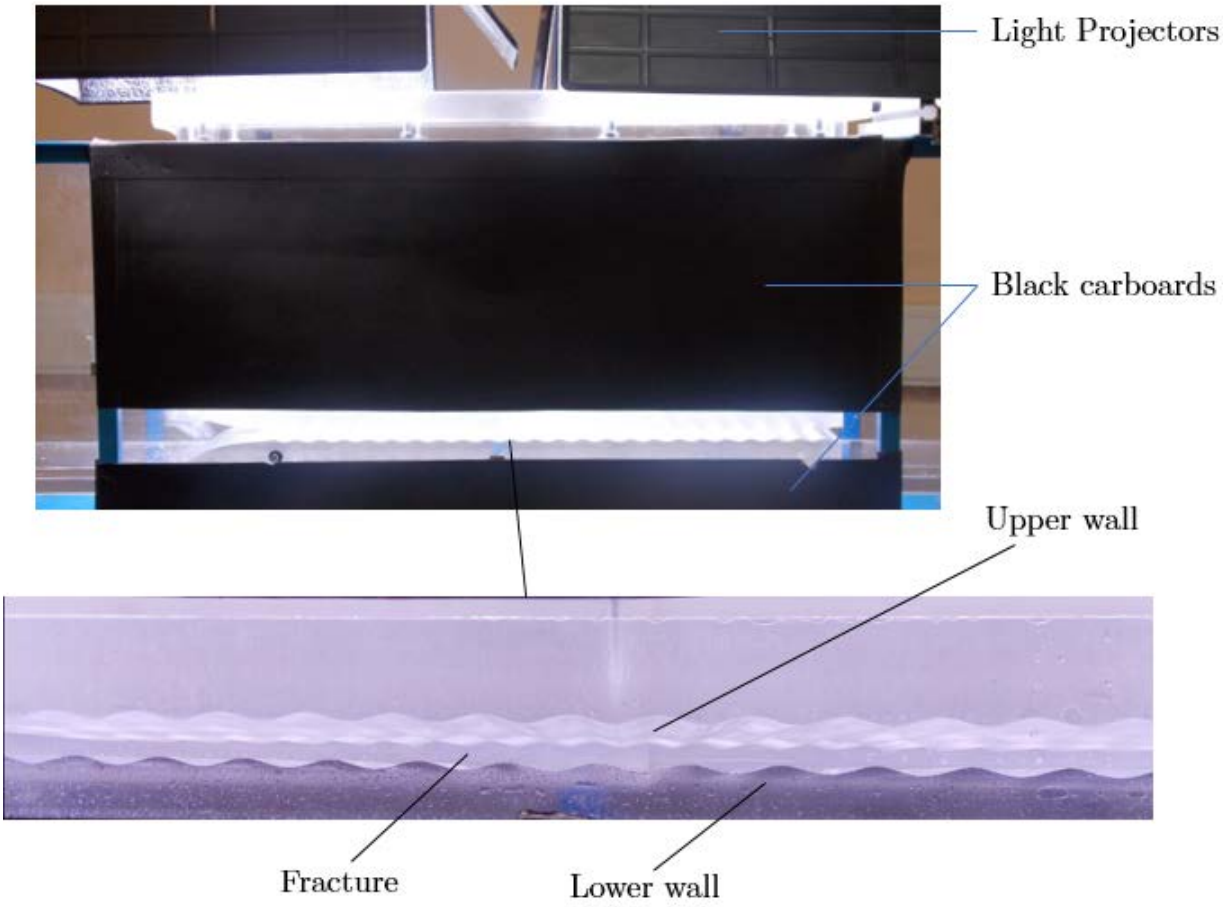

Figure 4.10: The black cardboards placed on the open channel wall to isolate the fracture and to ease visualization. The visible part of the fracture is also shown.

particles inside the fracture. Throughout the experiments, videos are either recorded at a fixed point such as the inlet and the outlet of the fracture, or recorded while the camera is moving along the fracture length.

4.1.5 Experimental procedure and image treatment

The first components to install in the experimental apparatus are the fracture walls. According to the predefined geometrical properties (flat or sinusoidal walls), two walls among the four available are selected. The lower wall is first fixed. Then, the upper wall is fixed on the holding slab, and the slab is then placed and adjusted according to the desired mean aperture and, when applicable, to the phase shift between the two walls.

The camera is fixed on the belt conveyor. Particles are inserted into the syringe which

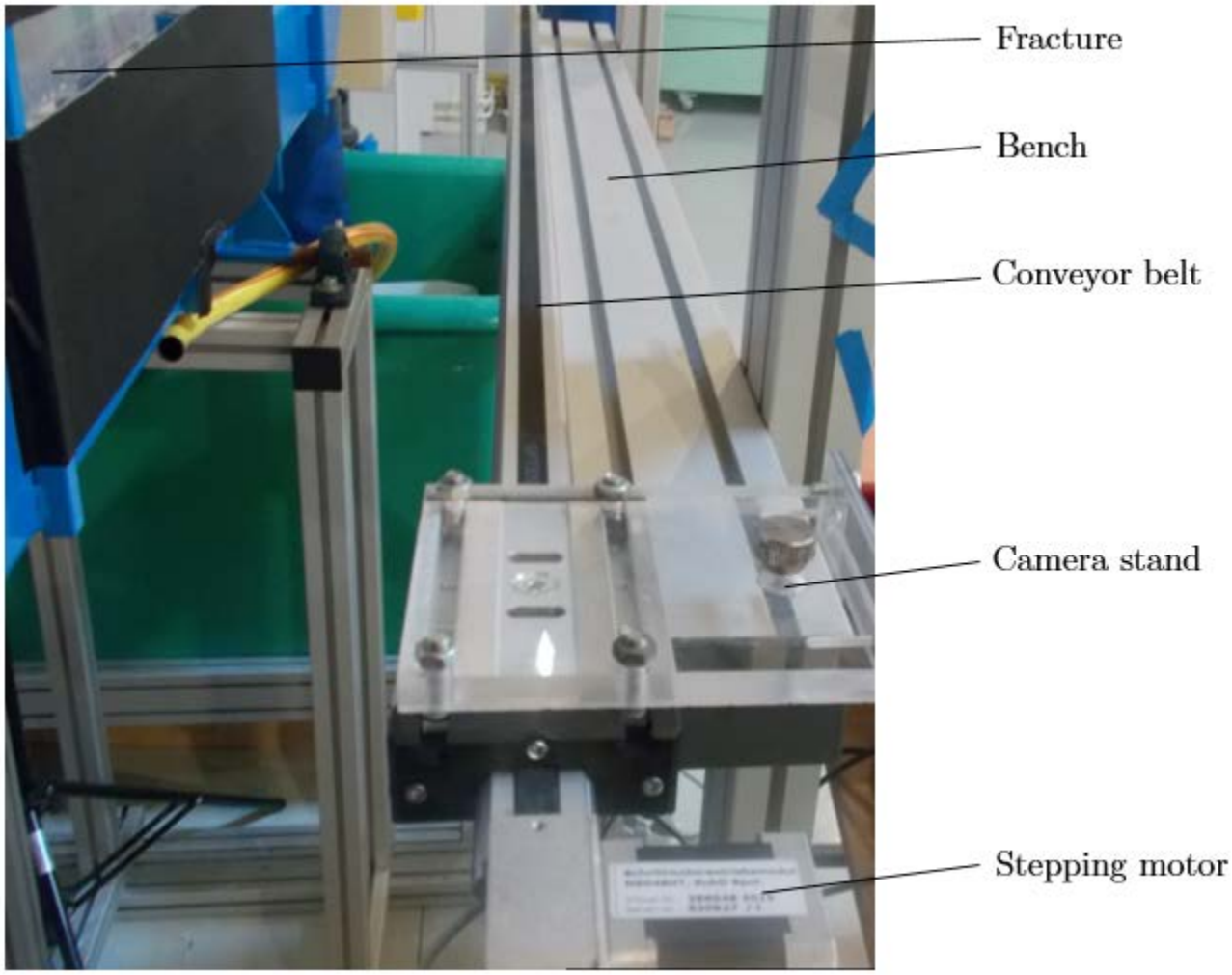

Figure 4.11: The bench and the belt conveyor on which the camera is fixed.

is then connected to the inlet hose. When using the water-glycerin mixture, the pumps are turned on for at least one hour to ensure that the glycerin is completely dissolved in water and that the mixture is thus homogeneous.

In the experiments where the camera is fixed at a specified point alongside the fracture, recording is started directly once the particles are injected and is turned off when all the moving particles have passed.

When the camera is moving along the fracture, a first test is performed to determine the velocity at which the belt conveyor should be set. Then, the experimental procedure is as follows:

1. The camera is positioned at the fracture inlet.

2. The video recording is turned on and particles are injected immediately after.

3. As soon as the particles get out of the hose end and enter the fracture, the camera is translated at the velocity previously determined.

4. When the camera reaches the fracture outlet, recording is turned off when all the particles have passed.

5. The video is then post-processed by applying an image treatment procedure described hereafter.

The image treatment procedure consists first in transforming the recorded video into a series of images. For that purpose, we used the software *MPlayer*. The number of images depends on the duration of the video, knowing that the frame rate of the camera is set at 50 frames/second. As an example, a video of 10 s duration will be transformed into 500 images.

After that, the number of pictures is reduced by keeping only those which feature particles. For instance, when the camera starts recording before the particles are injected, the first images without particles are deleted, and the same goes for the last images that were recorded after all the particles have exited the fracture.

The images are then edited using the open-source image editor *GIMP*. A simple Batch processing plugin, *David's Batch Processor*, is used to automatically perform operations on all the images because treating each image alone would be time-consuming and practically impossible. The image treatment procedure is as follows:

1. The images are cropped by selecting only the zone between the two walls. A random image is selected before, and cropped in *GIMP* in order to extract the crop required values (width and height) and apply them to the Batch Processor.

2. The contrast of the images is increased to make the particles more distinguishable.

3. This step is optional because it is possible at point (2) to directly process the images in order to track the particles and to find the distance to deposition, or to study particle trajectories. However, it is possible also to convert the colored images into black and white either directly or by applying a threshold.

An example of the image treatment is given in Figure 4.12 for a black poppy seed immersed in the water-glycerin mixture.

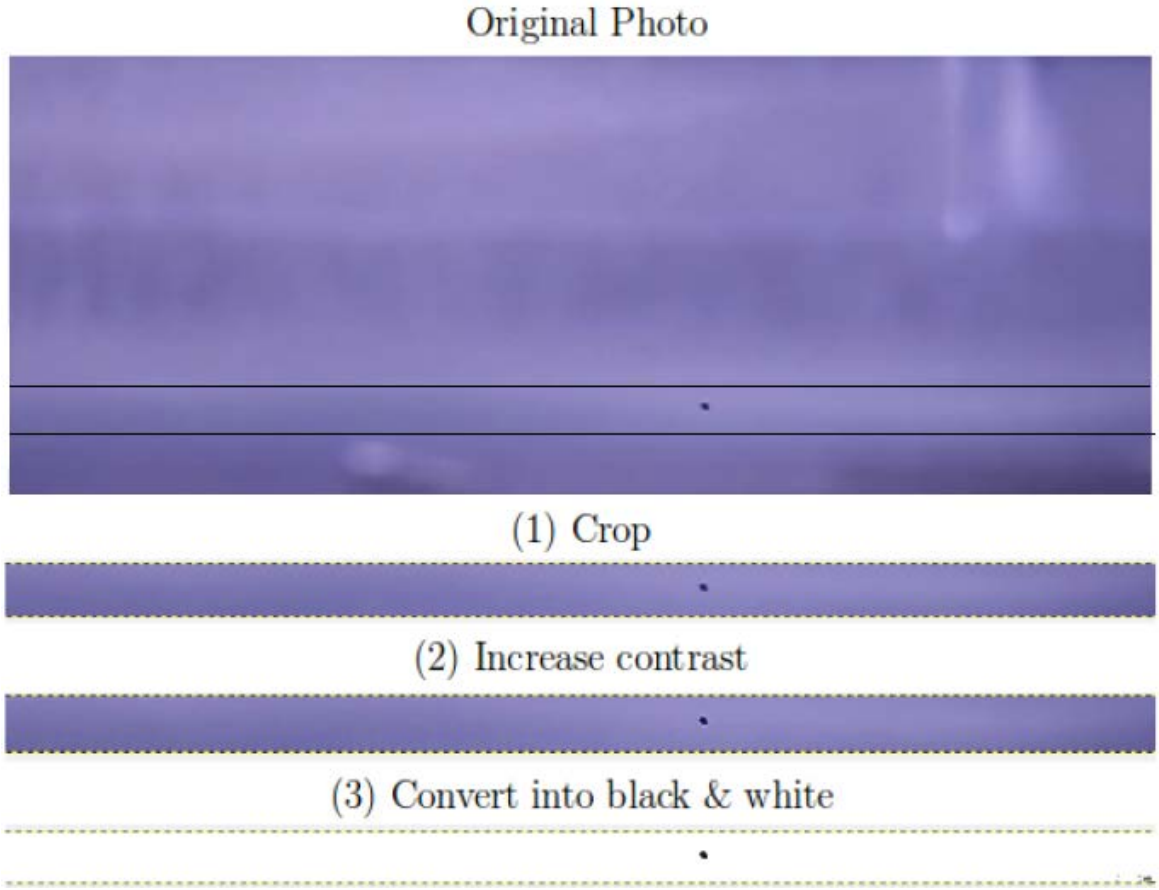

Figure 4.12: Image treatment applied in the case of a black poppy seed immersed in the water-glycerin mixture.

In addition to this procedure, it is possible to draw the trajectories of single particles when the camera is fixed, using a Matlab script, by adding successive photos of the moving particle and combining them into one. This will be shown later on when single particle trajectories are discussed.

4.2 Preliminary results with poppy seeds

The ability of the experimental apparatus to investigate particle transport in closed channels must be assessed before going into further investigations related to the analytical model presented in chapter 3. This was done by performing simple experiments using small

particles that can be easily found on a daily basis like, for instance, poppy seeds. In fact, poppy seeds are relatively small, have a quasi-spherical shape and a gray to black color, making them convenient for experiments and image treatment. However, poppy seeds are polydisperse. They have slightly different sizes and densities. This tends to slightly hinder the validation of the analytical model but it also provides a better representation of practical situations in which particles are neither perfectly spherical nor monodisperse.

4.2.1 Particle properties

The average density ρ_p of poppy seeds was first measured by weighing samples and by soaking them in a water volume V_f in order to measure the change in volume ΔV, which is equal to the particles volume V_p. To take into account measurement errors, four samples with different weights (m_p) were considered. The results are presented in table 4.2.

Table 4.2: Geometrical properties of the three fractures used as references in the numerical simulations.

$m_p\ (g)$	$\Delta V = V_p (mL)$	$\rho_p \quad (kg/m^3)$
5	10	1068
10	100	1072
20	150	1069
30	200	1070
Average density		1069.75

The considered measured density of poppy seeds is equal to $\rho_p = 1070\,kg/m^3$. This means that the particles are slightly denser than water and lighter than the water-glycerin mixture ($\rho_p = 1211\,kg/m^3$). This does not modify the analytical model verification, but instead of considering sedimentation or deposition, floating will be studied. In fact, the particle trajectories depend on the ratio k between the particle and liquid densities. In the case of poppy seeds immersed in water-glycerin mixture, $k < 1$ and the vertical position of the particles increases along the fracture length until the particles reach the upper wall. Hence, trajectories are investigated from the point at which particles are injected until they reach the upper wall.

In addition, all the particles do not have the same size. At first, using sieves, particle diameter d_p was found to range from $500\,\mu m$ to $1\,mm$. In order to find a more specific range

of d_p, an digital image analysis was performed. A portion of the particles was dispersed on a homogeneous paper and photographed. Using the software *ImageJ*, particles were converted into circular black dots on a white background and their surfaces were determined (Figure 4.13). d_p was then calculated.

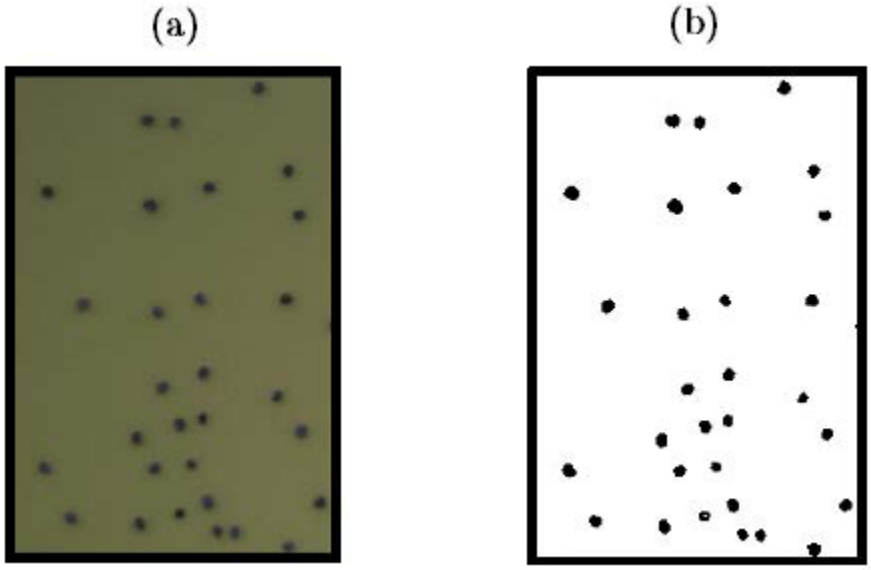

Figure 4.13: (a) A sample of poppy seeds dispersed on a homogeneous surface. (b) Particles converted into black circular dots on a white background.

The particle size distribution of a representative sample of 30 particles is presented in Figure 4.14. The mean value of d_p is 746 μm with a standard deviation of 147 μm. Therefore, in the following, d_p is considered as belonging to the range [600 μm; 800 μm].

4.2.2 Transport with water as the operating liquid

At first, experiments were performed using water as a liquid. In these experiments, the hydraulic head difference between the fracture inlet and outlet was set to $\Delta h = 9\ mm$. As mentioned above, in such a configuration, inertial effects dominate due to the low viscosity of the fluid. Therefore, lift forces can not be neglected, meaning that the analytical model presented in chapter 3 can not be assessed. On the other hand, one can expect the occurrence of inertial focusing in such configuration, meaning that particles injected randomly should focus on the same trajectory due to the lift forces acting on them (cf. chapter 3). Even though

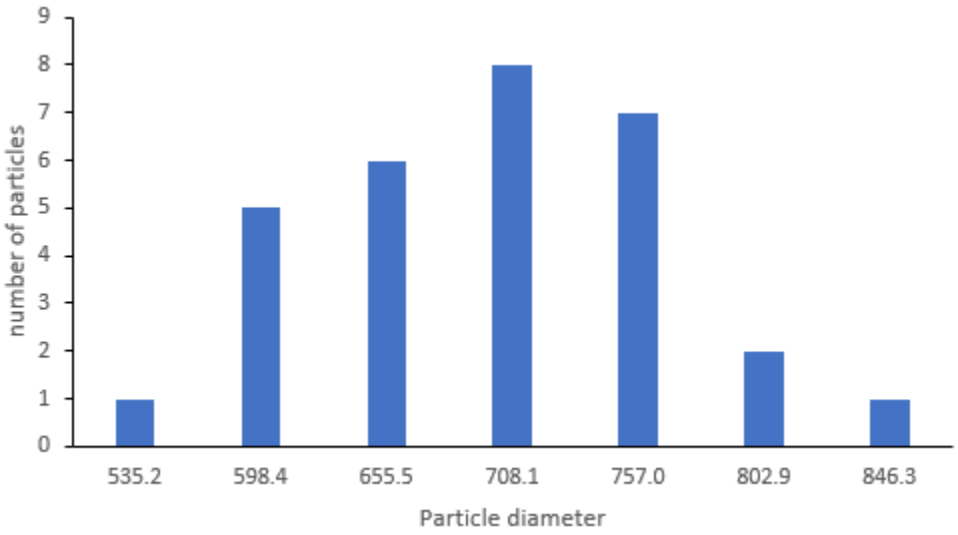

Figure 4.14: A histogram of particle size distribution of a representative sample of 30 poppy seeds.

poppy seeds are slightly denser than water, gravity forces are dominated by lift forces and therefore particles do not deposit on the lower wall. In order to verify the suitability of the experimental setup to deal with particle transport, we performed tests with water so that inertial focusing could be observed. Two experiments are proposed. In the first one, we injected a single particle. In the second one, we injected 2 particles. These particles were injected into a fracture with flat walls.

4.3.2.a. Trajectory of a single particles

First tests were performed by injecting a single particle into the fracture in order to study their trajectories. In such a configuration, particle-particle interactions are avoided and inertial focusing, if it is observed, is solely due to the effect of lift forces.

The camera was fixed right before the fracture outlet, capturing the last 15 *cm* of the fracture. One particle was injected at the fracture inlet, and it was filmed when it was exiting the fracture. The succession of particle positions after image treatment, allows to plot its trajectory as illustrated in Figure 4.15. According to this figure, it is clear that the particle trajectory is a straight horizontal line parallel to the fracture wall. By definition, this behavior is characteristic of inertial focusing.

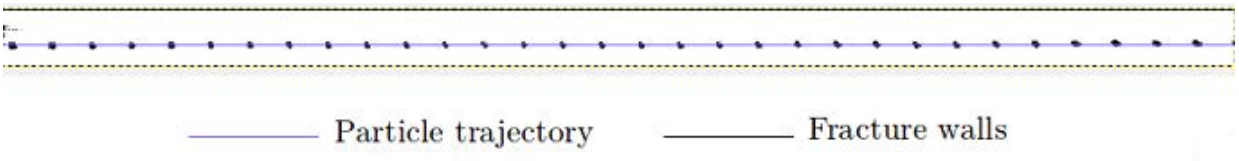

Figure 4.15: Single particle trajectory plotted at the fracture outlet as a succession of particle positions. (a) Positions of the particle at different times of the experiment. (b) Deduced particle trajectory

4.3.2.b. Inertial focusing of two particles

The experiment performed with a single particle was completed by a second test performed with two particles. The objective of this experiment was to test the same hypothesis as the previous case, i.e., if the two particles will exit the channel on the same trajectory, and to check if the slight difference in the physical properties (size and density) of the particles had an effect on their behavior. The same image treatment was performed and the two trajectories are plotted in Figure 4.16.

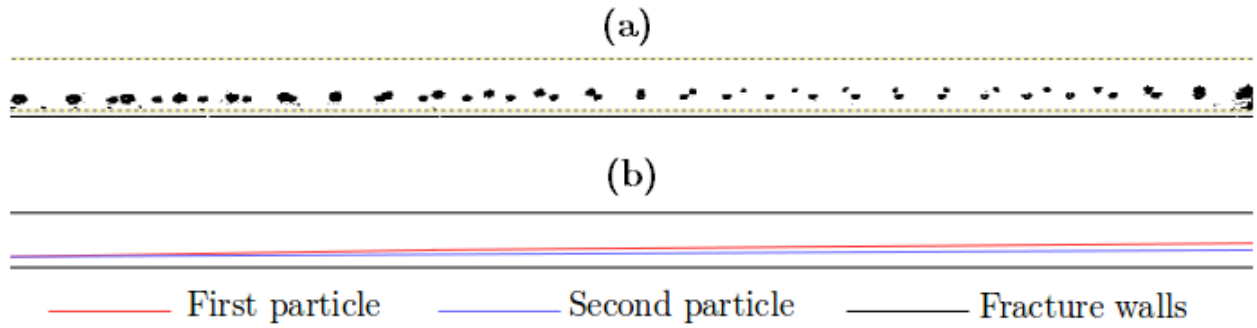

Figure 4.16: Trajectories of the two particles plotted at the fracture outlet as a succession of particle positions.(a) Positions of the two particles at different times of the experiment. (b) Deduced particle trajectories

The analysis of this figure shows a slight difference between the two trajectories which, however, remain almost parallel to the fracture wall. This small difference could be assigned to the respective physical properties of the particles that are not identical (they have a different size). Under these conditions, we can consider that the particles converge to an equilibrium position and that inertial focusing occurs. This result gives a first insight about the ability of the experimental apparatus to capture some of the physical mechanisms that take place in closed channel flows. It also confirms that inertial lift forces cannot be neglected

in our experiment when water is used and thus that the theoretical assumptions of our analytical model cannot be fulfilled.

4.2.3 Transport with water-glycerin mixture as the operating liquid

To investigate the particle deposition case, we replaced water by a water-glycerin mixture. This mixture presents a higher dynamic viscosity than that of water permitting to reduce, with a reasonable hydraulic head difference (Δh), the flow inertial effects. Therefore, we expect that the particles would float towards the upper wall. Comparisons can then be made with the predictions of the analytical model presented in chapter 3, in terms of distance traveled. For convenience, the term "deposition" is used to refer to the fact that the particle comes in contact with the upper wall. Deposition is normally used for particles that sediment on the bottom wall, but as the mechanism is the same, it will be used for particles that come in contact with the upper wall.

Another important advantage of choosing the water-glycerin mixture instead of the water alone, is that by increasing Δh, we can study non-inertial regimes at low Re (for small Δh), in which the analytical model is valid, as well as inertial regimes at high Re (for high Δh), in which the inertial effects are significant. This can thus give us insights into the limitations of the analytical model for high Re.

We recall that the analytical model was developed with the aim to predict particle trajectories and positions without knowing the exact flow velocity field. Instead, an approximated velocity is calculated using the LCL (cf. chapter 3). In fact, based on the hydraulic aperture H_h (which depends on the fracture geometry) and on the pressure difference ΔP, the flow mean velocity V_0 can be estimated. Then, depending on the particle radius a and on the density ratio k, the dimensionless number W is determined and the particle trajectory equation as well as the distance at which the particle will deposit can be calculated. This can be done under the assumption that the particles have a small inertia (particle response time $\tau < 10^{-3}$) and that $Re = \frac{V_0 H_0}{\nu}$ is small.

To sum up, in each case, Δh is set and Re is calculated. For relatively low Re, W and

τ are determined, and the distance to deposition can be calculated for each particle. This distance is compared to that found experimentally. For high Re, the presence of inertial focusing is investigated.

The mixture and particle properties are defined in sections 2.3 and 3.1. The mixture temperature was measured at different positions in the channel and at different times, using a mercury-in-glass thermometer and was found to be equal to $21.5\,°C$. The kinematic viscosity is approximately equal to $\nu_f = 55\,cSt$ and the density ratio is $k = 0.88$. As the particle diameter was defined in a given range, the same applies for W and τ. In the experiments, H_0 was varied between $5\,mm$ and $10\,mm$, and Δh between $0.8\,cm$ and $15\,cm$. In the following, we present selected significant results which show specific particle behaviors.

4.3.3.a. Fracture with two flat walls

The configuration with two flat walls was used with different values of H_0 and Δh.

i. Non-inertial regime: verification of the analytical model

The mean aperture was set to $H_0 = 5\,mm$ and the hydraulic head difference to $\Delta h = 2.5\,cm$, leading to $V_0 = 0.013\,m/s$ (using the LCL) and $Re = 1.184$. In this case, the dimensionless numbers are $\tau \in [9.6 \times 10^{-6}; 1.7 \times 10^{-5}]$ and $W \in [-0.058; -0.032]$. A picture illustrating the particles right before they exit the fracture is shown in Figure 4.17.

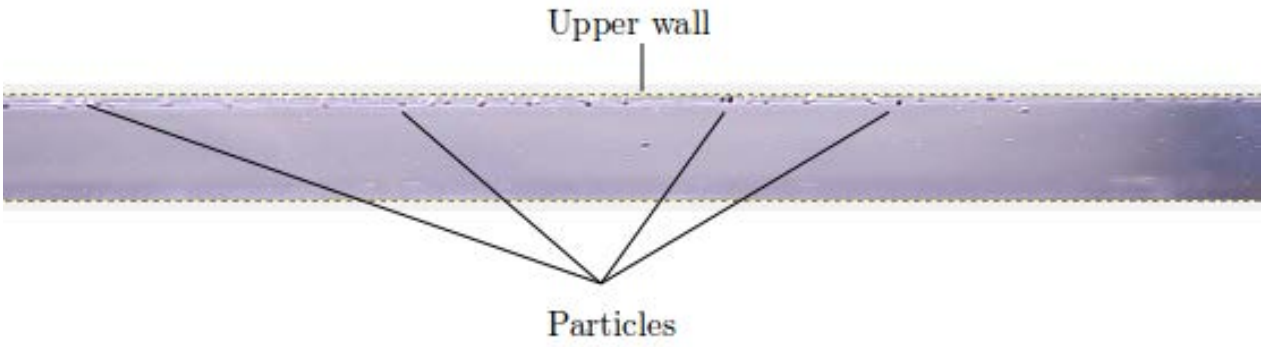

Figure 4.17: Multiple particles filmed moving on the upper wall, ahead of the fracture outlet for $\Delta h = 0.8cm$ ($Re = 1.184$, $\tau \in [9.6 \times 10^{-6}; 1.7 \times 10^{-5}]$ and $W \in [-0.058; -0.032]$).

According to this figure, the majority of the particles floated and were moving on the upper wall. This means that the inertial lift forces are negligible with respect to gravity

(buoyancy) forces. To assess the predictions of the analytical model, a random particle with an initial vertical position $z_p^0 \simeq 0$ was selected. For this particle The distance to deposition (in the dimensionless form with L_∞ as a length scale $x^f = \frac{X^f}{L_\infty}$) was found experimentally (Figure 4.18) to be $x^f_{exp} = 0.075$ (or $X^f_{exp} = 0.051\,m$ in the dimensional form). Note that in the case of a fracture with a corrugated wall, the distance to deposition can be more easily determined by counting the number of the wavelengths that the particle has traveled before touching the wall. Using the analytical model, the range of the distance to deposition x^f_{ana} is equal to $x^f_{ana} \in [0.043; 0.078]$ (or $X^f_{ana} \in [0.029\,m; 0.053\,m]$) considering the range of W mentioned above. This means that the distance to deposition found experimentally falls in the range predicted by the analytical model.

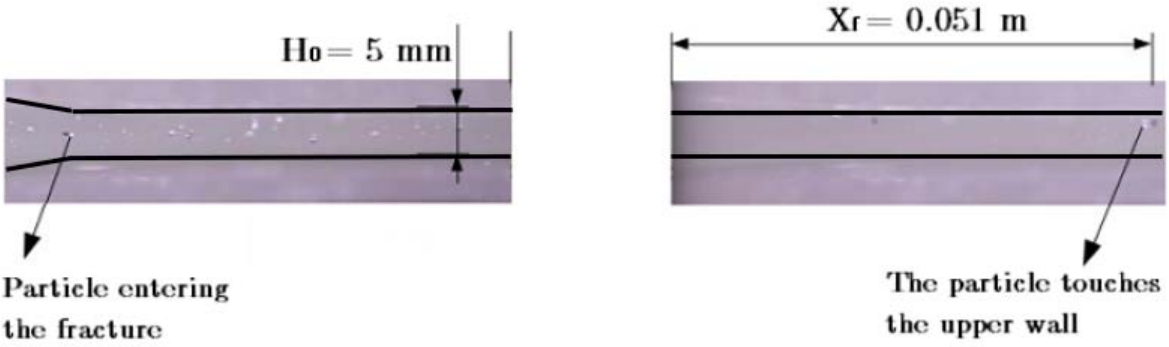

Figure 4.18: The distance X^f_{exp} traveled by a particle entering the fracture with two flat walls at $Z_p^0 \simeq 0$.

Although this experimental observation can be disputed due to the heterogeneity of the physical properties of the particles (size, density), it is nonetheless in relatively good agreement with the analytical solution, confirming thus that the analytical model gives a good approximation of the distance at which polydisperse particles would deposit in fractures with flat walls.

ii. Inertial regime: Lift-induced particle focusing

The mean aperture was set to $H_0 = 9\,mm$ and the hydraulic head difference to $\Delta h = 5\,cm$. In this case, $V_0 = 0.171\,m/s$ and $Re = 27.81$. Thus, flow inertial effects should be dominant. Several particles were injected at the fracture inlet and the camera was fixed in the same way as previously (section 3.2.1), i.e. at the fracture outlet. Figure 4.19 shows the

particles right before they exited the fracture.

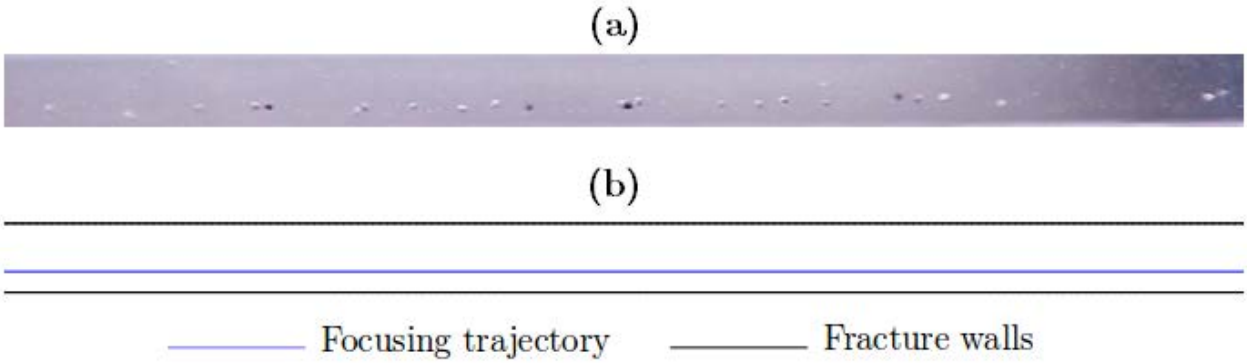

Figure 4.19: (a) Multiple particles filmed ahead the fracture outlet for $\Delta h = 5\,cm$ ($Re = 27.81\,cm$). (b)The deduced line on which particles focused

In this test, none of the particles float towards the upper wall, meaning that buoyancy forces are negligible with respect to other forces. Instead, particles tend to travel with the same vertical position and therefore move on a single trajectory. This is due to the equilibrium between the different inertial lift forces acting on the particles (cf. chapter 3). The slight deviation between the particle positions is due to their polydispersity. However, one can conclude that inertial focusing occurs this experiment.

4.3.3.b. Fracture with a flat wall and a sinusoidal wall

In this case, the fracture consists of a bottom flat wall and an upper sinusoidal one. The tests performed are similar to those done with the flat fracture (section 3.3.1). We first performed experiments with low Δh to assess the analytical model for this particular configuration. Δh was then increased to generate high Re in order to examine the effect of the fluid inertia on the particle behavior and the potential presence of inertial focusing.

i. Non-inertial regime: verification of the analytical model

The mean aperture was set equal to $H_0 = 5\,mm$ (the hydraulic aperture was then calculated $H_h = 4.9mm$). In order to minimize the inertial effects, the hydraulic head was fixed equal to $\Delta h = 2.5\,cm$. Using the LCL, $V_0 = 0.013\,m/s$ and $Re = 1.184$. In this case, the dimensionless numbers are $\tau \in [9.6 \times 10^{-6}; 1.7 \times 10^{-5}]$ and $W \in [-0.058; -0.032]$.

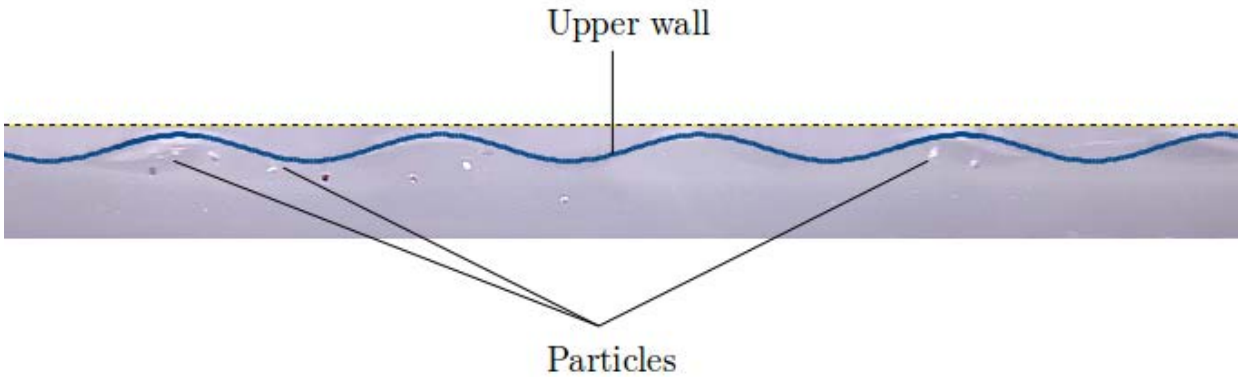

Figure 4.20: Multiple particles floated to the upper sinusoidal wall, ahead the fracture outlet for $\Delta h = 2.5cm$ ($Re = 1.184$, $\tau \in [9.6 \times 10^{-6}; 1.7 \times 10^{-5}]$ and $W \in [-0.058; -0.032]$).

Figure 4.20 shows the particles right before they exited the fracture. Most of the particles floated to the upper wall due to the density difference, suggesting that the inertial lift forces are overcome by the buoyancy forces so that inertial focusing can not occur. To verify the predictions of the analytical model, a random particle with an initial vertical position $z_p^0 \simeq 0$ was selected (Figure 4.21). The distance to deposition for this particle was measured to be equal to $x_{exp}^f = 0.22$ (or $X_{exp}^f = 0.15\,m$ in the dimensional form). Using the analytical model, the distance to deposition x_{ana}^f was evaluated in the range $x_{ana}^f \in [0.136; 0.25]$ (or $X_{ana}^f \in [0.092\,m; 0.17\,m]$). This means that the distance to deposition found experimentally belongs to the range predicted by the analytical model. This result proves that even when the fracture has a corrugated wall, the analytical model gives a good approximation of the range of the distance at which polydisperse particles would deposit.

ii. Inertial regime: Lift-induced particle focusing

As discussed in chapters 1 and 3, previous investigations on inertial focusing have mainly considered channels with flat walls (e.g. Di Carlo et al. [35]) or other geometries such as serpentine channels (Zhang et al. [120]) and spiral channels (Russom et al. [134]). Even though sinusoidal walls have not been considered before, one can expect the same effect to occur due to the equilibrium between the different lift forces acting on the particles. To this end, a test was performed with relatively high Δh.

We set the mean aperture $H_0 = 9\,mm$ (the hydraulic aperture was then calculated $H_h = 8.82\ mm$), and $\Delta h = 6\,cm$ leading to $Re = 18$. Several particles were injected at the

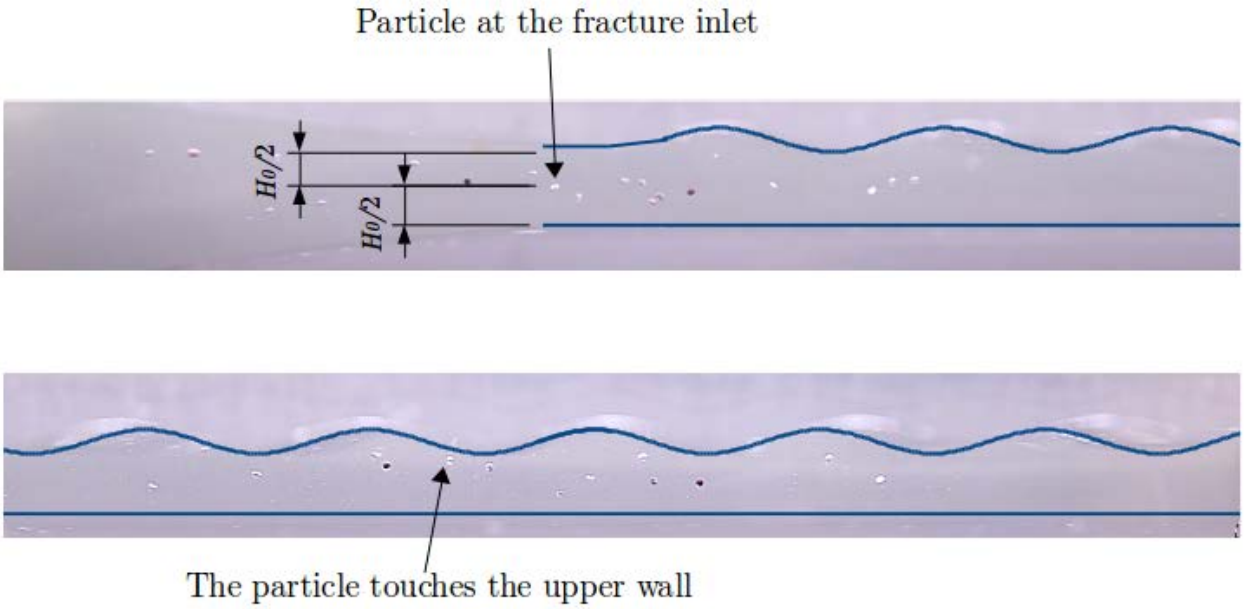

Figure 4.21: Particle with $Z_p^0 \simeq 0$ traveling through the fracture until it touches the upper wall.

fracture inlet. Figure 4.22 shows the particles right before they exited the fracture. Similarly to what was observed with two flat walls, the particles do not float but instead remain at a certain distance from the upper wall. This can also be interpreted as inertial focusing. An approximate line on which particles focused was drawn and it shows a sinusoidal shape. This experiment proves that inertial focusing can occur even when the fracture has a sinusoidal wall.

4.3.3.c. Fracture with two sinusoidal walls

The final tests were performed in the fracture with two sinusoidal walls. The walls were mounted in a mirror-symmetric configuration for which the variation of the aperture is maximum, and consequently the deviation of the LCL from the NS solution is maximum (cf. chapter 2). This configuration is, therefore, the most convenient to validate the analytical model.

i. Non-inertial regime: verification of the analytical model

The mean aperture was set equal to $H_0 = 7\,mm$ ($H_h = 6.12\ mm$). To minimize inertial

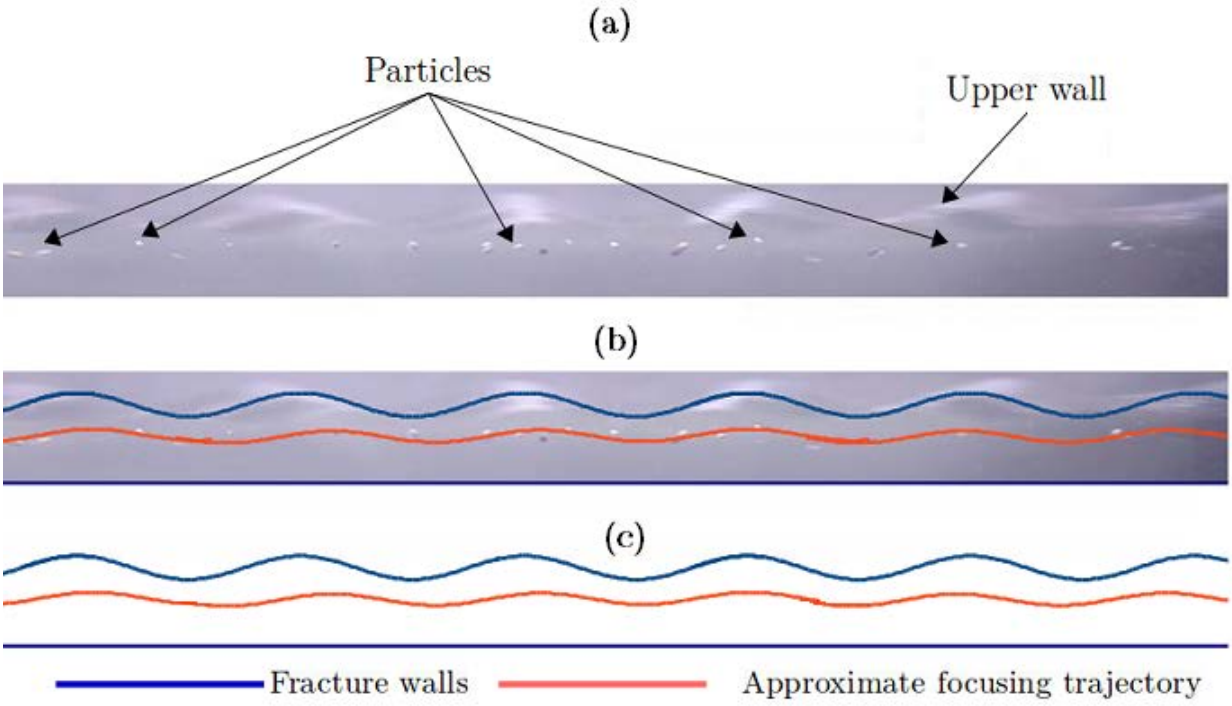

Figure 4.22: (a) Multiple particles filmed ahead the fracture outlet for $\Delta h = 6cm$ ($Re = 18$). (b) Approximated line on which the particles have focused is plotted in red by connecting the particles. (c) Schematic representation of the fracture and the approximated focusing trajectory.

effects, the hydraulic head was fixed equal to $\Delta h = 2.4\,cm$ which leads, using the LCL, to $V_0 = 0.02\,m/s$ and $Re = 2.3$. In this case, the dimensionless numbers are $\tau \in [4 \times 10^{-4}; 7.1 \times 10^{-4}]$ and $W \in [-0.038; -0.021]$.

Similarly to the previous tests, a random particle with an initial vertical position $z_p^0 \simeq 0$ was selected in order to verify the predictions of the analytical model (Figure 4.23). The distance to deposition for this particle was measured to be equal to $x_{exp}^f = 0.147$ (or $X_{exp}^f = 0.1\,m$ in the dimensional form). Using the analytical model, the distance to deposition x_{ana}^f was evaluated in the range $x_{ana}^f \in [0.092; 0.16]$ (or $X_{ana}^f \in [0.0625\,m; 0.108\,m]$). The distance to deposition measured experimentally belongs thus to the range predicted by the analytical model. This result confirms the ability of the analytical model to give a good approximation of the range of the distance at which polydisperse particles would deposit, even when the fracture has two corrugated walls.

Figure 4.23: Particle with $Z_p^0 \simeq 0$ traveling through the fracture until it touches the upper wall.

ii. Inertial regime: Lift-induced particle focusing

This test was performed with relatively high Δh to investigate the presence of inertial focusing when the two walls of the fracture are sinusoidal. Similarly to the two previous cases, one can expect inertial lift forces to dominate the buoyancy forces due to the increase of the flow inertial effects, so that the analytical model does not remain valid.

We set the mean aperture $H_0 = 8\,mm$ (the hydraulic aperture was then calculated $H_h = 7.22\,mm$), and $\Delta h = 10\,cm$ leading to $Re = 14.5$. Several particles were injected at the fracture inlet. Figure 4.24 shows the particles right before they exited the fracture.

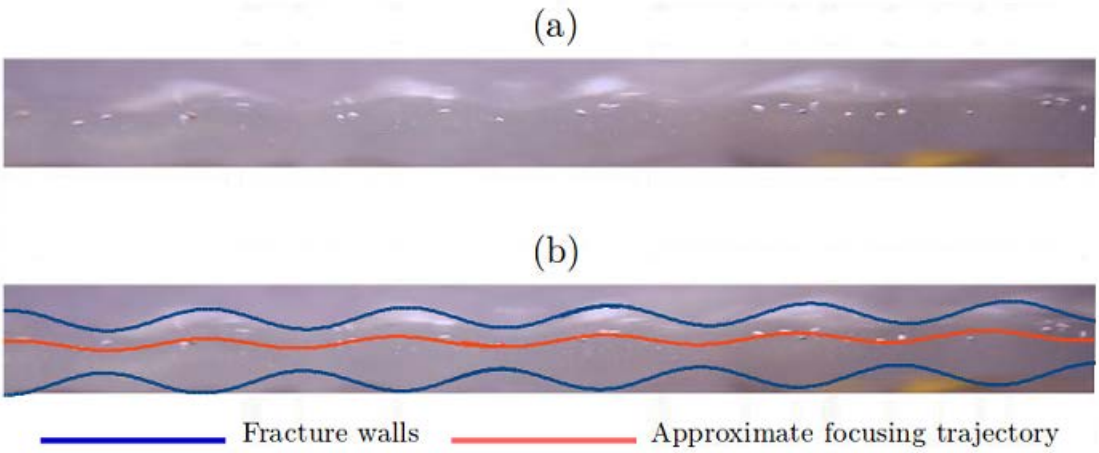

Figure 4.24: (a) Multiple particles filmed ahead the fracture outlet for $\Delta h = 10cm$ ($Re = 14.5$). (b) Approximated line on which the particles have focused.

Once again, the particles do not float but remain at a certain distance from the upper wall, which can be interpreted as inertial focusing. An approximate line on which particles focused was drawn and it also shows a sinusoidal shape. This experiment confirms that inertial focusing can occur even when the fracture has sinusoidal walls, and that the analytical

model is not valid when the flow inertial effects are relatively important.

4.3 Conclusion

In this chapter, the experimental apparatus that was designed and built up to study particle transport in closed channels was presented. A detailed description of the experimental setup and procedure was given. The apparatus was used to conduct a preliminary study of particle transport in fractures with flat and/or sinusoidal walls with dimensions in accordance with the theoretical assumptions made in the previous chapters.

The experimental results show that the apparatus is able to capture the different behaviors of particles in fractures, such as transport and deposition as well as inertial focusing. Many tests were performed using water and a water-glycerin mixture as liquid and poppy seeds as polydisperse particles moving in the liquid. By choosing an optimal difference in piezometric load, flow inertial effects can be reduced and the experimental results are in agreement with the analytical solution. The distance traveled by the particles from the inlet till they deposit fall in the range predicted by the analytical model developed in chapter 3. This suggests that the analytical solution can be used to evaluate deposition distance of polydisperse particles in fractures with flat and/or sinusoidal walls. When the hydraulic head was increased, i.e. for higher Re, it was shown that in fractures with both flat and sinusoidal walls, the particles focused on a single trajectory, verifying thus the presence of inertial focusing and confirming that inertial lift forces govern the particle behavior. This result verifies the assumption that the analytical model is valid only for low Re.

As a conclusion, the preliminary experimental results verify the analytical model developed in this thesis. In addition, these results demonstrate the ability of the experimental device for investigating particle transport in closed channel flows. It can be soundly used for future experimental studies of particle transport, which may improve our understanding of particle behavior and further validate the previously developed models.

CONCLUSION AND PERSPECTIVES

Single-phase flow and particle transport through fractures with flat and corrugated periodic walls have been investigated.

For single-phase flow, a thorough numerical study has been conducted to investigate the effects of the fracture geometry on the validity of the local cubic law (LCL). Numerical solutions of the Navier-Stokes (NS) equations have been compared to the predictions of the LCL. The results suggest that the validity of the LCL depends strongly on the geometrical properties of the fracture, defined by its aperture, the roughness (corrugation amplitude) of its walls, as well as the phase shift between the walls, and the asymmetry of the walls corrugations. The results further suggest that the criteria previously proposed for the applicability of the LCL to fracture flow, developed considering specific fracture geometries, can not be generalized for fractures with arbitrary geometries. In all the cases tested in the present manuscript, the LCL was found to be valid for modeling fracture flow, under the condition that the walls roughness as well as the Reynolds number Re are relatively small. Another numerical result, obtained in all the configurations tested in the simulations, suggests that the flow remains in the non-inertial regime for $Re \leq 15$.

To investigate particle transport through fractures, an approach combining analytical, numerical, and experimental developments has been adopted. In the analytical approach, the LCL was used to model the flow and was coupled to a simplified form of the particle motion equation in which particle inertia is neglected. A model describing the trajectories of the particles transported in channels with flat and corrugated walls was developed. It was found that when particle inertia is negligible, the particle behavior depends on a dimen-

sionless number W relating the particle properties and the flow characteristics, as well as on the geometry of the fracture. Using the proposed trajectory equation, and considering a uniform distribution of particles at the channel inlet, different transport regimes could be identified: transport, sedimentation and transition. According to the channel geometry, different diagrams that can predict the transport regime of particles entering a channel were then established. Moreover, numerical simulations combining the finite element method (FEM) to a Lagrangian particle tracking technique were conducted to assess the relevance of the analytical approach. Contrary to the analytical model, these simulations were conducted solving the full NS equations and taking into account particle inertia. Particles were injected at different positions at the inlet of channels with flat and corrugated walls, and the distance to deposition was computed numerically for each particle. This distance was then compared to the distance predicted by the analytical model. First, the dependence of the particle behavior on W and on the channel geometry was verified. Numerical experiments were then performed considering 100 particles. The results confirmed the ability of the regime diagrams to predict the behavior of the moving particles.

Finally, an apparatus was constructed to study particle behavior in fractures with flat and sinusoidal walls. The aim of this apparatus was to evaluate the pertinence of the analytical model when applied to practical configurations. To reduce the flow inertial effects, a water-glycerin mixture was used as the operating liquid. Preliminary tests conducted using poppy seeds seem to confirm the validity of the analytical model. For high pressure difference, the analytical model was no longer valid: The behavior of the particles is dominated by inertial lift forces, leading to inertial focusing in both the flat and sinusoidal walls configurations.

Overall, the results obtained in this thesis improve our understanding of the behavior of small particles immersed in closed channel flows, with a direct application to the transport of contaminants transported through fractures. For instance, we can identify, based on their size and density, the contaminants that are likely to deposit inside the fracture or be suspended and transported for long distances. Our results have other applications in water filtration and in mineral separation. In fact, based on our regime diagrams, a system of separation based on particle deposition in channels with sinusoidal walls could be designed. It would enable to separate particles based on their size and/or density depending on the

distance at which they would deposit in the channel. As the flow in the channel can simply be created by a hydraulic head difference, the advantage of such system with respect to present separation techniques is that it is passive and does not require important energy supply. Another application concerns inertial focusing, and may find some echoes in microfluidics. First, the results obtained may lead to a quantification of the conditions (Re and particle size) under which focusing becomes efficient. Second, we were able to observe inertial focusing in channels with sinusoidal walls. Further analyses may reveal new features at the origin of the focusing phenomenon, such as, for instance, the effect of the curvature of the channel walls on the inertial lift forces acting on the particles.

Perspectives

The ability of the experimental apparatus to study flow and particle transport in closed channels has been confirmed. It can now be used for further investigations. First, single-phase flow can be addressed. As the apparatus can be utilized over a wide range of flow rates and pressure differences, the validity of the LCL can be assessed experimentally. The results described in the second chapter of the present document could thus be practically evaluated.

Concerning particle transport, the most important perspective would consist in conducting experiments with spherical particles of different sizes and/or densities, in order to have an exact comparison with the analytical model and more particularly to validate the regime diagrams established in chapter 3. This can be done by injecting particles slightly denser than the liquid at the fracture inlet and by calculating the percentage of particles exiting the fracture. Distances to deposition could also be measured and compared to the analytical predictions, similar to what was done with poppy seeds in this thesis. Moreover, our experimental results suggest that the analytical model is not valid anymore when the flow inertial effects are important. The apparatus could therefore help to quantify the range of validity of the theoretical assumptions, i.e. Re and the ratio of particle size to channel aperture above which inertial lift forces start to be dominant with respect to other forces acting on the particles.

Regarding now the analytical and numerical modeling presented in this manuscript, sev-

eral developments could be considered. We neglected inertial effects so that our analytical model is valid only for small Re. For high Re, flow inertial effects may lead to the appearance of recirculation zones, especially when the walls corrugations are not smooth. These recirculation zones can trap the particles under specific conditions. Investigating this trapping mechanism requires an exact description of the fracture flow, and the LCL can no longer be used. A numerical analysis based on the NS equations could be applied.

Another perspective would consist in considering dense particle suspensions. In such configuration, two-way coupling must be taken into account, as well as particle-particle interactions. A numerical model combining the lattice Boltzmann method for describing the fluid flow and a discrete element method for describing particle motion has recently been developed in GeoRessources. This model enables to consider the effect of the particles on the flow and the particle-particle interactions. This couples approach could be used in combination with the experimental investigations to verify the analytical developments in both dilute and dense suspensions. This numerical model could also help to generalize the results concerning particle transport and deposition for the case of non-spherical particles. In addition, different particle shapes such as oblate and prolate spheroids, or parallelepipeds can be considered and the effect of particle orientation on the particle behavior may be eventually addressed.

Finally, another perspective would consist in assessing the validity of the analytical results obtained in this thesis in the case of fractures with non-periodic and non-smooth rough walls. Indeed, the analytical models proposed in this thesis do not require the fracture walls to be periodic. However, these analytical models incorporate expressions for the variation of the fracture walls, and more precisely, expressions for the variation of the fracture middle line and the fracture half-aperture along the fracture length ($H(X)$ and $\Phi(X)$ in chapters 2 and 3). Numerical and experimental verifications using fractures with non-periodic walls could be conducted to evaluate the validity of the analytical predictions, and more particularly the distance at which injected particles would deposit inside the fracture. The only limitation for such generalization would be the singularities that may appear in the wall shapes, which may give rise to singularities in the NS equations. This final point would require additional investigations.

Bibliography

[1] A. Hajjar, L. Scholtès, C. Oltéan, and M. Buès, "Transport and deposition of weakly inertial particles in closed channel flows at low reynolds number," *European Journal of Mechanics-B/Fluids*, 2017.

[2] J. F. McCarthy and J. M. Zachara, "Subsurface transport of contaminants," *Environmental science & technology*, vol. 23, no. 5, pp. 496–502, 1989.

[3] R. Kretzschmar, M. Borkovec, D. Grolimund, and M. Elimelech, "Mobile subsurface colloids and their role in contaminant transport," *Advances in agronomy*, vol. 66, pp. 121–193, 1999.

[4] K. C. Khilar and H. S. Fogler, *Migrations of fines in porous media*, vol. 12. Springer Science & Business Media, 1998.

[5] T. K. Sen and K. C. Khilar, "Review on subsurface colloids and colloid-associated contaminant transport in saturated porous media," *Advances in colloid and interface science*, vol. 119, no. 2, pp. 71–96, 2006.

[6] R. A. Jones, *Soft condensed matter*, vol. 6. Oxford University Press, 2002.

[7] A. Babiano, J. Cartwright, O. Piro, and A. Provenzale, "Dynamics of a small neutrally buoyant sphere in a fluid and targeting in hamiltonian systems," *Physical Review Letters*, vol. 84, no. 25, p. 5764, 2000.

[8] G. Haller and T. Sapsis, "Where do inertial particles go in fluid flows?," *Physica D: Nonlinear Phenomena*, vol. 237, no. 5, pp. 573–583, 2008.

[9] J. Cartwright, U. Feudel, G. Károlyi, A. de Moura, O. Piro, and T. Tél, "Dynamics of finite-size particles in chaotic fluid flows," in *Nonlinear Dynamics and Chaos: Advances and Perspectives*, pp. 51–87, Springer, 2010.

[10] E. Balkovsky, G. Falkovich, and A. Fouxon, "Intermittent distribution of inertial particles in turbulent flows," *Physical Review Letters*, vol. 86, no. 13, p. 2790, 2001.

[11] M. Lunau, A. Lemke, O. Dellwig, and M. Simon, "Physical and biogeochemical controls of microaggregate dynamics in a tidally affected coastal ecosystem," *Limnology and Oceanography*, vol. 51, no. 2, pp. 847–859, 2006.

[12] R. Shaw, "Particle-turbulence interactions in atmospheric clouds," *Annual Review of Fluid Mechanics*, vol. 35, no. 1, pp. 183–227, 2003.

[13] J. Eaton and J. Fessler, "Preferential concentration of particles by turbulence," *International Journal of Multiphase Flow*, vol. 20, pp. 169–209, 1994.

[14] K. D. Squires and J. K. Eaton, "Preferential concentration of particles by turbulence," *Physics of Fluids A: Fluid Dynamics*, vol. 3, no. 5, pp. 1169–1178, 1991.

[15] J. Bec, "Fractal clustering of inertial particles in random flows," *Physics of Fluids (1994-present)*, vol. 15, no. 11, pp. L81–L84, 2003.

[16] T. Nizkaya, J. Angilella, and M. Buès, "Inertial focusing of small particles in wavy channels: Asymptotic analysis at weak particle inertia," *Physica D: Nonlinear Phenomena*, vol. 268, pp. 91–99, 2014.

[17] J.-R. Angilella, "Dust trapping in vortex pairs," *Physica D: Nonlinear Phenomena*, vol. 239, no. 18, pp. 1789–1797, 2010.

[18] J. Angilella, R. Vilela, and A. Motter, "Inertial particle trapping in an open vortical flow," *Journal of Fluid Mechanics*, vol. 744, pp. 183–216, 2014.

[19] G. Falkovich, A. Fouxon, and M. Stepanov, "Accleration of rain initiation by cloud turbulence," *Nature*, vol. 419, no. 6903, p. 151, 2002.

[20] H. Stommel, "Trajectories of small bodies sinking slowly through convection cells," *J. mar. Res*, vol. 8, no. 11, pp. 24–29, 1949.

[21] M. Maxey, "The motion of small spherical particles in a cellular flow field," *Physics of Fluids (1958-1988)*, vol. 30, no. 7, pp. 1915–1928, 1987.

[22] R. Therrien and E. Sudicky, "Three-dimensional analysis of variably-saturated flow and solute transport in discretely-fractured porous media," *Journal of Contaminant Hydrology*, vol. 23, no. 1-2, pp. 1–44, 1996.

[23] J. Bouquain, Y. Méheust, D. Bolster, and P. Davy, "The impact of inertial effects on solute dispersion in a channel with periodically varying aperture," *Physics of Fluids*, vol. 24, no. 8, p. 083602, 2012.

[24] C. Oltéan, F. Golfier, and M. A. Buès, "Numerical and experimental investigation of buoyancy-driven dissolution in vertical fracture," *Journal of Geophysical Research: Solid Earth*, vol. 118, no. 5, pp. 2038–2048, 2013.

[25] D. F. Boutt, G. Grasselli, J. T. Fredrich, B. K. Cook, and J. R. Williams, "Trapping zones: The effect of fracture roughness on the directional anisotropy of fluid flow and colloid transport in a single fracture," *Geophysical Research Letters*, vol. 33, no. 21, 2006.

[26] K. S. Novakowski, "The analysis of tracer experiments conducted in divergent radial flow fields," *Water resources research*, vol. 28, no. 12, pp. 3215–3225, 1992.

[27] T. Nizkaya, *Transport and deposition of inertial particles in a fracture with periodic corrugation.* PhD thesis, Institut National Polytechnique de Lorraine, 2012.

[28] G. Segré and A. Silberberg, "Behaviour of macroscopic rigid spheres in poiseuille flow part 2. experimental results and interpretation," *Journal of Fluid Mechanics*, vol. 14, no. 1, pp. 136–157, 1962.

[29] J. A. Schonberg and E. Hinch, "Inertial migration of a sphere in poiseuille flow," *Journal of Fluid Mechanics*, vol. 203, pp. 517–524, 1989.

[30] E. S. Asmolov, "The inertial lift on a spherical particle in a plane poiseuille flow at large channel reynolds number," *Journal of Fluid Mechanics*, vol. 381, pp. 63–87, 1999.

[31] A. Karnis, H. Goldsmith, and S. Mason, "The flow of suspensions through tubes: V. inertial effects," *The Canadian Journal of Chemical Engineering*, vol. 44, no. 4, pp. 181–193, 1966.

[32] J. Matas, J. Morris, and E. Guazzelli, "Inertial migration of rigid spherical particles in poiseuille flow," *Journal of Fluid Mechanics*, vol. 515, pp. 171–195, 2004.

[33] J. Feng, H. H. Hu, and D. Joseph, "Direct simulation of initial value problems for the motion of solid bodies in a newtonian fluid. part 2. couette and poiseuille flows," *Journal of Fluid Mechanics*, vol. 277, pp. 271–301, 1994.

[34] B. Yang, J. Wang, D. Joseph, H. H. Hu, T.-W. Pan, and R. Glowinski, "Migration of a sphere in tube flow," *Journal of Fluid Mechanics*, vol. 540, pp. 109–131, 2005.

[35] D. Di Carlo, D. Irimia, R. Tompkins, and M. Toner, "Continuous inertial focusing, ordering, and separation of particles in microchannels," *Proceedings of the National Academy of Sciences*, vol. 104, no. 48, pp. 18892–18897, 2007.

[36] J. Martel and M. Toner, "Inertial focusing in microfluidics," *Annual review of biomedical engineering*, vol. 16, p. 371, 2014.

[37] T. Rasmussen, "Computer simulation model of steady fluid flow and solute transport through three-dimensional networks of variably saturated, discrete fractures," *Flow and transport through unsaturated fractured rock. Geophysical Monogr*, vol. 43, pp. 107–114, 1987.

[38] X. Zhang, D. Sanderson, R. Harkness, and N. Last, "Evaluation of the 2-d permeability tensor for fractured rock masses," in *International journal of rock mechanics and mining sciences & geomechanics abstracts*, vol. 33, pp. 17–37, Elsevier, 1996.

[39] V. Mourzenko, J.-F. Thovert, and P. Adler, "Percolation and conductivity of self-affine fractures," *Physical Review E*, vol. 59, no. 4, p. 4265, 1999.

[40] V. Mourzenko, J.-F. Thovert, and P. Adler, "Permeability of self-affine fractures," *Transport in porous media*, vol. 45, no. 1, pp. 89–103, 2001.

[41] E. Hakami and E. Larsson, "Aperture measurements and flow experiments on a single natural fracture," in *International Journal of Rock Mechanics and Mining Sciences & Geomechanics Abstracts*, vol. 33, pp. 395–404, Elsevier, 1996.

[42] S. Gentier, *Morphologie et comportement hydromécanique d'une fracture naturelle dans le granite sous conrainte normale*. BRGM, 1987.

[43] T. Belem, *Morphologie et comportement mécanique des discontinuités rocheuses*. PhD thesis, 1997.

[44] F. Plouraboue, *Propriétés géométriques et propriétés de transport des fractures à parois rugueuses*. PhD thesis, 1996.

[45] A. P. Oron and B. Berkowitz, "Flow in rock fractures: The local cubic law assumption reexamined," *Water Resources Research*, vol. 34, no. 11, pp. 2811–2825, 1998.

[46] F. Lefêvre, *Comportement en cisaillement et évolution de la morphologie des discontinuités rocheuses*. PhD thesis, 1999.

[47] H. Legrain, "Etude de l'influence de la rugosité sur l'écoulement de fluide dans les fissures rocheuses," 2007.

[48] C. Louis, *Etude des écoulements d'eau dans les roches fissurées et de leurs influences sur la stabilité des massifs rocheux*. PhD thesis, 1968.

[49] M. A. Dippenaar and J. L. Van Rooy, "On the cubic law and variably saturated flow through discrete open rough-walled discontinuities," *International Journal of Rock Mechanics and Mining Sciences*, vol. 89, pp. 200–211, 2016.

[50] S. Whitaker, "Flow in porous media i: A theoretical derivation of darcy's law," *Transport in porous media*, vol. 1, no. 1, pp. 3–25, 1986.

[51] J. Lin, *Étude du comportement hydromécanique d'une fracture rocheuse sous contrainte normale: développement d'un modèle numérique*. PhD thesis, Institut National Polytechnique de Lorraine, 1994.

[52] F. Davias, *Modélisation numérique d'écoulements en massif rocheux fracturé: contribution à la modélisation du comportement hydromécanique des milieux fracturés*. PhD thesis, Bordeaux 1, 1997.

[53] S. Crosnier, *Écoulement dans une fracture de géométrie radiale: influence d'une rugosité périodique*. PhD thesis, Institut National Polytechnique de Lorraine, 2001.

[54] J. Bear, "Dynamics of fluids in porous media," *American Elsevier, New York*, 1972.

[55] H. Darcy, *Les fontaines publiques de la ville de Dijon: exposition et application...* Dalmont, 1856.

[56] D. M. Brown, *Stochastic analysis of flow and solute transport in a variable-aperture rock fracture*. PhD thesis, Massachusetts Institute of Technology, 1984.

[57] S. R. Brown, "Fluid flow through rock joints: the effect of surface roughness," *Journal of Geophysical Research: Solid Earth*, vol. 92, no. B2, pp. 1337–1347, 1987.

[58] S. Silliman, "An interpretation of the difference between aperture estimates derived from hydraulic and tracer tests in a single fracture," *Water Resources Research*, vol. 25, no. 10, pp. 2275–2283, 1989.

[59] Z. Chen, S. Narayan, Z. Yang, and S. Rahman, "An experimental investigation of hydraulic behaviour of fractures and joints in granitic rock," *International Journal of Rock Mechanics and Mining Sciences*, vol. 37, no. 7, pp. 1061–1071, 2000.

[60] J. S. Konzuk and B. H. Kueper, "Evaluation of cubic law based models describing single-phase flow through a rough-walled fracture," *Water Resources Research*, vol. 40, no. 2, 2004.

[61] P. A. Witherspoon, J. S. Wang, K. Iwai, and J. E. Gale, "Validity of cubic law for fluid flow in a deformable rock fracture," *Water resources research*, vol. 16, no. 6, pp. 1016–1024, 1980.

[62] Y. Tsang and C. Tsang, "Hydrological characterization of variable-aperture fractures," in *International Symposium on Rock Joints*, pp. 423–430, 1990.

[63] C. E. Renshaw, "On the relationship between mechanical and hydraulic apertures in rough-walled fractures," *Journal of Geophysical Research: Solid Earth*, vol. 100, no. B12, pp. 24629–24636, 1995.

[64] A. J. A. Unger and C. Mase, "Numerical study of the hydromechanical behavior of two rough fracture surfaces in contact," *Water Resources Research*, vol. 29, no. 7, pp. 2101–2114, 1993.

[65] E. Hakami and N. Barton, "Aperture measurements and flow experiments using transparent replicas of rock joints," *Rock Joints*, pp. 383–390, 1990.

[66] R. Gutfraind and A. Hansen, "Study of fracture permeability using lattice gas automata," *Transport in Porous Media*, vol. 18, no. 2, pp. 131–149, 1995.

[67] S. P. Neuman, "Trends, prospects and challenges in quantifying flow and transport through fractured rocks," *Hydrogeology Journal*, vol. 13, no. 1, pp. 124–147, 2005.

[68] L. I. G. de Vallejo and M. Ferrer, *Geological engineering*. CRC Press, 2011.

[69] R. W. Zimmerman and G. S. Bodvarsson, "Hydraulic conductivity of rock fractures," *Transport in Porous Media*, vol. 23, no. 1, pp. 1–30, 1996.

[70] E. Hasegawa and H. Izuchi, "On steady flow through a channel consisting of an uneven wall and a plane wall: Part 1. case of no relative motion in two walls," *Bulletin of JSME*, vol. 26, no. 214, pp. 514–520, 1983.

[71] H. Basha and W. El-Asmar, "The fracture flow equation and its perturbation solution," *Water Resources Research*, vol. 39, no. 12, 2003.

[72] R. W. Zimmerman and I.-W. Yeo, "Fluid flow in rock fractures: From the navier-stokes equations to the cubic law," *Dynamics of fluids in fractured rock*, pp. 213–224, 2000.

[73] M. Firdaouss, J.-L. Guermond, and P. Le Quéré, "Nonlinear corrections to darcy's law at low reynolds numbers," *Journal of Fluid Mechanics*, vol. 343, pp. 331–350, 1997.

[74] A. Dybbs and R. Edwards, "A new look at porous media fluid mechanicsdarcy to turbulent," in *Fundamentals of transport phenomena in porous media*, pp. 199–256, Springer, 1984.

[75] E. Skjetne and J. Auriault, "New insights on steady, non-linear flow in porous media," *European Journal of Mechanics-B/Fluids*, vol. 18, no. 1, pp. 131–145, 1999.

[76] D. Lo Jacono, F. Plouraboué, and A. Bergeon, "Weak-inertial flow between two rough surfaces," *Physics of Fluids*, vol. 17, no. 6, p. 063602, 2005.

[77] P. K. Kitanidis and B. B. Dykaar, "Stokes flow in a slowly varying two-dimensional periodic pore," *Transport in porous media*, vol. 26, no. 1, pp. 89–98, 1997.

[78] A. E. Malevich, V. V. Mityushev, and P. M. Adler, "Stokes flow through a channel with wavy walls," *Acta Mechanica*, vol. 182, no. 3-4, pp. 151–182, 2006.

[79] P. Forchheimer, "Wasserbewegung durch boden," *Zeitz. Ver. Duetch Ing.*, vol. 45, pp. 1782–1788, 1901.

[80] Y. Lucas, M. Panfilov, and M. Buès, "High velocity flow through fractured and porous media: the role of flow non-periodicity," *European Journal of Mechanics-B/Fluids*, vol. 26, no. 2, pp. 295–303, 2007.

[81] R. Zimmerman, S. Kumar, and G. Bodvarsson, "Lubrication theory analysis of the permeability of rough-walled fractures," in *International Journal of Rock Mechanics and Mining Sciences & Geomechanics Abstracts*, vol. 28, pp. 325–331, Elsevier, 1991.

[82] W. L. Power and T. E. Tullis, "Euclidean and fractal models for the description of rock surface roughness," *Journal of Geophysical Research: Solid Earth*, vol. 96, no. B1, pp. 415–424, 1991.

[83] T. Le Borgne, D. Bolster, M. Dentz, P. Anna, and A. Tartakovsky, "Effective pore-scale dispersion upscaling with a correlated continuous time random walk approach," *Water Resources Research*, vol. 47, no. 12, 2011.

[84] S. R. Brown, H. W. Stockman, and S. J. Reeves, "Applicability of the reynolds equation for modeling fluid flow between rough surfaces," *Geophysical Research Letters*, vol. 22, no. 18, pp. 2537–2540, 1995.

[85] M. E. Waite, S. Ge, H. Spetzler, and D. B. Bahr, "The effect of surface geometry on fracture permeability: A case study using a sinusoidal fracture," *Geophysical Research Letters*, vol. 25, no. 6, pp. 813–816, 1998.

[86] S. Sisavath, A. Al-Yaaruby, C. C. Pain, and R. W. Zimmerman, "A simple model for deviations from the cubic law for a fracture undergoing dilation or closure," *Pure and Applied Geophysics*, vol. 160, no. 5-6, pp. 1009–1022, 2003.

[87] I. W. Yeo and S. Ge, "Applicable range of the reynolds equation for fluid flow in a rock fracture," *Geosciences Journal*, vol. 9, no. 4, pp. 347–352, 2005.

[88] Q. q. Liu and H. g. Fan, "The characteristics and estimation of flow through a single rough-walled fracture," *Journal of Hydrodynamics, Ser. B*, vol. 24, no. 3, pp. 315–322, 2012.

[89] V. Renu and G. S. Kumar, "Benzene dissolution and transport in a saturated sinusoidal fracture with non-uniform flow: Numerical investigation and sensitivity analysis," *Environmental Processes*, pp. 1–15, 2017.

[90] D. Edwards, M. Shapiro, H. Brenner, and M. Shapira, "Dispersion of inert solutes in spatially periodic, two-dimensional model porous media," *Transport in Porous Media*, vol. 6, no. 4, pp. 337–358, 1991.

[91] D. Bolster, M. Dentz, and T. Le Borgne, "Solute dispersion in channels with periodically varying apertures," *Physics of Fluids (1994-present)*, vol. 21, no. 5, p. 056601, 2009.

[92] V. V. Mourzenko, J. F. Thovert, and P. M. Adler, "Permeability of a single fracture; validity of the reynolds equation," *Journal de Physique II*, vol. 5, no. 3, pp. 465–482, 1995.

[93] M. J. Nicholl, H. Rajaram, R. J. Glass, and R. Detwiler, "Saturated flow in a single fracture: Evaluation of the reynolds equation in measured aperture fields," *Water Resources Research*, vol. 35, no. 11, pp. 3361–3373, 1999.

[94] S. H. Lee, K. K. Lee, and I. W. Yeo, "Assessment of the validity of stokes and reynolds equations for fluid flow through a rough-walled fracture with flow imaging," *Geophysical Research Letters*, vol. 41, no. 13, pp. 4578–4585, 2014.

[95] C. E. Renshaw, J. S. Dadakis, and S. R. Brown, "Measuring fracture apertures: A comparison of methods," *Geophysical Research Letters*, vol. 27, no. 2, pp. 289–292, 2000.

[96] D. J. Brush and N. R. Thomson, "Fluid flow in synthetic rough-walled fractures: Navier-stokes, stokes, and local cubic law simulations," *Water Resources Research*, vol. 39, no. 4, 2003.

[97] M. Van Dyke, "Slow variations in continuum mechanics," *Archive of Applied Mechanics*, vol. 25, pp. 1–45, 1987.

[98] V. I. Borisov, "Viscous liquid flow in a channel with sinusoidal walls," *Journal of Engineering Physics and Thermophysics*, vol. 42, no. 4, pp. 399–401, 1982.

[99] M. A. Buès, M. Panfilov, S. Crosnier, and C. Oltéan, "Macroscale model and viscous–inertia effects for navier–stokes flow in a radial fracture with corrugated walls," *Journal of Fluid Mechanics*, vol. 504, pp. 41–60, 2004.

[100] S. Ge, "A governing equation for fluid flow in rough fractures," *Water Resources Research*, vol. 33, no. 1, pp. 53–61, 1997.

[101] W. Mallikamas and H. Rajaram, "An improved two-dimensional depth-integrated flow equation for rough-walled fractures," *Water Resources Research*, vol. 46, no. 8, 2010.

[102] J. Qian, Z. Chen, H. Zhan, and H. Guan, "Experimental study of the effect of roughness and reynolds number on fluid flow in rough-walled single fractures: a check of local cubic law," *Hydrological processes*, vol. 25, no. 4, pp. 614–622, 2011.

[103] L. Wang, M. B. Cardenas, D. T. Slottke, R. A. Ketcham, and J. M. Sharp, "Modification of the local cubic law of fracture flow for weak inertia, tortuosity, and roughness," *Water Resources Research*, vol. 51, no. 4, pp. 2064–2080, 2015.

[104] Z. Chen, J. Qian, H. Zhan, Z. Zhou, J. Wang, and Y. Tan, "Effect of roughness on water flow through a synthetic single rough fracture," *Environmental Earth Sciences*, vol. 4, no. 76, pp. 1–17, 2017.

[105] J. Yin, G. Yang, and Y. Li, "The effects of wavy plate phase shift on flow and heat transfer characteristics in corrugated channel," *Energy Procedia*, vol. 14, pp. 1566–1573, 2012.

[106] H. Mohammed, A. M. Abed, and M. Wahid, "The effects of geometrical parameters of a corrugated channel with in out-of-phase arrangement," *International Communications in Heat and Mass Transfer*, vol. 40, pp. 47–57, 2013.

[107] R. W. Zimmerman, A. Al-Yaarubi, C. C. Pain, and C. A. Grattoni, "Non-linear regimes of fluid flow in rock fractures," *International Journal of Rock Mechanics and Mining Sciences*, vol. 41, pp. 163–169, 2004.

[108] A. Jebakumar, K. Premnath, and J. Abraham, "Lattice boltzmann method simulations of stokes number effects on particle trajectories in a wall-bounded flow," *Computers & Fluids*, vol. 124, pp. 208–219, 2016.

[109] R. Chen, W. Chen, and C. Lai, "Deposition of charged particles in a channel," *Powder Technology*, vol. 74, no. 2, pp. 135–140, 1993.

[110] R. Chen, H. Chiou, and D. Sun, "Deposition of particles in a convergent channel," *Powder Technology*, vol. 87, no. 1, pp. 83–86, 1996.

[111] T. Sapsis and G. Haller, "Clustering criterion for inertial particles in two-dimensional time-periodic and three-dimensional steady flows," *Chaos: An Interdisciplinary Journal of Nonlinear Science*, vol. 20, no. 1, p. 017515, 2010.

[112] T. Auton, J. Hunt, and M. Prud'Homme, "The force exerted on a body in inviscid unsteady non-uniform rotational flow," *Journal of Fluid Mechanics*, vol. 197, pp. 241–257, 1988.

[113] C. Tchen, *Mean Value and Correlation Problems Connected with the Motion of Small Particles Suspended in a Turbulent Fluid*. PhD thesis, Delft, 1947.

[114] F. Candelier, J. Angilella, and M. Souhar, "On the effect of the boussinesq–basset force on the radial migration of a stokes particle in a vortex," *Physics of Fluids*, vol. 16, no. 5, pp. 1765–1776, 2004.

[115] J. Zhang, S. Yan, D. Yuan, G. Alici, N.-T. Nguyen, M. E. Warkiani, and W. Li, "Fundamentals and applications of inertial microfluidics: a review," *Lab on a Chip*, vol. 16, no. 1, pp. 10–34, 2016.

[116] G. Magnus, "On the deviation of projectiles, and: on a sinking phenomenon among rotating bodies," *Ann Phys*, vol. 164, p. 29, 1853.

[117] B. Ho and L. Leal, "Inertial migration of rigid spheres in two-dimensional unidirectional flows," *Journal of Fluid Mechanics*, vol. 65, no. 02, pp. 365–400, 1974.

[118] P. Vasseur and R. Cox, "The lateral migration of a spherical particle in two-dimensional shear flows," *Journal of Fluid Mechanics*, vol. 78, no. 2, pp. 385–413, 1976.

[119] F. Bretherton, "The motion of rigid particles in a shear flow at low reynolds number," *Journal of Fluid Mechanics*, vol. 14, no. 02, pp. 284–304, 1962.

[120] J. Zhang, W. Li, M. Li, G. Alici, and N.-T. Nguyen, "Particle inertial focusing and its mechanism in a serpentine microchannel," *Microfluidics and Nanofluidics*, vol. 17, no. 2, pp. 305–316, 2014.

[121] M. Maxey and J. Riley, "Equation of motion for a small rigid sphere in a nonuniform flow," *Physics of Fluids (1958-1988)*, vol. 26, no. 4, pp. 883–889, 1983.

[122] R. Gatignol, "The faxén formulas for a rigid particle in an unsteady non-uniform stokes-flow," *Journal de Mécanique théorique et appliquée*, vol. 2, no. 2, pp. 143–160, 1983.

[123] H. Faxén, "Der widerstand gegen die bewegung einer starren kugel in einer zähen flüssigkeit, die zwischen zwei parallelen ebenen wänden eingeschlossen ist," *Annalen der Physik*, vol. 373, no. 10, pp. 89–119, 1922.

[124] L. Bergougnoux, G. Bouchet, D. Lopez, and E. Guazzelli, "The motion of solid spherical particles falling in a cellular flow field at low stokes number," *Physics of Fluids (1994-present)*, vol. 26, no. 9, p. 093302, 2014.

[125] J. L. Best, "Sediment transport and bed morphology at river channel confluences," *Sedimentology*, vol. 35, no. 3, pp. 481–498, 1988.

[126] L. Yilmaz, "Experimental study of sediment transport in meandering channels," *Water Resources Management*, vol. 22, no. 2, pp. 259–275, 2008.

[127] X. Wang, Q. Yang, W. Lu, and X. Wang, "Effects of bed load movement on mean flow characteristics in mobile gravel beds," *Water Resources Management*, vol. 25, no. 11, p. 2781, 2011.

[128] A. Jarno-Druaux, J. Brossard, and F. Marin, "Dynamical evolution of ripples in a wave channel," *European Journal of Mechanics-B/Fluids*, vol. 23, no. 5, pp. 695–708, 2004.

[129] T. Chu, A. Jarno-Druaux, F. Marin, and A. Ezersky, "Particle trajectories and size sorting above a rippled bed under standing water waves," *Physical Review E*, vol. 85, no. 2, p. 021304, 2012.

[130] I. W. Yeo, M. H. De Freitas, and R. W. Zimmerman, "Effect of shear displacement on the aperture and permeability of a rock fracture," *International Journal of Rock Mechanics and Mining Sciences*, vol. 35, no. 8, pp. 1051–1070, 1998.

[131] Y. Ju, Q. Zhang, Y. Yang, H. Xie, F. Gao, and H. Wang, "An experimental investigation on the mechanism of fluid flow through single rough fracture of rock," *Science China Technological Sciences*, vol. 56, no. 8, pp. 2070–2080, 2013.

[132] T. Rush, T. Newell, and A. Jacobi, "An experimental study of flow and heat transfer in sinusoidal wavy passages," *International journal of Heat and Mass Transfer*, vol. 42, no. 9, pp. 1541–1553, 1999.

[133] N.-S. Cheng, "Formula for the viscosity of a glycerol- water mixture," *Industrial & engineering chemistry research*, vol. 47, no. 9, pp. 3285–3288, 2008.

[134] A. Russom, A. K. Gupta, S. Nagrath, D. Di Carlo, J. F. Edd, and M. Toner, "Differential inertial focusing of particles in curved low-aspect-ratio microchannels," *New Journal of Physics*, vol. 11, no. 7, p. 075025, 2009.

Abstract

Analytical, numerical, and experimental investigations of particle transport in fractures with flat and corrugated walls

The aim of the present thesis is to study the transport and deposition of small solid particles in fracture flows. First, single-phase fracture flow is investigated in order to assess the validity of the local cubic law for modeling flow in corrugated fractures. Channels with sinusoidal walls having different geometrical properties are considered to represent different fracture geometries. It is analytically shown that the hydraulic aperture of the fracture clearly deviates from its mean aperture when the walls roughness is relatively high. The finite element method is then used to solve the continuity and the Navier-Stokes equations and to simulate fracture flow in order to compare with the theoretical predictions of the local cubic law for Reynolds numbers Re in the range $6.7 \times 10^{-2} - 6.7 \times 10^{1}$. The results show that for low Re, typically less than 15, the local cubic law can properly describe the fracture flow, especially when the fracture walls have small corrugation amplitudes. For Re higher than 15, the local cubic law can still be valid under the conditions that the fracture presents a low aspect ratio, small corrugation amplitude, and moderate phase lag between its walls. Second, particle-laden flows are studied. An analytical approach has been developed to show how particles sparsely distributed in steady and laminar fracture flows can be transported for long distances or conversely deposited inside the channel. More precisely, a rather simple particle trajectory equation is established. Based on this equation, it is demonstrated that when particles' inertia is negligible, their behavior is characterized by the fracture geometry and by a dimensionless number W that relates the ratio of the particles sedimentation terminal velocity to the flow mean velocity. The proposed particle trajectory equation is verified by comparing its predictions to particle tracking numerical simulations taking into account particle inertia and resolving the full Navier-Stokes equations. The equation is shown to be valid under the conditions that flow inertial effects are limited. Based on this trajectory equation, regime diagrams that can predict the behavior of particles entering closed channel flows are built. These diagrams enable to forecast if the particles entering the channel will be either deposited or transported till the channel outlet. Finally, an experimental apparatus that was designed to have a practical assessment of the analytical model is presented. Preliminary experimental results tend to verify the analytical model. Overall, the work presented in this thesis give new insights on the behavior of small particles in fracture flows, which may improve our prediction and control of underground contamination, and may have applications in the development of new water filtration and mineral separation techniques.

Keywords: Particle-laden flow, Particle trajectory, Corrugated walls, Rough Fracture, Local Cubic Law

Résumé

Études analytique, numérique, et expérimentale du transport de particules dans des fractures parois plates et ondulées

Le but de cette thèse est d'étudier le transport et le dépôt de particules solides dans les écoulements à travers les fractures. Dans un premier temps, l'écoulement monophasique à travers les fractures est étudié afin d'évaluer la validité de la loi cubique locale comme modèle de l'écoulement. Des canaux à parois sinsoïdales à géométrie variable sont utilisés pour représenter différents types de fractures. Un premier développement analytique montre que l'ouverture hydraulique de la fracture diffère de son ouverture moyenne lorsque la rugosité des parois est élevée. La méthode des éléments finis est ensuite utilisée pour résoudre les équations de continuité et de Navier-Stokes et comparer les solutions numériques aux prédictions théoriques de la loi cubique locale sur une gamme relativement étendue de nombres de Reynolds Re. Pour de faibles Re, typiquement inférieurs à 15, la loi cubique locale décrit raisonnablement l'écoulement, surtout lorsque la rugosité et le déphasage entre les parois sont relativement faibles. Dans un deuxième temps, les écoulements chargés de particules sont étudiés. Une approche analytique est d'abord développée pour montrer comment des particules distribuées dans un écoulement stationnaire et laminaire à travers une fracture peuvent être transportées sur de longues distances ou au contraire se déposer à l'intérieur. Plus précisément, une équation simple décrivant la trajectoire d'une particule est établie. Sur la base de cette équation, il est démontré que, quand l'inertie des particules est négligeable, leur comportement dépend directement de la géométrie de la fracture et d'un nombre adimensionnel W qui relie la vitesse de sédimentation des particules à la vitesse moyenne de l'écoulement. L'équation proposée est vérifiée en comparant ses prédictions à des simulations numériques de suivi de particules prenant en compte l'inertie des particules et résolvent complètement les équations de Navier-Stokes. Il est montré que l'équation est valide lorsque l'inertie du fluide est faible. Des diagrammes de régimes, permettant de prévoir le comportement des particules à travers la fracture sont proposés. Enfin, un appareil expérimental conçu dans le but d'effectuer une évaluation pratique du modèle analytique est présenté et les résultats préliminaires sont discutés. Les rèsultats expérimentaux préliminaires tendent valider le modèle analytique. De façon plus générale, les résultats obtenus à travers ce travail de thèse font progresser nos connaissances du comportement des petites particules transportées dans les écoulements de fractures. Potentiellement, ce travail devrait permettre d'améliorer notre prévision de la pollution souterraine, et peut avoir des applications dans le développement de nouvelles techniques de filtration de l'eau et de séparation des minéraux.

Mots-clefs: Transport de particules, Fracture rugueuse, Parois ondulées, Loi cubique locale